Optics, Photonics and Lasers:

Proceedings of the 3ʳᵈ International Conference on Optics, Photonics and Lasers (OPAL' 2020)

21-22 October 2020

Tenerife (Canary Islands), Spain

Edited by Sergey Y. Yurish

IFSA Publishing

Sergey Y. Yurish, *Editor*
Optics, Photonics and Lasers
OPAL' 2020 Conference Proceedings

Contents

Foreword

On behalf of the OPAL' 2020 Organizing Committee, I introduce with pleasure these proceedings devoted to contributions from the 3rd International Conference on Optics, Photonics and Lasers (OPAL' 2020). The conference is organized by the International Frequency Sensor Association (IFSA) in technical cooperation with our media partners: Institute of Physics (IOP), UK and MDPI Photonics journal (ISSN 2304-6732), Switzerland.

In keeping with tradition begun in 2018 in Barcelona, Spain and in 2019 in Amsterdam, The Netherlands the Conference attracts researchers and practitioners in the related fields, from around the world including 4 keynote speakers from Germany and India.

The conference program provides an opportunity for researchers interested in optics, photonics and lasers to discuss their latest results and exchange ideas on the new trends and challenges. The main objective of the Conference is to encourage discussion on a broad range of optic related topics and to stimulate new collaborations among the participants.

The conference proceedings contains all papers of regular and keynote presentations. We hope that these proceedings will give readers an excellent overview of important and diversity topics discussed at the conference. Based on the proceeding's contributions, selected and extended papers will be submitted by the authors to the special issue of '*Sensors & Transducers*' journal (ISSN: 2306-8515, e-ISSN 1726-5479) or Photonics journal (ISSN 2304-6732). The limited number of articles, published in '*Sensors & Transducers*' journal will be invited to be extended for '*Advances in Optics: Reviews*', Vol. 5, Book Series, which will be published in 2021.

We thank all authors for submitting their latest work, thus contributing to the excellent technical contents of the Conference. Especially, we would like to thank the individuals and organizations that worked together diligently to make this Conference a success, and to the members of the International Program Committee for the thorough and careful review of the papers. It is important to point out that the great majority of the efforts in organizing the technical program of the Conference came from volunteers.

Prof., Dr. Sergey Y. Yurish
OPAL' 2020 Chairman

(006)

Increasing Microcirculation in the Surface Layer of Lower Limb Tissue with Diabetic Foot Uncler by Laser Stimulation

K. S. Beloshenko [1], I. A. Riabenko [1], K. S. Galicheva [1]
[1] V. N. Karazin Kharkiv National University, 4 Svobody Sq., Kharkiv, 61022, Ukraine
Tel.: + 380989824245, fax: +380577050241
E-mail: kbeloshenko@karazin.ua

Summary. This work is devoted to the study of the mechanisms of laser radiation effect on tissues of patients with diabetic foot ulcer (DFU). When exposed to a laser beam (radiation power of 50 mW, $\lambda = 635$ nm), patients experience increased microcirculation due to the increase in the mass flow of blood in the capillaries. To confirm the working hypothesis, sugar concentration in the blood, temperature distribution over the lower limbs before and after laser irradiation, systolic and diastolic blood pressure are measured. Wound healing is much faster, taking into account the daily procedures on the Barva apparatus. Skin condition, color and turgor had a healthier appearance after the 3 procedures. The approach in treatment and rehabilitation with non-invasive methods available is studied. The building of a physical-mathematical model of the process based on the polyelastic model of the sample is planned. The data obtained fully confirm the hypothesis.

Keywords: Barva apparatus, Diabetic foot ulcer, Laser irradiation, Thermography.

1. Introduction

According to the International Diabetes Federation, at the end of 2013, more than 382 million patients with diabetes mellitus (DM) were registered in the world, expected to rise to 592 million by 2035 [1]. It is also known that every 15 years the number of patients with DM doubles [2]. One of the most dangerous complications of DM is diabetic foot uncler (DFU). This complication is observed in 15-25 % of patients [3-5]. To date, the treatment of DFU in most cases ends with lower-limb amputations (LLAs). In the world, every 40 seconds one such operation is performed [6]. The UN calls on all countries of the world to take the necessary measures to reduce the number of amputations at least twice. Moreover, more than a trillion US dollars are spent annually on the fight against DM and its complications worldwide [7].

DFU is associated with a significant deterioration in blood microcirculation in the lower extremities in patients with DM [8]. Therefore, the aim of the work is to study the laws of action of low molecular weight electromagnetic radiation of the red spectrum on the microcirculation of blood in the lower extremities of patients with DM.

2. Materials and Methods

2.1. Physical Model of Fluid Redistribution

The methods of laser medicine and the main mechanisms of interaction of laser radiation with tissues have been known for a long time [9, 10]. Photo thermal and photochemical transformations of continuous laser radiation can lead to significant results both in the prevention of diseases [10] and in their treatment [11]. One of the methods of analyzing the effect of laser radiation on the surface layer is given by the thermodynamic approach. With the approach, we assume that one-photon absorption of laser radiation occurs in the surface layer of body tissues in accordance with the Bugrea-Lambert-Behr law. We can estimate the penetration depth of laser radiation

$$h = \frac{1}{\alpha} \times \ln \frac{I}{I_0}, \qquad (1)$$

at which the radiation intensity is decreased by factor e, if we take the extinction coefficient for $\lambda = 532$ nm equal to $\alpha = 3.33$ cm^{-1} [12], then the penetration depth will be 0.3 cm. Accordingly, the most of radiation is absorbed by the skin, and we can simulate the skin as a black body. Photothermal conversion consists in the fact that the short-wave laser radiation is converted to long-wave radiation, which was recorded using a Fluke Ti400 thermal imager. From the Wien's displacement law [13], we can calculate the maximum of the long-wavelength radiation band within the range of 8-14 μm, provided that the skin surface temperatures is within the range of 35-37 °C. It is noted that the integral power of the secondary radiation can be estimated on the base of Stefan-Boltzmann law [13]:

$$I = \varepsilon \sigma T^4, \qquad (2)$$

where I = 0.05 W/cm^2 at temperature T = 300 K, $\varepsilon \simeq 1$, $\sigma = 5.67 \times 10^{-8}$ W/(m^{2}K^4) is the Stefan-Boltzmann constant.

2.2. Anatomical Model of the Disease

The main causes of the development of DFU are peripheral arterial disease (PAD) [14]. Other factors

that are responsible for diabetic foot infections are repetitive trauma and super-imposing foot infections [15, 16].

In the foot, the own plantar finger arteries (aa. Digitdles plantdres propriae) which are shown in Fig. 1, the dorsal digital arteries (aa. Digitdles dorsdles) and the calcaneal rete which are shown in Fig. 2 (rete calcalcum) are primarily and potentially destroyed.
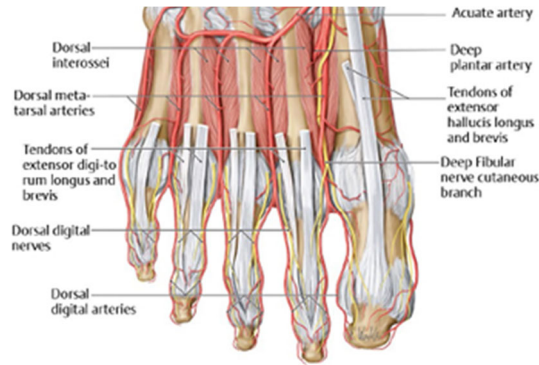
Fig. 1. The dorsal arteries and nerves of the foot [17].
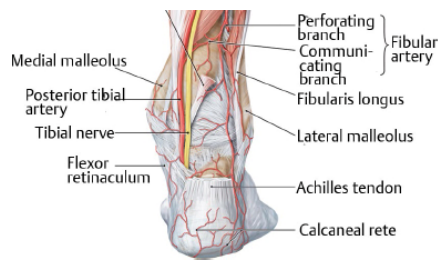
Fig. 2. Right leg, posterior view. Neurovascular structures in the deep posterior compartment after partial removal of the triceps surae and the deep layer of the fascia of the leg [17].

Every vessel in the leg has tissues surrounding it, the parameters of which will be taken into account when constructing the polyelastic model.

To assess the redistribution of temperature, it is important to make a thermogram taking into account the capture of the anterior and posterior regions of the knee joint, the proximal and distal parts of the anterior and posterior regions of the lower leg.

3. Results

The study observed a temperature increase of 0.5-2 °C after phototherapy with a red laser. When assessing the ratio of power radiated by the skin of patients before and after the procedure, the change is 12-13 %, but in absolute terms it is about 4 mW/cm². From the above estimates, it can be concluded that 70 % of the laser radiation is used for heating, and 30 % is spent on photochemical transformations. When taking into account the photon energy of 3.73×10^{-27} J, it can be assumed that covalent bonds cannot be broken only by radiation, and laser radiation changes only the thermodynamic conditions for reactions in the surface layer of the patient's skin. It should be noted that the

known reactions of the conversion of ATP to ADP are exothermic, and therefore they maintain a special temperature inside tissue cells in the region of 37 °C. Moreover, these reactions require oxygen supply in an amount of 7 ppm/min [18] to maintain thermodynamic equilibrium and chemical potential in the tissues of the surface layer [19]. Otherwise, these reactions attenuate, which leads to slowdown in metabolism, lowering the temperature inside the tissues and imbalance of the chemical potential [19], and this in turn leads to disturbance of microcirculation in the tissues.

The experiment may serve as evidence of microcirculation disturbance. In a random sample of 30 people, the patient's legs were irradiated with the Barva apparatus (radiation power of 50 mW, $\lambda = 635$ nm) in the morning on an empty stomach for 30 minutes. Before irradiation, a blood sampling was taken to conduct an express blood test for sugar concentration using an Accu-Chek Active glucose meter. Blood pressure measurements were also performed with Omron M300. The averaged data are shown in Tables 1, 2 and 3.

Table 1. Change in blood glucose.

	Before irradiation	After irradiation
Left arm	11	11.5
Left leg	3.3	6.3 (toe)
Right leg	3.5	9.1 (toe)

Table 2. Change in blood pressure.

	Before irradiation	After irradiation
Left arm	104/65	123/81
Right arm	103/74	114/74

Table 3. Pulse change.

	Before irradiation	After irradiation
Left arm	75	71
Right arm	76	73

Thermodynamic control of the surface temperature was carried out using a Fluke Ti400 thermal imager with precompensation for the background temperature (T = 296.15 K) and emissivity (ε = 0.86). The emissivity level was selected by comparison with the Omron Gentle Temp 720 thermal resistance. The background temperature was measured on a foil fixed next to the patients. Thermograms frontal anterior and posterior planes of the feet of patients are shown in Fig. 3a,b and Fig. 4a,b.
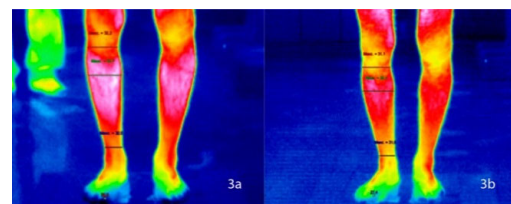
Fig. 3. A thermoregulatory response of the front surface of lower legs (a-before irradiation, b-after irradiation).
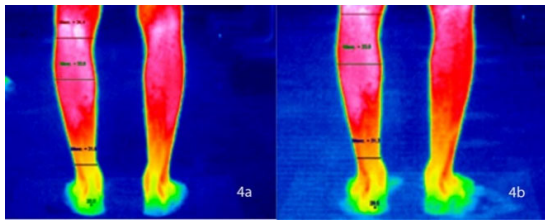
Fig. 4. A thermoregulatory response of the back surface of lower legs (a-before irradiation, b-after irradiation).

The data evident that the temperature distribution is equalized over the entire surface of the lower limb, which indicates changes in thermodynamic equilibrium. Zonal temperature distributions are shown in Fig. 5 a, b and Fig. 6 a, b.
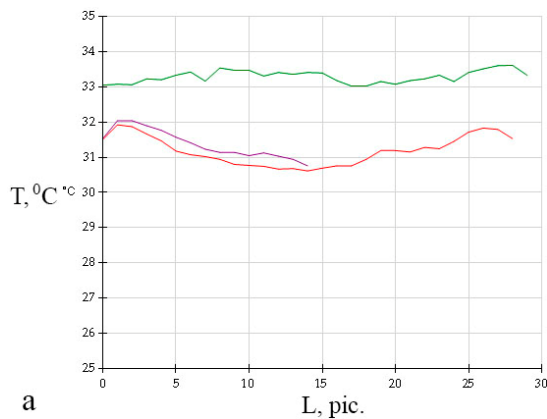
Fig. 5 a. Zonal temperature distributions of the front surface of lower legs before irradiation.
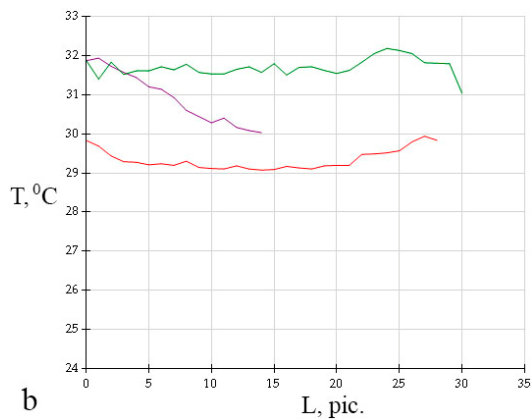
Fig. 5 b. Zonal temperature distributions of the front surface of lower legs after irradiation.

The maximum temperature in the front and rear areas of the knee joint is reduced by 0.9-1.2 °C. In the proximal sections of the anterior and posterior regions of the lower leg the maximum temperature decreases by 0.8-1.4 °C. In the proximal sections of the anterior and posterior regions of the lower leg the maximum temperature decreases by 0.8-1.4 °C. In the distal parts of the anterior and posterior regions of the lower leg the maximum temperature decreases on average by 1 °C. In the surface layer of the foot the maximum temperature increases by 0.5-1.4 °C.
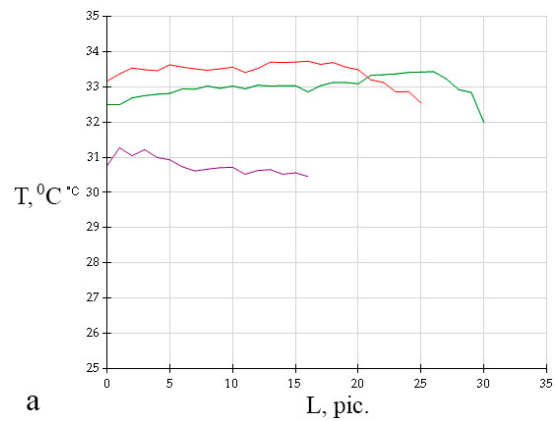
Fig. 6 a. Zonal temperature distributions of the back surface of lower legs before irradiation.
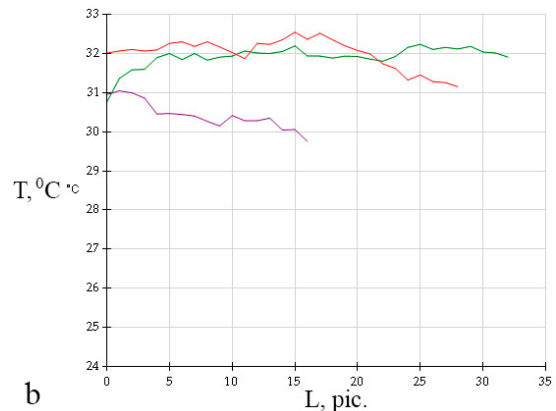
Fig. 6 b. Zonal temperature distributions of the back surface of lower legs after irradiation

This suggests that in the own plantar finger arteries, dorsal finger arteries and the calcaneal rete, the amount of blood increases, so the inner plantar nerves and the heel of the tibial nerve in the affected leg receive enough nutrients to improve the innervation of the surface layer of the foot after irradiation.

The increase in sugar level in the lower limbs indicates improvement in microcirculation. The venous capillaries, venules and veins, as well as the venous part of the arterio-venous anastomoses, expanded in diameter, thereby increasing the difference in osmotic potentials between the arterial and venous channels. With this change in the osmotic potential of a large circle of blood circulation in the lower limbs, blood outflow will increase, which means that blood inflow will also be increased according to Bernoulli's law [20].

All these qualitative changes inhibit the development of DFU and make it possible to avoid LLAs.

However, we must bear in mind that one cannot achieve the same figures of improving microcirculation under conventional heating of the patient. Since when heated, the heat transfer method is convection. With convection heating in the human body, processes will start in which water will accumulate in the surface layer of the skin (since water

has a heat capacity of 4200 J/(kg×C), which is 10 orders of magnitude higher than the heat capacity of dry skin, therefore, the water layer in the transition process is a good storage of thermal energy), thereby forming a protective layer on the skin surface, which will prevent heat transfer to deeper layers. In order to achieve energy transfer through radiation, it would be necessary to increase the emitter temperature over 600 °C, which is dangerous for biological processes.

4. Conclusions

Based on the obtained data on the improvement of microcirculation after irradiation with a red laser, we can assume that the absorption of this wavelength was due to those tissues that do not reflect it, and these are all the tissues other than red. If we take into account a large circle of blood circulation, then the absorption of this electromagnetic radiation was due to veins, venules and capillaries of the venous channel, while the rest of the tissues are considered «transparent» for this spectrum and scattering is neglected. With this absorption, the energy that acted on the venous vessels, and specifically on their walls, increased the potential energy of the elements of the connective tissue. The measurement of the pulse and blood pressure of patients will be taken into account when constructing a polyelastic model of the system for further description of the experiment.

Acknowledgements

References

[1]. International Diabetes Federation, 6th Edition, Brussels, 2013, IDF Diabetes Atlas, http://www.idf.org/diabetesatlas

[2]. DIAMOND Project Group, Incidence and trends of childhood Type 1 diabetes worldwide 1990-1999, *Diabetic Medicine*, Vol. 23, Issue 8, 2006, pp. 857-866.

[3]. P. Zhang, et al., Global epidemiology of diabetic foot ulceration: A systematic review and meta-analysis, *Annals of Medicine*, Vol. 49, Issue 2, 2017, pp. 106-116.

[4]. N. C. Schaper, J. Apelqvist, K. Bakker, The international consensus and practical guidelines on the management and prevention of the diabetic foot, *Current Diabetes Reports*, Vol. 3, Issue 6, 2003, pp. 475-479.

[5]. J. A. Mayfield, et al., Preventive foot care in diabetes, *Diabetes Care*, Vol. 27, 2004, 63.

[6]. S. H. Won, et al., Risk factors associated with amputation-free survival in patient with diabetic foot ulcers, *Yonsei Medical Journal*, Vol. 5, Issue 5, 2014, pp. 1373-1378.

[7]. A. Raghav, et al., Financial burden of diabetic foot ulcers to world: a progressive topic to discuss always, *Therapeutic Advances in Endocrinology and Metabolism*, Vol. 9, Issue 1, 2018, pp. 29-31.

[8]. N. Singh, D. G. Armstrong, B. A. Lipsky, Preventing foot ulcers in patients with diabetes, *Jama*, Vol. 293, Issue 2, 2005, pp. 217-228.

[9]. J.-L. Boulnois, Photophysical processes in recent medical laser developments: A review, *Lasers in Medical Science*, Vol. 1, Issue 1, 1986, pp. 47-66.

[10]. L. Goldman (Ed.), The Biomedical Laser: Technology and Clinical Applications, *Springer Science & Business Media*, 2013.

[11]. P. Schaaf (Ed.), Laser Processing of Materials: Fundamentals, Applications and Developments, Vol. 139. *Springer Science & Business Media*, 2010.

[12]. H.-J. Wei, et al., Determination of optical properties of normal and adenomatous human colon tissues in vitro using integrating sphere techniques, *World Journal of Gastroenterology*, Vol. 11, Issue 6, 2005, 2413.

[13]. E. Hecht, 4th Edition, Optics, *Addison Wesley Longman, Inc.*, 1998.

[14]. M. H. Criqui, Peripheral arterial disease-epidemiological aspects. *Vascular Medicine*, Vol. 6, Issue 1, 2001 pp. 3-7.

[15]. A. J. M. Boulton, The pathway to foot ulceration in diabetes, *Medical Clinics*, Vol. 97, Issue 5, 2013, pp. 775-790.

[16]. L. A. Lavery, et al., Diabetic foot prevention: A neglected opportunity in high-risk patients, *Diabetes Care*, Vol. 33, Issue 7, 2010, pp. 1460-1462.

[17]. M. Schuenke, E. Schulte, et al., General Anatomy and the Musculoskeletal System (Thieme Atlas of Anatomy), *New York*, Thieme, 2005.

[18]. S. S. Simakov, A. S. Kholodov, Computational study of oxygen concentration in human blood under low frequency disturbances, *Mathematical Models and Computer Simulations*, Vol. 1, Issue 2, 2009, pp. 283-295.

[19]. M. Marcotte, M. Le Maguer, Mass transfer in cellular tissues. Part II: Computer simulations vs experimental data, *Journal of Food Engineering*, Vol. 17, Issue 3, 1992, pp. 177-199.

[20]. D. Chapelle, P. Moireau, General coupling of porous flows and hyperelastic formulations – From thermodynamics principles to energy balance and compatible time schemes, *European Journal of Mechanics-B*, Vol. 46, 2014, pp. 82-96.

(008)

Can the Near-field Optics be used for Antiviral Therapy?

V. Lozovski [1,2], N. Rusinchuk [1] and V. Lysenko [2]
[1] Institute of High Technologies Taras Shevchenko National University of Kyiv,
56 Volodymyrska str., 01602 Kyiv, Ukraine
[2] V. Lashkariov Institute of Semiconductor Physics, National Academy of Sciences of Ukraine,
45 Nauki ave., 01000 Kyiv, Ukraine
Tel.: +380445213566
E-mail: v.lozovsk@gmail.com

Summary: When nanoparticles solution is adding to viruses preparation the nanoparticles may adsorb on the virus surface due to Van der Vaals forces. As a result of such interaction a stable nano-sized system is formed. In such system the local electric field is redistributed by the nanoparticles and viruses, which in turn leads to the local field enhancement effect and appearance of 'hot spots' on the virus surface. Consequently, there are local field gradients on the virus surface, and this is the reason for ponderomotive forces acting on the virus. Results of calculations show that on the surface of influenza virus near the Au nanoparticles of 5 nm diameter the forces may lead up to 70 nN. Existed experimental studies of mechanical properties of viruses indicate that mainly the force higher than 30 nN leads to irreversible deformation of the virus particle. Hence, the main idea of the work is to show that ponderomotive forces are the reason for destruction of viruses mixing with nanoparticles, which was demonstrated by microscopy studies for many times. This is the novelty of the work as for now the exact mechanism of the virus destruction under the action of nanoparticles is not known.

Keywords: Nanoparticle, Virus, Antiviral action, Near-field interaction, Local field enhancement, Ponderomotive forces.

1. Introduction

The interaction between nanoparticles and viruses can be the reason of a lost by the virus its infectivity's [1-6]. However, the mechanism of this action is not known. There are different suppositions for this mechanism. We would like to discuss, to extend and to improve the model of influence of nanoparticle on the virus infectivity based on the local-field enhancement effect proposed earlier in [3, 5]. The main feature of proposed model is the arising of the domains of high local field (hot spots) at the virus surface. It was shown that the higher the local field gradient is, the higher antiviral action is without explanation of this dependence. Here we would like to consider this dependence and try to explain it via the action of ponderomotive forces.

2. The Model

The most human viruses have the quasi-spherical shape with linear dimension about 100 nm. The characteristic dimensions of the nanoparticles are about few nanometers. Then, we can use the model when the virus is spherically shelled solid nanoparticle where core is characterized by dielectric constant ε_c^{vir} and the virus shell is characterized by dielectric constant ε_{sh}^{vir}. The dielectric constant of the nanoparticle is ε_p. As is was mentioned, in the system there are the high local field on the virus surface. The domains of high field mean the existence of gradients of the local field at the surface of virus shell. The molecule-receptors at the surface of virus contain the polar sites [7, 8]. Then, the dipole moments of the polar sites are under action of the inhomogeneous field. It means that the forces acting to the molecule-receptors arises (ponderomotive forces):

$$F = -P_i \cdot \partial E_j / \partial x_i. \tag{1}$$

The action of the forces leads to damage the virus surface molecules (up to destruction of virus shell) which can lead to the loose the infection ability of the virus. Sketch of the main stages of the mechanism are shown in Fig. 1.
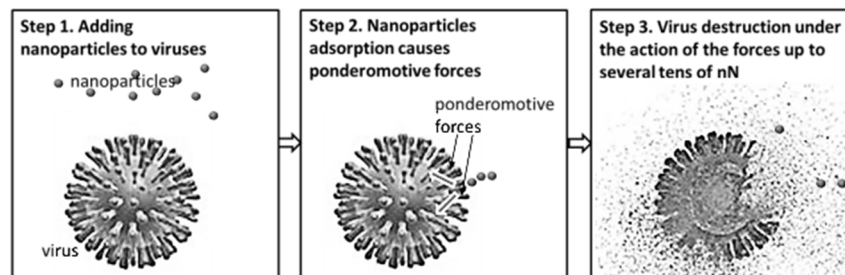
Fig. 1. Sketch of the proposed mechanism of nanoparticles action on the virus.

The effect of the local-field enhancement requests the existence of external field. In the normal conditions the virus-nanoparticle system is situated under day light action. When the additional field source acts to the system one can obtain the influence of the external light on the virus infection ability. The influence was studied in [9] where the addition lighting lead to increase the antiviral properties of nanoparticles. This means that additional illumination by the monochromatic light with resonant wavelength may intensify the antiviral action much. Hence, if we want to evaluate ponderomotive forces at the virus surface we need to consider system of two nanoparticles: small one and big one with a shell and at least, calculate the local-field distribution in the system.

3. Results of Calculation

Using approach described in [10] we calculated the adsorption potential in the system, defined the distance between nanoparticles. Then, for this system of two nanoparticles we calculated the local field distribution and the ponderomotive forces distribution. The maximum force acts at nearly the 1 nm inside the virus from its surface. Direction of forces is schematically shown in Fig. 1 and maximum force value is presented in Table 1.

Table 1. System parameters and results of calculation.

Parameter	System 1	System 2
Virus	Influenza virus H_1N_1	
Outer radius, nm	60	
Inner radius, nm	50	
Dielectric constant of the virus core	2	
Dielectric constant of the virus shell	4	
Nanoparticle material	Au	
Nanoparticle radius, nm	5	20
Nanoparticle dielectric constant	$10.5+1.3i$	
Ponderomotive force max value, nN	75	5

It can be seen, that for smaller nanoparticle the maximum force value is rather high. If we compare this value with experimental results of study of mechanical properties of viruses, we can see that the maximum ponderomotive force is higher than the force needed for irreversible virus deformation [11]. Consequently, these forces may lead to the virus particle destruction, which can be seen on micrographs of viruses with nanoparticles, e.g. in [2].

4. Conclusions

In the work we show that model of the near-field interaction between two nanoparticles allows calculating value of the ponderomotive forces, which

appear at the virus surface. Compare of the calculation results, existed experimental results of mechanical properties of viruses and results of virological experiments with nanoparticles indicate that these forces may lead to the destruction of the virus particle. Thus, for example maximum force value in the system with smaller nanoparticle prevails over the forces value for irreversible virus deformation, while in the system with bigger nanoparticle the force is much lower.

References

[1]. L. Lu, R. W. Y. Sun, R. Chen, C. K. Hui, C. M. Ho, J. M. Luk, G. K. K. Lau, C. M. Che, Silver nanoparticles inhibit hepatitis B virus replication, *Antiviral Therapy*, Vol. 13, Issue 2, 2008, pp. 253-262.

[2]. N. A. Mazurkova, Yu. E. Spitsyna, Z. R. Ismagilov, S. N. Zagrebel'nyi, E. I. Ryabchikova, Interaction of titanium dioxide nanoparticles with influenza virus, *Nanotechnologies in Russia*, Vol. 5, 2010, pp. 417-420.

[3]. V. Lozovski, V. Lysenko, V. Piatnytsia, O. Scherbakov, N. Zholobak, M. Spivak, Physical point of view for antiviral effect caused by the interaction between the viruses and nanoparticles, *Journal of Bionanoscience*, Vol. 6, Issue 2, 2012, pp. 109-112.

[4]. N. Shionoiri, T. Sato, Y. Fujimori, T. Nakayama, M. Nemoto, T. Matsunaga, T. Tanaka, Investigation of the antiviral properties of copper iodide nanoparticles against feline calicivirus, *Journal of Bioscience and Bioengineering,* Vol. 113, Issue 5, 2012, pp. 580-586.

[5]. V. Lysenko, V. Lozovski, M. Lokshyn, Yu. V. Gomeniuk, A. Dorovskih, N. Rusinchuk, Yu. Pankivska, O. Povnitsa, S. Zagorodnya, V. Tertykh, Nanoparticles as antiviral agents against adenoviruses, *Advances in Natural Sciences: Nanoscience and Nanotechnology*, Vol. 9, Issue 2, 2018, 025021.

[6]. S. Galdiero, A. Falanga, M. Vitiello, M. Cantisani, V. Marra, M. Galdiero, Silver nanoparticles as potential antiviral agents, *Molecules*, Vol. 16, Issue 10, 2011, pp. 8894-8918.

[7]. K. Grünewald, P. Desai, D.C. Winkler, J. B. Heymann, D. M. Belnap, W. Baumeister, A. C. Steven, Three-dimensional structure of herpes simplex virus from cryo-electron tomography, *Science*, Vol. 302, Issue 5649, 2003, pp. 1396-1398.

[8]. E. E. Heldwein, H. Lou, F. C. Bender, G. H. Cohen, R. J. Eisenberg, S. C. Harrison, Crystal structure of glycoprotein B from herpes simplex virus 1, *Science*, Vol. 313, Issue 5784, 2006, pp. 217-220.

[9]. O. Khylko, N. Rusinchuk, O. Shydlovska, M. Lokshyn, V. Lozovski, V. Lysenko, A. Marynin, A. Shcherbakov, M. Spivak, N. Zholobak, Influence of the virus-nanoparticles system illumination on the virus infectivity, *Journal of Bionanoscience,* Vol. 10, Issue 6, 2016, pp. 453-459.

[10]. V. Lozovski, N. Rusinchuk, T. Vasiliev, Repulsive interaction between two different-sized nanoparticles due to self-consistency, in *Proceedings of the IEEE 39ᵗʰ International Conference on Electronics and Nanotechnology (ELNANO'19),* Kyiv, Ukraine, 16-18 April 2019, pp. 253-256.

[11]. P. J. de Pablo, M. G. Mateu, Mechanical properties of viruses, *Subcell Biochem.,* Vol. 68, 2013, pp. 519-551.

(009)

Optical Sensing of Biological Liquids by Means of Gold Nanoparticles with Biospecific Surfaces

<u>V. Z. Lozovski</u> and M. A. Razumova

Institute of High Technologies, Taras Shevchenko National University of Kyiv, 64 Volodymyrska Str.,
01601 Kyiv, Ukraine
E-mail: v.lozovsk@gmail.com

Summary: The optical absorption spectra of colloidal solution of specifically covered gold nanoparticles were calculated in the framework of the effective susceptibility concept and method of the Green functions. The change in shell thickness of modified gold nanoparticles are caused by binding between the molecules-analytes and the antibody conjugated to the gold nanoparticle. The increase in the nanoparticle shell thickness and the effective dielectric constant of the shell cause the shift of the frequency of the localized surface plasmon resonance. This frequency shift manifested in the absorption spectra can be used for sensing of analyte in the bioliquid.

Keywords: Nanocomposite, Plasmon resonance, Effective susceptibility, Local field, Absorption, Biospecific interaction.

1. Introduction

The plasmonic nanoparticles with biospecific surfaces can play a role of sensitive device [1] for sensing both the biomolecules concentration in the bioliquid and biospecific reaction (BSR) (for example, by interaction of antigen-antibody type). The methods of nanoparticles conjugation to antibodies are good developed and considered in [2].

Studies of biosensors, which use biospecific binding on the functionalized surface have shown that the magnitude of the wavelength shift of localized surface plasmon resonance depends on the size and density of the molecules on the surface of the nanoparticle and that the detection limit of the sensor is determined by the surface-confined binding constant between the molecule-analyte and substrate (see, for example, [1]). In our previous works [3-5] we have considered nanocomposite thin films with embedded metal nanoparticles with biospecific surfaces in Teflon matrix for implementation in biosensorics. We have calculated optical response of nanocomposite film by applying the local-field method of the effective medium theory in the framework of the effective susceptibility concept. In this work we have developed the method for a case of colloidal solution of gold nanoparticles with biospecific surfaces.

2. Linear Response of Colloidal Solution of Nanoparticles

Two types of changes in complex nanoparticles can be included in theoretical model under consideration, namely, the change in the thickness of the shell and change in the effective dielectric constant of the shell with a simultaneous change in its thickness (see schematic in Fig. 1). The change in the thickness of the shell results in the change of the volume fraction of nanoparticles f (and corresponding volume fraction of gold core in the modified nanoparticles f_1) in the solution. The values of these parameters depend on the analyte molecules concentration in the bioliquid.

Fig. 1. Modified nanoparticle (left) which is covered by other shell due to antigen-antibody interactions (right).

The dielectric function of the effective medium of the nanocomposite of spherical particles is

$$L_{il}(\mathbf{k},\omega) = \left[\delta_{il} + k_m^2 f G_{il}(\mathbf{k},\omega) \mathrm{X}^{(p)}(\omega) \right]^{-1}, \quad (1)$$

where ω and $\mathbf{k}$ are the frequency and wavevector of electromagnetic wave, respectively. $k_m = \omega\sqrt{\varepsilon_m}/c$, c is the speed of light, ε_m is the dielectric constant of the liquid (matrix) without nanoparticles. f is the volume fraction of nanoparticles in the solution. $\mathbf{G}(\mathbf{k},\omega)$ is the Fourier transform of the electrodynamic Green function, describing the electromagnetic field propagation inside the homogeneous and isotropic liquid without nanoparticles. The effective susceptibility of a coated spherical particle is

$$\mathrm{X}^{(p)}(\omega) = 3\frac{(\varepsilon_2 - \varepsilon_m)(\varepsilon_1 + 2\varepsilon_2) + f_1(\varepsilon_1 - \varepsilon_2)(\varepsilon_m + 2\varepsilon_2)}{(\varepsilon_2 + 2\varepsilon_m)(\varepsilon_1 + 2\varepsilon_2) + f_1(2\varepsilon_2 - 2\varepsilon_m)(\varepsilon_1 - \varepsilon_2)}, \quad (2)$$

where a_2 is the outer radius, ε_1 and ε_2 are the core (of radius a_1) and shell dielectric functions, respectively. The core volume fraction is

$$f_1 = a_1^3 / a_2^3 \quad (3)$$

3. Absorption Spectra of Colloidal Solution

Figs. 2 and 3 show the numerically calculated dependence of the absorption (in arbitrary units) on the frequency (in units of the frequency of the bulk plasmons ω_p in gold) for colloidal solution of nanoparticles with the different values of volume fraction of nanoparticles f and the effective dielectric constant of the shell ε_2 correspondingly presented in inset. Red curves correspond to the initial inclusions conjugated to antibodies; other curves correspond to the treated with solution of complementary molecules (of the different concentration) resulting in the different increases in the shell thickness.
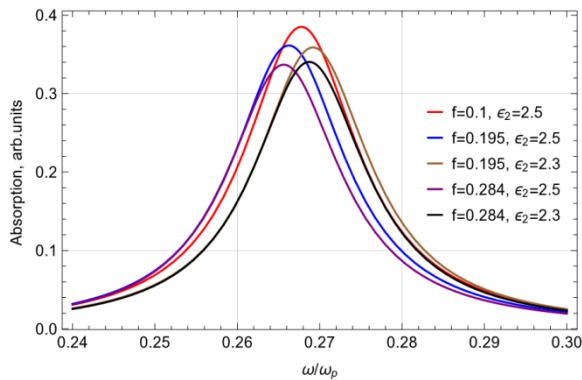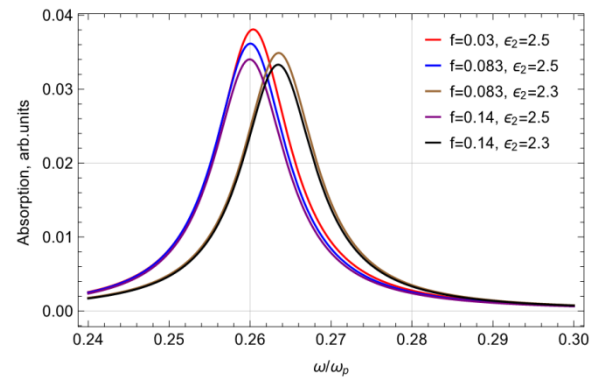

Fig. 2. The changing of absorption profile when the shell is increased in thickness as a result of the biospecific binding with the complementary 5-nm-molecules to the surface of inclusion particles of 7-nm-radius Au core.

4. Conclusion

The localized surface plasmon resonance manifested in absorption spectra can be used for sensing the change in shell thickness of modified gold nanoparticles caused by binding between the analyte molecules and the antibody conjugated to the gold nanoparticle. Increase in the nanoparticle shell thickness and the change of the effective dielectric constant of the shell due to bindings of analytes to the nanoparticles surface results in the shift of the frequency of the plasmon resonance. The different change trends are obtained in a case for "big" and "small" molecules of analyte which by binding cause increase of the shell of the nanoparticles.

Exploring the change in the absorption profile, one can detect whether biospecific reaction took place. Note that there can be two different directions of exploring. Firstly, assuming that the concentration of molecules of the antigen (analyte) is sufficient that for some time all the molecules of the antibodies have attached the molecules of the antigen. In this case, the thickness of the shell will be changed without changing the dielectric constant of its substance (the molecules

of antibodies and antigens have the same electrodynamic properties). The blue and purple curves in the Figs. 2 and 3 correspond to this case.

Fig. 3. The changing of absorption profile when the shell is increased in thickness as a result of the biospecific binding with the complementary 25-nm- molecules to the surface of inclusion particles of 12-nm-radius Au core.

Another assumption is that the concentration of analyte molecules is low and only some of the antibody molecules can be bound antigen molecules. In this case, it can be assumed that the effective thickness of the shell has changed and reached its value, as in the previous case (the geometry of the molecular complex of antigen-antibody is constant), and the effective dielectric constant of the shell is decreased (since the shell will became optically less dense). In this case, the curves of the absorption spectra are blue-shifted.

References

[1]. J. Zhao, X. Zhang, C. R. Yonzon, A. J. Haes, R. P. Van Duyne, Localized surface plasmon resonance biosensors, *Nanomedicine*, Vol. 1, Issue 2, 2006, pp. 219–228.

[2]. A. J. Sivaram, A. Wardiana, C. B. Howard, S. M. Mahler, K. J. Thurecht, Recent advances in the generation of antibody–nanomaterial conjugates, *Advanced Healthcare Materials*, Vol. 7, Issue 1, 2018, 1700607.

[3]. V. Lozovski, M. Razumova, The local field effects in optical response of nanocomposite thin films, An implementation in sensorics of biospecific interactions, in *Proceedings of the IEEE 35th International Conference on Electronics and Nanotechnology (ELNANO'15)*, 2015, pp. 333-336.

[4]. V. Lozovski, M. Razumova, The effective susceptibility concept implementation for nanocomposite systems and sensing, in *Proceedings of the Progress in Electromagnetic Research Symposium (PIERS'16)*, 2016, pp. 2708-2712.

[5]. V. Lozovski, M. Razumova, Plasmon resonances for biospecific interactions sensing, *Journal of Photonic Materials and Technology*, Vol. 1, Issue 2, 2015, pp. 33-39.

(023)

Spirally Polarized Sources with Cosine-circular Coherence

J. C. G. de Sande [1], G. Piquero [2], R. Martínez-Herrero [2], M. Santarsiero [3] and F. Gori [3]

[1] Universidad Politécnica de Madrid, ETSIS de Telecomunicación, Campus Sur, 28031 Madrid, Spain

[2] Universidad Complutense de Madrid, Departamento de Óptica, 28040 Madrid, Spain

[3] Università Roma Tre, Dipartimento di Ingegneria, V. Volterra 62, Rome 00146, Italy

Tel.: + 34 910673373

E-mail: juancarlos.gonzalez@upm.es

Summary: A type of partially coherent and nonuniformly polarized sources is proposed. This type of sources belongs to those with cosine-circular coherence, that is, they present a cosine-type dependence on the square of the distances of the points from the source center. On the other hand, these sources are endowed with a non-uniform polarization pattern across their transverse section. In particular, the electric field is linearly polarized and, at each point of the transverse section, symmetrically oriented with respect to the source center, so that the electric field lines form spirals. These sources will be denoted as "Spirally polarized sources with cosine-circular coherence". Analytical expessions for the generated field upon free propagation under paraxial conditions are derived. The intensity and polarization at each plane is studied. It is demonstrated that, under particular conditions, these type of fields remains spirally polarized but with an intensity profile that changes at each z-plane. A simple procedure of synthesis of such sources is schematized.

Keywords: Polarization, Coherence, Propagation, Physical optics, Statistical optics.

1. Introduction

One of the topics that is receiving a lot of interest in recent years is the proposal of new physically realizable sources with special coherence and polarization characteristics. Several models of scalar partially coherent sources with peculiar coherence characteristics have recently been proposed [1-8], such as sources with either circular or radial coherence [1-5]. These type of sources are described by a cross spectral density (CSD) function that only depends on the difference of the modulus of the position vectors and have been shown to present self-focusing [4,5,7]. Sources whose CSD has a functional form of cosine-type will be studied and, in particular, sources that present a cosine-type dependence on the square of the distances of the points from the source center [6]. In the scalar case, it has been demonstrated that the field generated from these sources presents interesting properties in propagation under paraxial conditions. For instance, the intensity of the propagated field changes and shows a maximum at a certain plane that, in general, does not coincide with the waist plane [4,5,7].

On the other hand, it has been shown that spirally polarized beams (SPBs) [9-14], which include radially and azimuthally polarized as particular cases, are useful in some application fields, such as microscopy, particle manipulation, polarimetry, etc. (see for example, [15-26]). SPBs present linearly polarization across the transverse beam section but the electric field forms a fixed angle with the radial direction at each point, so that the azimuth changes from one point to another. They belong to the so called nonuniformly totally polarized beams [25-29].

Usually, a circularly symmetric intensity is considered for totally coherent SPBs, that is, their electric field amplitude depends only on the radial distance to the beam axis. A typical example of amplitude dependence is a Laguerre-Gauss function, in which case not only the polarization but also the intensity remains invariant in propagation, up to a scale factor. Partially coherent SPBs have also been theoretically considered and experimentally synthesized (see for example [10] and [14]).

In this work, sources presenting cosine-circular coherence properties and spiral polarization pattern across the transverse plane will be considered. For these kind of sources, analytical expressions for the beam coherence-polarization matrix [30] at each transverse plane are derived. Special attention will be paid to the evolution of the intensity and the polarization pattern in free space propagation of the beam radiated from the source. It will be shown that, under certain conditions, the beam remains spirally polarized at each plane but the intensity reaches a maximum value in a plane that will be different than that of the beam waist. The maximum intensity value and the position of the plane at which this maximum is reached depend on the coherence characteristics of the source. The results will be compared with two different cases: a totally coherent SPB, and a partially coherent beam with circular coherence but totally and uniformly polarized.

Acknowledgements

References

[1]. M. Santarsiero, R. Martínez-Herrero, D. Maluenda, J. C. G. de Sande, G. Piquero, F. Gori, Partially coherent sources with circular coherence, *Optics Letters,* Vol. 42, 2017, pp. 1512-1515.

[2]. M. Santarsiero, R. Martínez-Herrero, D. Maluenda, J. C. G. de Sande, G. Piquero, F. Gori, Synthesis of circularly coherent sources, *Optics Lett*ers, Vol. 42, 2017, pp. 4115-4118.

[3]. G. Piquero, M. Santarsiero, R. Martínez-Herrero, J. C. G. de Sande, M. Alonzo, F. Gori, Partially coherent sources with radial coherence, *Optics Lett*ers, Vol. 43, 2018, pp. 2376-2379.

[4]. R. Martínez-Herrero, G. Piquero, J. C. G. de Sande, M. Santarsiero, Besinc pseudo-schell model sources with circular coherence, *Applied Sciences,* Vol. 9, Issue 13, 2019, 2716.

[5]. J. C. G. de Sande, R. Martínez-Herrero, G. Piquero, M. Santarsiero, F. Gori, Pseudo-Schell model sources, *Optics Express,* Vol. 27, Issue 4, 2019, pp. 3963-3977.

[6]. G. Piquero, J. de la Riva, R. Martínez-Herrero, J. C. G. de Sande, M. Santarsiero, Cosine-circular partially coherent sources, in *Proceedings of the Reunión Española de Optoelectrónica (OPTOEL'19),* Zaragoza, Spain, 3-5 July 2019, SP3MIS09.

[7]. C. Ding, M. Koivurova, J. Turunen, L. Pan, Self-focusing of a partially coherent beam with circular coherence, *Journal of the Optica A: Pure and Applied Optics,* Vol. 34, 2017, pp. 1441-1447.

[8]. M. W. Hyde, S. R. Bose-Pillai, R. A Wood, Synthesis of non-uniformly correlated partially coherent sources using a deformable mirror, *Applied Physics Letters,* Vol. 111, 2017, 101106.

[9]. F. Gori, Polarization basis for vortex beams, *Journal of the Optical Society of America A,* Vol. 18, 2001, pp. 1612-1617.

[10]. J. Tervo, Azimuthal polarization and partial coherence, *Journal of the Optical Society of America A*, Vol. 20, 2003, pp. 1974-1980.

[11]. R. Borghi, M. Santarsiero, Nonparaxial propagation of spirally polarized optical beams, *Journal of the Optical Society of America A*, Vol. 21, 2004, pp. 2029-2037.

[12]. R. Martínez-Herrero, P. M. Mejías, Propagation of light fields with radial or azimuthal polarization distribution at a transverse plane, *Optics Express,* Vol. 16, 2008, pp. 9021-9033.

[13]. V. Ramírez-Sánchez, G. Piquero, M. Santarsiero, Generation and characterization of spirally polarized fields, *Journal of the Optica A: Pure and Applied Optics*, Vol. 11, 2009, 085708.

[14]. V. Ramírez-Sánchez, G. Piquero, M. Santarsiero, Synthesis and characterization of partially coherent beams with propagation-invariant transverse polarization pattern, *Optics Communications,* Vol. 283, 2010, pp. 4484-4489.

[15]. V. G. Niziev, A. V. Nesterov, Influence of beam polarization on laser cutting efficiency, *Journal of Physics D: Applied Physics,* Vol. 32, 1999, pp. 1455-1461.

[16]. Q. Zhan, J. R. Leger, Focus shaping using cylindrical vector beams, *Optics Express,* Vol. 10, 2002, pp. 324-331.

[17]. R. Dorn, S. Quabis, G. Leuchs, Sharper focus for a radially polarized light beam, *Physical Review Letters*, Vol. 91, 2003, 233901.

[18]. Q. Zhan, Trapping metallic rayleigh particles with radial polarization, *Optics Express*, Vol. 12, 2004, pp. 3377-3382.

[19]. Q. Zhan, Cylindrical vector beams: from mathematical concepts to applications, *Advances in Optics and Photonics,* Vol. 1, 2009, pp. 1-57.

[20]. J. C. G. de Sande, M. Santarsiero, G. Piquero, Spirally polarized beams for polarimetry measurements of deterministic and homogeneous samples, *Optics and Lasers in Engineering,* Vol. 91, 2017, pp. 97-105.

[21]. H. Zhang, J. Li, K. Cheng, M. Duan, Z. Feng, Trapping two types of particles using a focused partially coherent circular edge dislocations beam, *Optics & Laser Technology,* Vol. 97, 2017, pp. 191-197.

[22]. J. C. G. de Sande, G. Piquero, M. Santarsiero, Polarimetry with azimuthally polarized light, *Optics Communications,* Vol. 410, 2018, pp. 961-965.

[23]. C. Rosales-Guzmán, B. Ndagano, A. Forbes, A review of complex vector light fields and their applications, *Journal of Optics*, Vol. 20, 2018, 123001.

[24]. J. Chen, C. Wan, Q. Zhan, Vectorial optical fields: Recent advances and future prospects, *Science Bulletin*, Vol. 63, 2018, pp. 54-74.

[25]. G. Piquero, R. Martínez-Herrero, J. C. G. de Sande, M. Santarsiero, Synthesis and characterization of non-uniformly totally polarized light beams: Tutorial, *Journal of the Optica A: Pure and Applied Optics,* Vol. 37, 2020, pp. 591-605.

[26]. R. Martínez-Herrero, P. M. Mejías, G. Piquero, Characterization of Partially Polarized Light Fields (W. T. Rhodes, Ed.), *Springer*, 2009.

[27]. G. Piquero, J. Vargas-Balbuena, Non-uniformly polarized beams across their transverse profiles: An introductory study for undergraduate optics courses, *Eur. J. Phys.*, Vol. 25, 2004, pp. 793-800.

[28]. G. Piquero. L. Monroy, M. Santarsiero, M. Alonzo, J. C. de Sande, Synthesis of full Poincaré beams by means of uniaxial crystals, *Journal of Optics*, Vol. 20, Issue 6, 2018, 065602.

[29]. J. C. Suárez-Bermejo, J. C. G. de Sande, M. Santarsiero, G. Piquero, Mueller matrix polarimetry using full Poincaré beams, *Optics and Lasers in Engineering*, Vol. 122, 2019, pp. 134-141.

[30]. F. Gori, M. Santarsiero, R. Borghi, A sufficient condition for non-negative definiteness of cross-spectral densities, in *Proceedings of the Frontiers in Optics Conference*, 2006, p. JWD42.

(024)

Spectroscopy of Stationary Ultracold Ca-40 Plasma Prepared by Continuous Wave Lasers

B. B. Zelener [1], S. A. Saakyan [1], K. P. Galstyan [1], E. V. Vilshanskaya [1] and V. A. Sautenkov [1]

[1] Joint institute for high temperarures RAS, Laboratory of laser cooling and ultracold plasma, Izhorskaya str. 13, Bd.2, 125412 Moscow, Russian Federation

Tel.: + 74953620778, fax: + 74954859922

E-mail: bobozel@mail.ru

Summary: We report the spectroscopic studies of the stationary ultracold calcium plasma which is prepared via continuous wave optical excitation. Preparation of the plasma is performed in magneto-optical trap by using two excitation cw lasers with wavelengths 423 nm and 390 nm. The fluorescence resonances of Ca-40 ions on transition $4\,^2S_{1/2}$-$4\,^2P_{1/2}$ are recorded by using probe cw laser with wavelength 397 nm. We can change the initial temperature of free electrons in calcium plasma by tuning the second excitation laser above the ionization potential. For estimations of ion temperature we use the measured widths of the fluorescence resonances. The obtained results can be used for preparation of strongly coupled ultracold plasma.

**Keywords:** Laser spectroscopy, Ultracold plasma, Magnetooptical trap.

1. Introduction

The spectroscopic studies of the stationary ultracold calcium plasma which is prepared via continuous wave optical excitation are reported. This approach is realized for the first time. Previously published papers describe the creation and study of ultracold neutral plasma from Ca and Sr atoms by using pulse lasers [1, 2]. The advantages of these previous researches are the possibilities to create and study the high density plasma. In our continuous regime we can control all stationary processes of the creation and development of ultracold plasma cloud in the time. Analytical estimations and numerical thermo-dynamical calculations by method Monte-Carlo indicate the possibility to prepare liquid or crystal like-structures in a strongly coupled ultracold plasma, as well as in an ultracold dense ensemble of Rydberg atoms [3]. The possibility to create the spatial structures, as well as the ability to use a resonant laser to manipulate the excitation and degree of interaction of ultracold ions and ultracold Rydberg atoms, open the way to make components for quantum information technologies.

2. Experimental Results

Preparation of the calcium plasma is performed in magneto-optical trap by using two excitation lasers with wavelengths 423 nm and 390 nm [4]. In Fig. 1 the picture of calcium ions cloud recorded by using probe laser with wavelength 397 nm and CCD camera.

The fluorescence resonances of Ca-40 ions on transition $4^2S_{1/2}$-$4^2P_{1/2}$ are recorded by using probe laser with wavelength 397 nm, see Fig. 2.
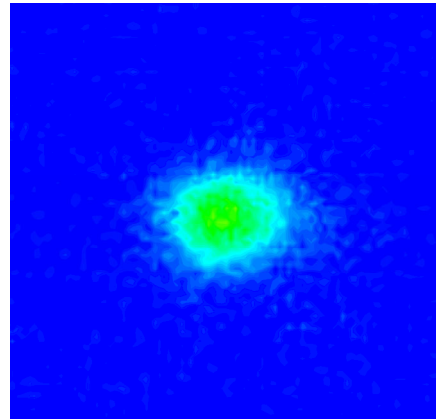
Fig. 1. The optical image of calcium ions cloud. The distribution cloud density quite well is describe by Gaussian function with FWHM alone horizontal axis 1.3 mm and vertical axes 1.1 mm.
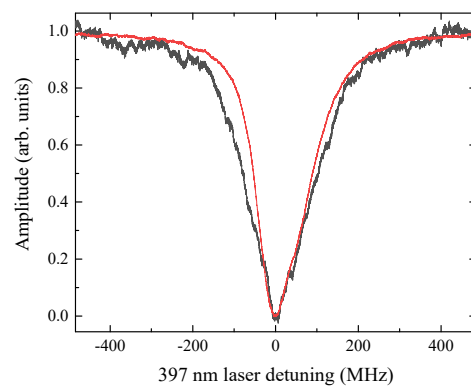
Fig. 2. The fluorescence resonances of Ca-40 ions on transition $4^2S_{1/2}$-$4^2P_{1/2}$. Black curve - excitation with laser detuning 2000 GHz, T_e = 64 K, T_i = 0.34 K. Red curve – excitation with laser detuning 0.2 GHz, T_e = 6 mK, T_i = 0.17 K.

We can change the initial temperature of free electrons T_e in calcium plasma by tuning the second excitation laser above the ionization potential. The thermal motion of free electrons influences on ions temperature T_i. For estimations of the ion temperature we use the measured widths of the fluorescence resonances. The widths of the resonances in Fig. 2 are 150 MHz and 200 MHz for electron temperatures of 6 mK and 64 K. The widths of the resonances are obtained by fitting fluorescence resonances with Gaussian functions, but as you can see, the resonances are not symmetrical due to an expansion of the ion cloud. These asymmetries give uncertainties of the order of 10 MHz. Ion temperature is obtained by solving the density matrix equation. The calculated ion temperature is 0.17 K and 0.34 K for T_e = 6 mK and 64 K respectively.
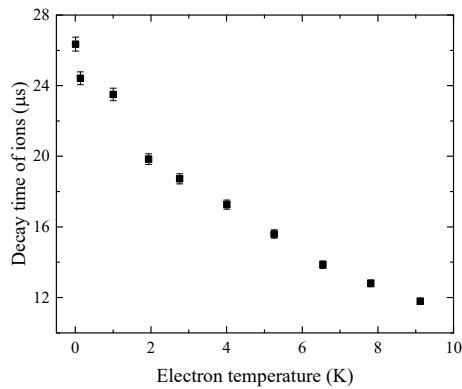
Fig. 3. Decay time of the ions cloud versus the initial temperature of free electrons.

We measure a decay time when the ions fluorescence is reduced to a level 1/e for different initial temperatures of free electrons in calcium plasma after switch off the laser excitation of the plasma (Fig. 3). It can be seen that with an increase in the electron temperature, the decay time of the ions cloud decreases rapidly.

Also we start to investigate hybrid plasma resonances by applying an additional radio-frequency field.

3. Conclusions

We present study of the stationary ultracold calcium plasma which is prepared via continuous wave optical excitation. These results can be useful for preparation of strongly coupled ultracold plasma.

Acknowledgements

References

[1]. T. K. Langin, G. M. Gorman, T. C. Killian, Laser cooling of ions in a neutral plasma, *Science*, Vol. 363, Issue 6422, 2019, pp. 61-64.

[2]. M. Lyon, S. D. Bergeson, A. Diaw, M. S. Murillo, Using higher ionization states to increase Coulomb coupling in an ultracold neutral plasma, *Physical Review E*, Vol. 91, Issue 3, 2015, 033101.

[3]. M. Bonitz, B. B. Zelener, B. V. Zelener, E. A. Manykin, V. S. Filinov, V. E. Fortov, Thermodynamics and correlation functions of an ultracold nonideal Rydberg plasma, *Journal of Experimental and Theoretical Physics*, Vol. 98, Issue 4, 2004, pp. 719-727.

[4]. B. B. Zelener, I. D. Arshinova, A. A. Bobrov, E. V. Vilshanskaya, S. A. Saakyan, V. A. Sautenkov, B. V. Zelener, V. E. Fortov, Coherent excitation of rydberg states in the gas of cold 40 Ca atoms, *Journal of Experimental and Theoretical Physics Letters*, Vol. 108, Issue 12, 2019, pp. 820-824.

Simulation of Mueller Matrix Polarimetry with Full Poincaré Beams and a CCD Camera

J. C. Suárez-Bermejo [1], J. C. González de Sande [2], M. Santarsiero [3] and G. Piquero [4]
[1] Universidad Politécnica de Madrid, Materials Science Department, Av. de la Memoria 4, 28040 Madrid, Spain
[2] Universidad Politécnica de Madrid, ETSIS de Telecomunicación, Campus Sur, 28031 Madrid, Spain
[3] Università Roma Tre, Dipartimento di Ingegneria, V. Volterra 62, Rome 00146, Italy
[4] Universidad Complutense de Madrid, Departamento de Óptica, 28040 Madrid, Spain
Tel.: + 34 910676214
E-mail: juancarlos.suarez@upm.es

Summary: Full Poincaré beams have already been applied in polarimetry for determining the Mueller matrix of homogeneus samples. This matrix could be obtained from the measured Stokes parameters at four different points of the transverse section of the full Poincaré beam before and after the sample. As a full Poincaré beam contains all the possible states of polarization in its transverse section, the change of the state of polarization in the whole section could be exploited to get a better accuracy in the determination of the Mueller matrix. Then, a polarization state analyzer with a CCD camera allows to obtain Stokes parameters maps for the input and output beams. The analysis of these maps could be usefull in order to obtain the Mueller matrix with reduced experimental errors. Several simulations will be presented and compared to show the feasibility of this proposal.

Keywords: Polarization, Polarimetry, Full Poincaré beams, CCD, Error sources.

1. Introduction

The analysis of the changes in polarization pattern of a non uniformly polarized beam [1] has been proposed for Mueller matrix polarimetry [2-6]. Full Poincaré beams (FPBs) are a class of non uniformly totally polarized beams characterized by presenting all possible states of totally polarized light in their transverse section [7]. This feature can be exploited in polarimetric applications where this kind of beams can be used as a polarization state generator in parallel. It has recently been shown that a particular type of FPB is easily synthesized by focusing a linearly polarized beam onto a plane parallel slab of uniaxial crystal with its optic axis perpendicular to the slab [8,9]. For this particular FPB, all possible states of polarization can be found in a semicircle in the beam transverse section of a given radius r_M. This radius is related with the thickness of the slab and the refractive indexes of the crystal at the working wavelength. By measuring the Stokes parameters at four different points of the transverse section of a FPB before and after a homogeneous sample, the Mueller matrix of the sample can be determined [6,10].

Here, we propose to use a CCD camera instead of a point-like detector to measure the Stokes parameters in the whole section of the FPB. Then, many sets of four pixels can be used to obtain the Mueller matrix of the sample. Simulation of the measurement process allows to show the potential improvement that could be achieved by averaging the results for a large number of combinations of measurement points.

2. Simulation of a Polarimetric Measurement with a FPB and a CCD Camera

Stokes vector at a given point in the transverse section of a light beam, $\vec{S}^{in}$, can be obtained by measuring the light intensity in such a point when the light passes by linear polarizer at four different orientations of its transmission axis, namely 0, $\pi/4$, $\pi/2$, and $-\pi/4$, and after the combination of a quarter wave phase plate and the same polarizer at $\pi/4$ and $-\pi/4$, which constitutes a polarization state analyzer (PSA). By recording the intensity with a camera, a map of the Stokes parameters can be obtained. If the same light beam passes through a given sample, the state of polarization changes depending on the sample characteristics, expressed as a 4x4 Mueller matrix, $\hat{M}$, as $\vec{S}^{out} = \hat{M}\vec{S}^{in}$, where $\vec{S}^{out}$ represents the Stokes vector of the output beam [11].

By measuring the Stokes parameters of the output beam for at least four different states of polarization of the input beam, the Mueller matrix of the sample can be recovered. When the input beam is a FPB and the Stokes parameters are measured in its transverse section with a CCD camera before and after the sample, many combinations of four different pixels can be used to determine the Mueller matrix of the sample.

Considering ideal optical elements (polarizer and quarter wave plate) that are perfectly oriented, an important source of error is the inaccuracy of the measurement of the light intensity in each pixel for each of the registered images. In order to evaluate this source of error, the values of the Stokes parameters for

the considered FPB are theoretically calculated [3]. Then the Stokes parameters for the output beam after passing through an ideal sample are also calculated. The intensity registered by an ideal CCD camera when the input and output beams passes through any of the six configurations of the basic PSA can also be theoretically calculated. For each of these simulated images, a random noise is added (Gaussian added noise). From these noisy images, the Stokes parameters map for the input and output beam are calculated, and from these Stokes parameters, the Mueller matrix of the sample is recovered. The differences between the recovered Muller matrix and the actual one will be evaluated. Repeating this process for many sets of four selected pixels and averaging the results, an average Mueller matrix can be found. It will be shown that this averaged matrix is closer to the theoretical one than any of the individually calculated matris for a given set of pixels.

The simulation will be developed following several criteria for the selection of the sets of pixels where to evaluate Stokes parameters from the noisy simulated images. Different types of weighted averaging will also be tested and compared.

The results obtained from these simulations will be useful for deciding a measurement strategy during the experimental development of this polarimetric method.

Acknowledgements

References

[1]. G. Piquero, R. Martínez-Herrero, J. C. G. de Sande, M. Santarsiero, Synthesis and characterization of non-uniformly totally polarized light beams: Tutorial, *Journal of the Optical Society of America A*, Vol. 37, Issue 4, 2020, pp. 591-605.

[2]. S. Tripathi, K. C. Toussaint, Rapid Mueller matrix polarimetry based on parallelized polarization state generation and detection, *Optics Express*, Vol 17, Issue 24, 2009, pp. 21396-21407.

[3]. F. Kenny, O. Rodríguez, D. Lara, C. Dainty, Vectorial polarimeter using an inhomogeneous polarization state generator, in *Proceedings of the Frontiers in Optics 2011 Conference*, *Laser Science XXVII*, 2011, p. FThQ5.

[4]. J. C. G. de Sande, M. Santarsiero, G. Piquero, Spirally polarized beams for polarimetry measurements of deterministic and homogeneous samples, *Optics and Lasers in Engineering*, Vol. 91, 2017, pp. 97-105.

[5]. J. C. G. de Sande, G. Piquero, M. Santarsiero, Polarimetry with azimuthally polarized light, *Optics Communication*, Vol. 410, 2018, pp. 961-965.

[6]. J. C. Suárez-Bermejo, J. C. G. de Sande, M. Santarsiero, G. Piquero, Mueller matrix polarimetry using full Poincaré beams, *Optics and Lasers in Engineering*, Vol. 122, 2019, pp. 134-141.

[7]. A. M. Beckley, T. G. Brown, M. A. Alonso, Full Poincaré beams, *Optics Express*, Vol. 18, Issue 10, 2010, pp. 10777-10785.

[8]. G. Piquero, J. Vargas-Balbuena, Non-uniformly polarized beams across their transverse profiles: An introductory study for undergraduate optics courses, *European Journal of Physics*. Vol. 25, 2004, pp. 793-800.

[9]. G. Piquero. L. Monroy, M. Santarsiero, M. Alonzo, J. C. de Sande, Synthesis of full Poincaré beams by means of uniaxial crystals, *Journal of Optics*, Vol. 20, Issue 6, 2018, 065602.

[10]. J. C. Suárez-Bermejo, J. C. G. de Sande, M. Santarsiero, G. Piquero, Analysis of the errors in polarimetry with full Poincaré beams, in *Proceedings of the Progress In Electromagnetics Research Symposium (PIERS'19)*, 2019, pp. 2621-2627.

[11]. R. A. Chipman, Polarimetry, in Handbook of Optics (M. Bass, Ed.), *McGraw-Hill*, 2010.

(038)

Two-wavelengths Interferometry as Confocal Microscope Extension to Provide 3D Imaging Capabilities

<u>M. Stašík</u> [1], F. Kaván [1], M. Mach [1], K. Sedláčková [1], J. Kredba [1] and M. Špína [1]
[1] Technical University of Liberec, Institute of New Technologies and Applied Informatics, Studentská 1402/2,
461 17 Liberec, Czech Republic
Tel.: + 420604534584
E-mail: marek.stasik@tul.cz

Summary: Digital holographic microscopy is a powerful 3D imaging tool for industrial surface inspection and scientific experiment evaluation, as it provides similar lateral resolution as classical microscope and very fine axial resolution. This paper presents the results and the findings of the experimental holographic microscope development. The device construction is described. The emphasis of the research lays on two-wavelength interferometry combined with a phase shifting. The phase shifting was done using acousto-optics modulators which allow precisely tune light frequency. A developed enhanced measurement procedure, which increases versatility by increasing dynamic range, is described. Developed algorithms for data evaluation are presented and measured experimental data visualised.

Keywords: Microscope, Interferometry, Phase shifting, Bragg cell, Acousto-optic modulator, Multiwavelength interferometry, High dynamic range.

1. Introduction

Microscopy is the standard inspection method for surface quality evaluation. One of the disadvantages of classical microscopy is the ability to sense only light intensity. This drawback can be overcome by using digital holographic microscopy (DHM). A digital holographic microscope bestows microscope ability to precisely measure surface height. In combination with a high lateral resolution of the microscopes, it forms superior measurement device.

The fundamental topology of the holographic microscope is similar to the standard microscope. A main difference is that, holographic microscope uses a coherent light source and a reference wavefront is introduced to a detector where an interference pattern is observed [1].

A common means of phase measurement in interferometry is the phase shifting. In this method a phase difference between an object wavefront and the reference wavefront is controlled and the interference patterns are captured for multiple different phase difference. For this purpose, the acousto-optics modulators (AOM) were used in our experimental setup [2-4].

Inspection of a discontinuous surface with significant steps is problematic when a simple interferometry is used. In order to allow measurement of discontinuous on the surface, two-wavelength interferometry is used.

The phase shifting is the reliable method when all parts of the measured surface reflect similar amount of light. When the surface contains parts where significantly less light is reflected, it reduces a modulation amplitude. Which negatively impact a signal to noise ratio. In order to compensate this disadvantage, a high dynamic range (HDR) approach was proposed and tested [5, 6].

The main point of this work is to use an experimental digital holographic microscope and test the mentioned improvement methods in the practical measurement of samples related to industrial production. As a sample for testing was used the piece of printed circuit board (PCB) as it has challenging properties for this type of measurement.

2. Experimental Device

In order to have experimental device to develop and test improvements method, the holographic microscope was built. The device in Fig. 1 uses an epi-illumination [7] via a microscope objective so it is intended to be used to inspect opaque samples.
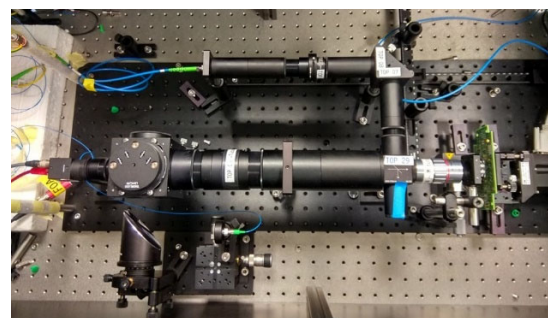

Fig. 1. The experimental holographic microscope.

The device is equipped with the microscope objective Mitutoyo MY5X-802 (5×) and a linear actuator to position sample to a focus. The object-illumination wavefront is introduced through a side tube and it is focused to a focal point of the microscope objective. Thus the object-illumination beam passing via objective form collimated

illumination. The reference beam is collimated using a fibre collimator and reflected to a camera detector via a beam splitter. Light is brought to the device via polarization maintaining optical fibres. The supplied light has linear polarization. In order to reduce internal reflections inside the system, a quarter-wave plate was added between the microscope objective and the sample. This quarter-wave plate converts the linearly polarized illumination light to a circularly polarized light. A light reflected from sample is converted back to linear polarization but it is rotated by 90 ° relatively to the light introduced to the system. A polarizer filter is placed in front of the camera to select specifically the polarization of the light reflected from sample. The device principle is illustrated in Fig. 2.
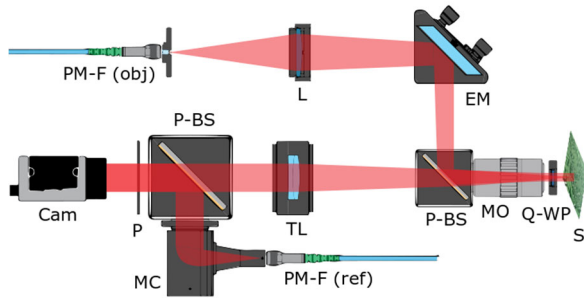
Fig. 2. The experimental microscope scheme. PM-F – PM Fibre, L – Lens, EM – Elliptic Mirror, P-BS – Pellicle Beam Splitter, MO – Microscope Objective, Q-WP – Quarter Wave Plate, S – Sample, TL – Tube Lens, MC – Mirror Collimator, P – Polarizer, Cam – Camera.

A grating stabilized tunable single-mode diode laser Toptica DL pro 633 with wavelength range from 631 nm to 635 nm was used as the coherent light source.

Each arm of the interferometer passes through one acousto-optic modulator MT80-B16-R40-Fio-PM which allows controlling output wavelength. Photo of the used AOM is in Fig. 3.

Fig. 3. One of the used AOM MT80-B16-R40-Fio-PM.

3. Phase Shifting

A standard holographic measurement approach uses the phase shifting to solve the problem of the unknown light intensity offset and gain. A few methods can be used to introduce the phase shifting to the system. The developed experimental microscope setup uses the set of the two fibre acousto-optic modulators so called Bragg cells in the reference and the illumination-object arm. These modulators are driven by an alternating electrical signal. Frequency of the output light frequency shift is equal to the electrical signal frequency. The acousto-optic modulators work at frequency tens of MHz. The difference of the frequencies can be arbitrary small, for example ones of Hz.

As result of the frequency difference, the time dependent phase shifting is introduced between the object and the reference wavefront.

$$\widehat{E}_{ref}(t) = A \cdot |\hat{E}_{in}| \cdot e^{i \cdot t \cdot (\omega_0 + \omega_{ref})}, \tag{1}$$

$$\widehat{E}_{obj}(t) = A \cdot |\hat{E}_{in}| \cdot e^{i \cdot t \cdot (\omega_0 + \omega_{obj})} \tag{2}$$

In the equations (1) and (2) there are the prescriptions of the output wave of the acousto-optics modulators in the reference and in the object arm. The value A is amplification of the modulator and the value $|E_{in}|$ is amplitude of the input wave. The functions are complex and are dependent on the time t. The value ω_0 represents the angular frequency of the input light and the values ω_{ref} and ω_{obj} represent the angular frequencies of the control signal driving each modulator.

$$\delta(t) = t \cdot (\omega_0 + \omega_{ref}) - t \cdot (\omega_0 + \omega_{obj}), \tag{3}$$

$$\delta(t) = t \cdot (\omega_{obj} - \omega_{ref}) \tag{4}$$

A phase difference $\delta(t)$ in the expression (3) is then function of the time t. It can be simplified to the function (4).

During the measurement, sequence of 4 frames is taken. Since the time of each frame is known, the introduced phase shift can be calculated from the function (4). For each pixel in the images four irradiance values I_1, I_2, I_3 and I_4 are known then. Considering the phase step between each shot is $\frac{\pi}{2}$, the formula (5) can be used to calculate the detected phase $\Delta\phi$ in each pixel. [3]

$$\Delta\phi = \arctan\left(\frac{I_4 - I_2}{I_1 - I_3}\right) \tag{5}$$

The values of the $\Delta\phi$ forms a phase map. The result phase map is wrapped and it has to be unwrapped.

4. Two-wavelength Interferometry

A Certain surface structures are difficult to measure due to the problem of phase 2π ambiguity. Typical examples of the problematic surfaces are surfaces with great slopes, discontinuities and steps. As the result of the ambiguity, the step size is limited by a used wavelength.

Two-wavelength interferometry is based on measuring data at two known wavelengths. When two-wavelength interferometry is used, measureable

step height is no longer limited by the wavelength of the used light but it is limited by a synthetic wavelength which can be calculated with the function (6) from the two values of the wavelength λ_1 and λ_2.

$$\lambda_s(\lambda_1, \lambda_2) = \frac{\lambda_2 \cdot \lambda_1}{|\lambda_2 - \lambda_1|} \qquad (6)$$

An input of the evaluation algorithm is the product of the phase shifting evaluation (5) without unwrapping. The measured phase $\Delta\phi_i(x, y)$ form a phase map for a wavelength with an index i. Each phase map can be converted to the complex domain using the expression (7).

$$\widehat{U}_i(x, y) = e^{i \cdot \Delta\phi_i} \qquad (7)$$

To combine phase of the two-wavelength expression (8) is used. [4]

$$\widehat{U}_{ab}(x, y) = \widehat{U}_a(x, y) \cdot \left(\widehat{U}_b(x, y)\right)^* \qquad (8)$$

An argument of the result complex number is the phase $\Delta\phi_{ab}$ of the synthetic wavelength.

$$\Delta\phi_{ab}(x, y) = \arg\left(\widehat{U}_{ab}(x, y)\right) \qquad (9)$$

An optical path difference (OPD) Δl_{ab} is calculated using the expression (10).

$$\Delta l_{ab} = \frac{\Delta\phi_{ab}}{2 \cdot \pi} \cdot \lambda_s(\lambda_a, \lambda_b) \qquad (10)$$

The OPD has to be divided by 2 to obtain measured surface height as the object wave has to travel the distance twice.

5. High Dynamic Range

Complex surfaces with different properties can provide very different reflectance in different areas. Visibility (12) of the interferometry fringes is given by the irradiance of the reflected-object light and by the irradiance of the reference light. It can be derived from an interference function (11). A function I_{obj} is the irradiance of the light from the object arm. A function I_{ref} is the irradiance from the reference arm. A function I is the overall irradiance of the interference. An angle ϕ is the phase difference between the object and the reference wave. A vector $\vec{r}$ is represent coordinates in the space.

$$I(\vec{r}) = I_{obj}(\vec{r}) + I_{ref}(\vec{r}) + \sqrt{I_{obj}(\vec{r}) \cdot I_{ref}(\vec{r})} \cdot \cos(\phi), \qquad (11)$$

$$v = \frac{2 \cdot \sqrt{I_{obj} \cdot I_{ref}}}{I_{obj} + I_{ref}} \qquad (12)$$

The highest visibility of the fringes is achieved when the irradiance of the reference and the object light reflected from the surface are equal, which can be deduced from the expression (13).

$$\frac{\partial v}{\partial I_{ref}} = \frac{I_{obj} \cdot (I_{obj} - I_{ref})}{\sqrt{I_{obj} \cdot I_{ref}} \cdot (I_{obj} + I_{ref})^2} = 0, \qquad (13)$$

$$I_{obj} = I_{ref} \qquad (14)$$

A visibility problem is demonstrated in Fig. 4 using simulation based on the function (12). Two different surfaces are assumed. One surface reflects ten times more light than the other.
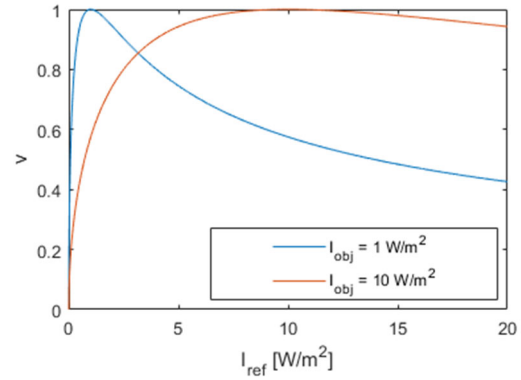

Fig. 4. Interference visibility for two different object arm irradiance as function of reference irradiance.

It is obvious that optimal visibility cannot be achieved with only one intensity of the reference light. To compensate this problem, two or more measurements are performed for two or more different reference intensities with different camera settings. The intensity of the reference light is controlled using an electronically controlled attenuator V450PA in the reference arm.

During the data processing it is necessary to merge the data of the all measurement together. For this purpose, visibility values were calculated from the phase shifting amplitudes. Synthetic phase in each pixel is selected from the map in which the pixel has the highest visibility value.

A condition for the successful composition of the phase maps, is that the phase δ on the beginning of each phase shifting sequence has to be the same. Or when it is not possible ensure same initial condition the phase difference has to be compensated during calculations. For this reason, the phase of the AOM control signal was synchronized before each measurement to make the conditions same. Nevertheless during measurement, it was discovered that used attenuator in the reference arm introduce different phase shifts for different attenuation levels. This behavior was measured using a simple experiment. The phase of the attenuator was measured for the different voltages of the control signal and a calibration curve was created. The calibration curve is plotted in Fig. 5.
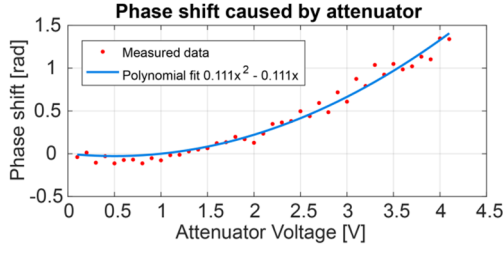
Fig. 5. The calibration curve of the attenuator V450PA.

The function (4) describing phase shift during measurement can be altered to the function (15) by subtracting the attenuator phase φ_a for used voltage.

$$\bar{\delta}(t) = t \cdot (\omega_{obj} - \omega_{ref}) - \varphi_a \qquad (15)$$

Function (5) can be altered to function (16) to compensate the introduced phase shift φ_a.

$$\Delta\bar{\phi} = \arctan\left(\frac{I_4 - I_2}{I_1 - I_3}\right) + \varphi_a \qquad (16)$$

The function $\Delta\bar{\phi}$ is then used to calculate proper phase. It is then used as input to the expression (7).

6. Measurement Procedure

The measurement procedure has multiple steps. In the first step one of the two wavelengths is tuned on the tunable laser. In the second step the camera and the attenuator are configured for the first chosen reflectivity. The frequency of the control signal of the reference AOM is set to the value 70000000 Hz. The frequency of the control signal of the object AOM is set to the value 70000001 Hz. Thus difference of the angular velocity between the reference and the object arm is 2·π rad/s.

$$\omega_{obj} - \omega_{ref} = 2 \cdot \pi \frac{rad}{s} \qquad (17)$$

The both control signals are synchronized to match phase and measurement is immediately started. Sequence of four frames with spacing 0.25 s is recorded. The camera and the attenuator are then configured for the second reflectivity. The AOM are synchronized again and the sequence of four frames is recorded. The laser is then tuned to the second wavelength and the measurement procedure is repeated for the new wavelength.

7. Experimental Data

The sample for this measurement solution was chosen the piece of the PCB. The PCB is challenging sample as it has different layers with thickness higher than the used wavelength. The layers have great slopes on the edges and the surfaces have diverse diffusivity and reflectivity. It was chosen as typical industrial

product to be analyzed. Part of the sample was painted with a thin layer of white paint to improve reflectivity.
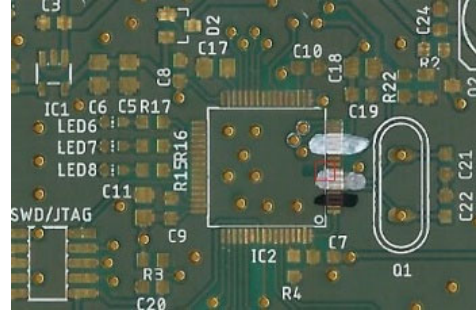
Fig. 6. The used sample with marked measured area with the red rectangle.

A presented experimental data was measured at two different wavelengths 630.45 nm and 632.28 nm. Based on the equation (6), it means that the synthetic wavelength was 218 μm. [7]

Three different settings of the attenuator and the camera were used. Captured intensity images are presented in Figs. 7, 8 and 9.
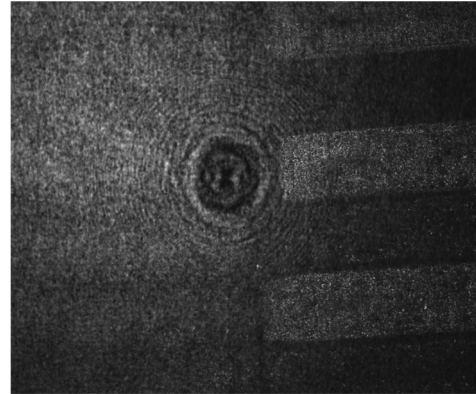
Fig. 7. An intensity image captured by the camera for the lowest attenuation in the reference arm. Control voltage was 1 V.

Fig. 8. An intensity image captured by the camera for the lowest attenuation in the reference arm. The control voltage was 3 V.

23
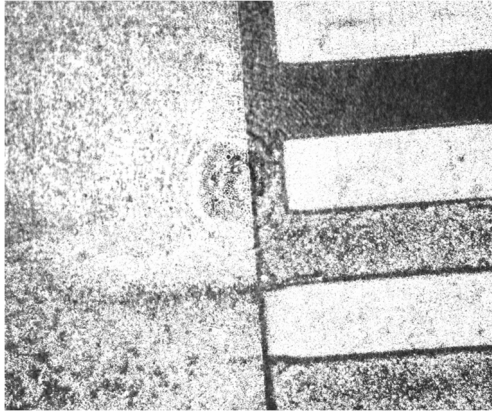
Fig. 9. An intensity image captured by the camera for the lowest attenuation in the reference arm. The control voltage was 3.5 V.

Thanks to the dynamic range enhancing technique, it was possible to measure most of the visible area. In Fig. 10, pixels are marked by color to illustrate from which intensity setting was the phase values taken.

Fig. 10. Color map of contribution in the composed data. Red areas are for the lowest reference arm attenuation, green areas are for medium attenuation and blue areas are for the highest attenuation.

Phase data converted to height map is displayed in Fig. 11.

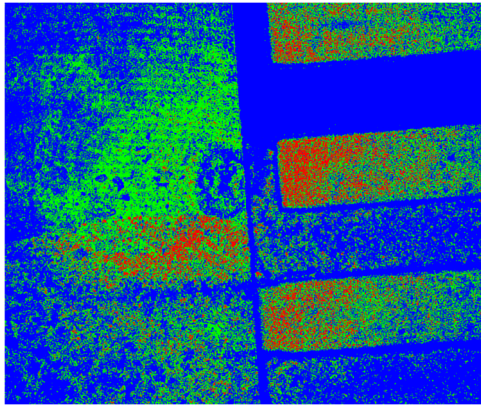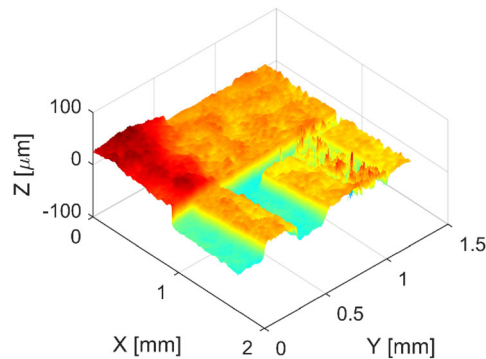**Fig. 11.** The measured height map of the chosen area on the PCB.

It can be observed that areas where the surface is not covered with any layer or the paint are very noisy.

This phenomenon is probably caused by the properties of the base material of the PCB. The base material is semi-transparent and semi-absorbent which could be a problem for the phase evaluation. Apart of these problematic areas, the solution provides fine lateral resolution (around 0.7 µm) and vertical precision. Thickness of each layer can be measured with this solution.
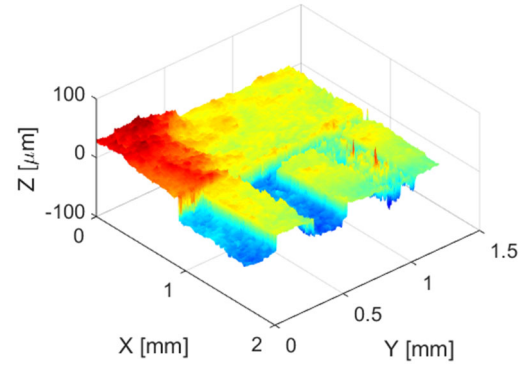
Fig. 12. The measured height map evaluated without the HDR from the measurement with the lowest attenuation.

Fig. 12 shows the evaluated height map calculated from only one attenuation settings. The result is noisier in the areas where the surface is less reflective.
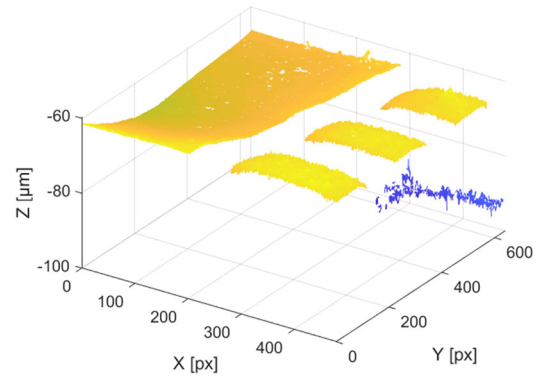
Fig. 13. Measured height map of the chosen area on the PCB with a Zygo white light interferometer.

For comparison reasons, the chosen area on the PCB was measured with Zygo NewView™ 7200. Data are presented in Fig. 13. It is noticeable that the surface measured by Zygo device has more missing or invalid areas than the surface measured by the developed experimental device.

8. Conclusions

The assembled experimental device and the performed experiment helped to verify the theoretical principles of DHM. The measurement procedure enhancement to increase dynamic range was devised and tested. The innovative way of inducing the phase shift using the AOM was tested. The measured data

24

confirmed that the AOM are very stable and it can be used as precise metrological-grade way of the phase shifting.

It was discovered that the used attenuator has the variable phase delay as the function of the control voltage. This behavior is problematic when the phase data from multiple different measurements need to be composed. The solution based on the calibration and computational compensation was proposed and used.

The measured data was used to test and develop the data evaluation algorithms. Especially algorithms for the two-wavelength interferometry, the phase evaluation and the HDR were developed.

Although this solution was unable to measure some parts of the PCB sample, it could be feasible to inspect the sample when the thin layer of paint is applied. With this treatment the measurement method can be used for the PCB inspection when a production technology needs to be optimized.

The device measurement capabilities were compared with the commercial device Zygo NewView™ 7200. The developed device was significantly better for the selected task.

Acknowledgements

References

[1]. M. K. Kim, Principles and techniques of digital holographic microscopy, *SPIE Reviews*, Vol. 1, Issue 1, 2010, 018005.

[2]. I. Kong, S. Kim, General algorithm of phase-shifting interferometry by iterative least-squares fitting, *Optical Engineering*, Vol. 34, Issue 1, 1995.

[3]. T. Kreis, Handbook of Holographic Interferometry, *Wiley-VCH*, 2005.

[4]. V. Lédl, P. Psota, P. Vojtíšek, R. Doleček, P. Mokrý, Holographic contouring and its limitations in nearly specularly reflecting surface measurement, *Proceeding of SPIE*, Vol. 9442, 2015, 94420Q.

[5]. M. F. Fay, X. C. de Lega, P. de Groot, Measuring high-slope and super-smooth optics with high-dynamic-range coherence scanning interferometry, in *Proceedings of the Classical Optics Conference*, Optical Society of America, 2014, p. OW1B.3.

[6]. J. Vargas, R. Restrepo, J. A. Quiroga, T. Belenguer, High dynamic range imaging method for interferometry, *Optics Communications*, Vol. 284, 2011, pp. 4141-4145.

[7]. ZEISS Microscopy Online Campus, Microscopy Basics, Illumination and the Optical Train, http://zeiss-campus.magnet.fsu.edu/articles/basics/opticaltrain.html

[8]. T. Kreis, Handbook of Holographic Interferometry: Optical and Digital Methods, *Wiley-VCH*, 2006.

(040)

Fresnel-Kirchoff Integral Method Comparison with Scattering Theory for the Study of Volume Dielectric Bodies

I. Taleb [1], <u>C. Neipp</u> [1], F. J. Martínez [1], M. L. Álvarez [1], E. Calzado [1], A. Márquez [1], J. Francés [1], S. Gallego [1] and A. Beléndez [1]

[1] University of Alicante, Carretera Sant Vicent s/n., 03690 Alicante, Spain
Tel.: + 3496 590 3400, fax: + 3496 590 3464
E-mail: cristian@ua.es

Summary: In this work the accuracy of Fresnel-Kirchoff integral method for the calculation of the refractive index of volume dielectric objects will be studied. To do this the results obtained by using this technique will be compared to those obtained by rigorously solving Helmholtz equation for a dielectric cylinder of circular cross section. Finally the Fresnel-Krichoff integral method will be applied to obtain the refractive index of a hair by fitting the experimental results of the diffraction pattern of the hair measured on a CCD camera to the theoretical curve.

Keywords: Scattering, Fresnel diffraction, Interferometry.

1. Introduction

Fresnel diffraction has been usually used as a technique for measuring the optical properties of different dielectric structures [1]. It is well known that Fresnel theory of diffraction was intended to simulate planar structures. Nonetheless, it has been also applied to simulate volumetric dielectric structures [2, 3]. To do this the structure must be treated as a two dimensional object. This is achieved by taking into account the phase accumulated by an incident plane wave after passing through the object. The amplitude of the input field in the Fresnel-Kirchoff integral is assumed to have this phase, and the calculation of the integral provides the field in the output plane. In this work, the accuracy of this method will be analyzed by comparing the results provided by Fresnel-Kirchoff approximation for a dielectric cylinder of circular cross section to the results obtained by rigorously solving Helmholtz equation.

Then, the method will be applied to obtain the refractive index of a hair. To do this the normalized intensity distribution of the diffraction pattern of the hair will be measured by using a CCD camera. Then, the experimental results will be fitted to the theoretical curve obtained by the Fresnel-Kirchoff method.

2. Theoretical Models

2.1. Fresnel Integral

We will start by considering that an object placed in an input plane is illuminated by a monochromatic wave. The field $U(P)$ at a point P (x,y) can be obtained from the field evaluated at the input plane $U(x',y')$ (described with coordinates x', y'), by applying Fresnel approximation to Fresnel-Kirchoff integral [1]:

$$U(P) = \frac{e^{ikz}}{i\lambda z} \iint_{-\infty}^{\infty} U(x',y') exp\left\{i\frac{k}{2z}[(x-x')^2 + (y-y')^2]\right\} dx'dy', \tag{1}$$

where λ is the wavelength of incident light, k is the wavenumber and z is the perpendicular distance between the input plane and the observation point P.

We will assume in this work that the integral (1) can be separated into the product of two one-dimensional integrals:

$$U(x,y) = \frac{e^{ikz}}{i} I_x(x) I_y(y) \tag{2}$$

It is important to notice that this assumption has not general validity, but it is applicable in the case we are going to consider, namely a unit amplitude incident wave onto a rectangular aperture and an optical fiber. In fact is applicable whenever $U(x',y')$ can be separated into the product of two one-dimensional amplitudes, where

$$I_x(x) = \frac{1}{\sqrt{\lambda z}} \int_{-\infty}^{\infty} U(x') exp\left[i\frac{k}{2z}(x-x')^2\right] dx', \tag{3}$$

$$I_y(y) = \frac{1}{\sqrt{\lambda z}} \int_{-\infty}^{\infty} U(y') exp\left[i\frac{k}{2z}(y-y')^2\right] dy' \tag{4}$$

The intensity of the field at point P(x,y) is computed by I(x,y) = $|U(x,y)|^2$.

Due to the independence of the last two integrals with respect to the other variable, one can concentrate in observing the diffraction pattern by varying either x or y coordinate. In our case, by absorbing the contribution of the y dependence in a constant K, the

wave field amplitude at point P can be finally expressed as:

$$U(x) = Ke^{ikz}I_x(x) \qquad (5)$$

In the particular case of diffraction of a dielectric circular cylinder we will assume that the phases accumulated by light from a plane just in front of the cylinder and another just before the fiber are (Fig. 1) [3]:

$$\varphi_S = 2kan_S, |x'| > a, \qquad (6)$$

$$\varphi_C = 2k(n_C - n_S)\sqrt{a^2 - x'^2}, \qquad (7)$$

where n_s is the index of refraction of the cylinder environment, n_C the refractive index of the cylinder and a is the radius of a circle representing the cross section of the cylinder. φ_S takes into account the phase accumulated by the surroundings, φ_C is the phase accumulated by the cylinder. Now assuming that a unit amplitude wave is incident onto the cylinder, $U(x')$ can be evaluated as $U(x') = \exp(ik\varphi)$, where φ takes into account at each point x' the different contributions of φ_S, and φ_C. The expression of the amplitude of the wavefield at a point $P(x,y)$ of the output plane (CCD) (Fig. 2) is finally:

$$
\begin{aligned}
&U(P) = \\
&= \frac{K'\exp(i\varphi_S)}{B}\left\{ \begin{array}{l} 1 + C(\alpha) - C(\beta) + i[1 + S(\alpha) - S(\beta)] + \\ +B\int_{-a}^{a}\exp(i\varphi_C(x'))\exp\left[ik\frac{(x-x')^2}{2z'}\right]dx' \end{array}\right\},
\end{aligned}
\qquad (8)
$$

where:

$$K' = Kexp(iz')/\sqrt{\lambda z'}, \qquad (9)$$

$$B = \sqrt{2}/\sqrt{\lambda z'}, \qquad (10)$$

$$\alpha = B(x - a), \qquad (11)$$

$$\beta = B(x + a), \qquad (12)$$

and $C(\alpha)$ y $S(\alpha)$ are the Fresnel integrals. λ is the wavelength in vacuum and z' is the distance of the cylinder to the output plane.
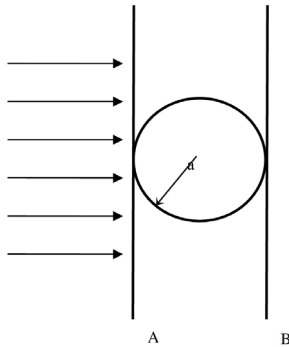
Fig. 1. Cross section of a dielectric circular cylinder. Planes A and B determine the accumulated phase.
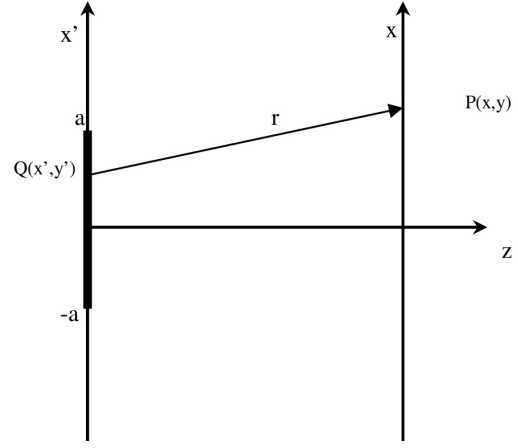
Fig. 2. Input and output planes for the diffraction of light by a circular cylinder.

The intensity as a function of x can then be calculated as: $I(x) = |U(x)|^2$.

2.1. Rigurous Solution

The scalar wave equation can be written in cylindrical coordinates (ρ, φ, z) as:

$$\frac{1}{\rho}\frac{\partial}{\partial\rho}\left(\rho\frac{\partial\psi}{\partial\rho}\right) + \frac{1}{\rho^2}\frac{\partial^2\psi}{\partial\varphi^2} + \frac{\partial^2\psi}{\partial z^2} + k^2\psi = 0 \qquad (13)$$

Separable solutions can be found in the form:

$$\psi_v(\rho, \varphi, z) = Z_v(k\rho)e^{iv\varphi}e^{ihz}, \qquad (14)$$

$v = 0, 1, 2$; and h is dictated by the form of the incident wave. For an electric field which is incident parallel to the axis of the cylinder (in the z direction) we can consider that $h = 0$, and $Z_v(k\rho)$ satisfy Bessel equation [4]:

$$
\begin{aligned}
&\rho^2\frac{d^2}{d\rho^2}Z_v(k\rho) + \rho\frac{d}{d\rho}Z_v(k\rho) + \\
&+ (k^2\rho^2 - v^2)Z_v(k\rho) = 0
\end{aligned}
\qquad (15)
$$

The vector cylindrical harmonics can be generated as:

$$\vec{M}_v = \vec{\nabla} \times (\vec{e}_\rho\psi_v), \qquad (16)$$

and

$$\vec{N}_v = \frac{\vec{\nabla} \times \vec{M}_v}{k} \qquad (17)$$

Here we have chosen the probe vector to be $\vec{e}_\rho$. Applying equations (16), (17) one can obtain:

$$\vec{M}_v = \frac{-iv}{\rho}Z_v(k\rho)e^{iv\varphi}\vec{e}_z, \qquad (18)$$

27

$$\vec{N}_v = \frac{e^{iv\varphi}}{k\rho} \left[\begin{array}{c} \frac{v^2}{\rho} Z_v(k\rho)\vec{e}_\rho + \\ +iv\left(-\frac{Z_v(k\rho)}{r} + kZ'_v(k\rho)\right)\vec{e}_\varphi \end{array} \right], \quad (19)$$

where $Z'_v(k\rho) = \frac{dZ_v(k\rho)}{d(k\rho)}$, that is the prime denotes the absolute derivative of Z with respect its argument.

Now the electric field can be expanded in terms of the cylindrical harmonics. We will consider there expansions for the electric field incident, scattered and inside the cylinder. The proper Bessel functions $Z_v(k\rho)$ will be chosen accordingly for each case. In particular, since the electric field must be finite at the origin the Bessel functions of the first kind ($J_v(k\rho)$) will be chosen in the cases of the incident and the internal field. In the case of the scattered field, Hankel functions ($H_v(k\rho)$) will be chosen as the generating functions, since their assymptotic behavior is that of a decaying wave at large distances.

The expansion of the incident field is:

$$\vec{E}_i = \sum_{v=-\infty}^{\infty} A_v^{(i)}\vec{M}_v^{(i)} + B_v^{(i)}\vec{N}_v^{(i)} \quad (20)$$

The expansion of the internal field is:

$$\vec{E}_1 = \sum_{v=-\infty}^{\infty} A_v^{(1)}\vec{M}_v^{(1)} + B_v^{(1)}\vec{N}_v^{(1)} \quad (21)$$

The expansion of the scattered field is:

$$\vec{E}_s = \sum_{v=-\infty}^{\infty} A_v^{(s)}\vec{M}_v^{(s)} + B_v^{(s)}\vec{N}_v^{(s)} \quad (22)$$

In each case if the electric field is expanded as

$$\vec{E} = \sum_{v=-\infty}^{\infty} A_v\vec{M}_v + B_v\vec{N}_v \quad (23)$$

The corresponding magnetic field is:

$$\vec{E} = \frac{-ik_j}{\omega\mu}\sum_{v=-\infty}^{\infty} A_v\vec{N}_v + B_v\vec{M}_v, \quad (24)$$

where $k_j = k$ for the incident and scattered electric field

And $k_j = nk$, being n the refractive index of the cylinder.

$$\vec{E}_j = \sum_{v=-\infty}^{\infty} A_v^{(j)}\vec{M}_v^{(j)} + B_v^{(j)}\vec{N}_v^{(j)}, \quad (25)$$

where j = i, 1,s for the incident, internal and scattered field respectively.

Now, Imposing the appropriate boundary conditions at the surface of the cylinder the values of

$A_v^{(j)}$ and $B_v^{(j)}$ can be obtained, so that the total field outside the cylinder can be calculated.

2.2. Scalar Wave Approximation

Assuming the scalar approximation, the incident electric field can be expressed as:

$$E_i = E_0 e^{-ik\rho cos\varphi}, \quad (26)$$

Taking into account the expansion of the exponential in terms of Bessel functions the incident electric field can now be expressed as:

$$E_i = \sum_{v=-\infty}^{\infty} E_0(-i)^v J_v(kr)e^{iv\varphi} \quad (27)$$

The scattered field can be expressed as:

$$E_s = \sum_{v=-\infty}^{\infty} \alpha_v H_v(kr)e^{iv\varphi}, \quad (28)$$

And the internal field:

$$E_1 = \sum_{v=-\infty}^{\infty} \beta_v H_v(nkr)e^{iv\varphi} \quad (29)$$

Imposing the appropriate boundary conditions the following result for the expansion coefficients can be obtained:

$$\alpha_v = E_0(-i)^v \frac{J'_v(x)J_v(nx) - nJ_v(x)J'_v(nx)}{nH_v(x)J'_v(nx) - J_v(nx)H'_v(x)} \quad (30)$$

It is important to say that in this particular case the scalar wave approximation gives the same result as the rigorous solution.

3. Results and Discussion

In Fig. 3 the results obtained by using both methods are represented for a circular cylinder of refractive index 1.50, radius of 30 mm and separated from the output plane 5 mm. As it can be seen from the figure both methods have good agreement.

In Fig. 4 it is shown the experimental set up used to obtain the diffraction pattern of a hair. The light coming from an He-Ne laser (633 nm) is collimated by using a system of lenses; the sample (hair) is placed between the laser and a CCD connected to a personal computer is used to process the data. Fig. 5 shows the diffraction pattern obtained from the hair by using this set up.
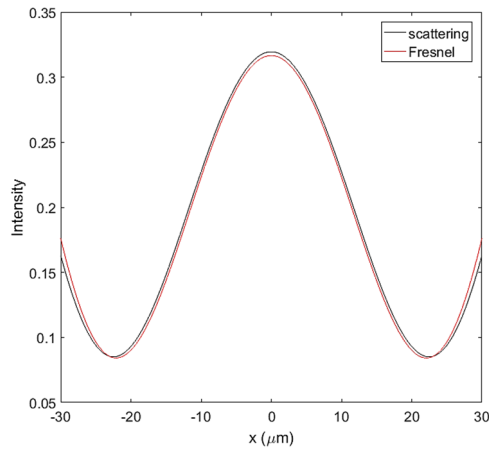
Fig. 3. Comparison of Fresnel-Kirchoff integral diffraction method and rigorous method for a cylinder of refractive index of 1.50 and radius of 30 μm.
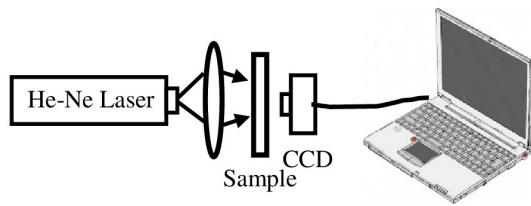
Fig. 4. Experimental set up used to record the diffraction pattern.

In Fig. 6 the diffraction pattern of a hair is represented. The fitting of the theoretical curve to the experimental data provides a refractive index of 1.55 and an internal radius of 21.35.
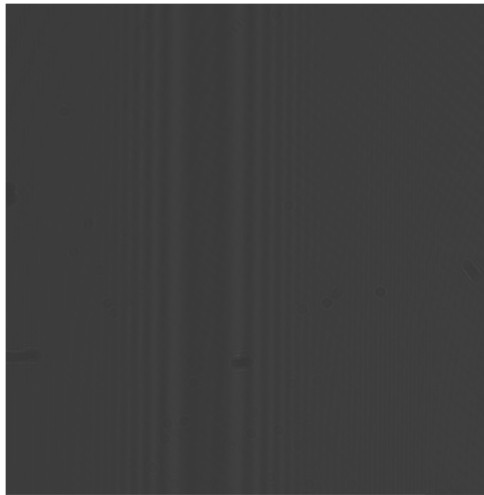
Fig. 5. Diffraction pattern on the CCD of a hair.
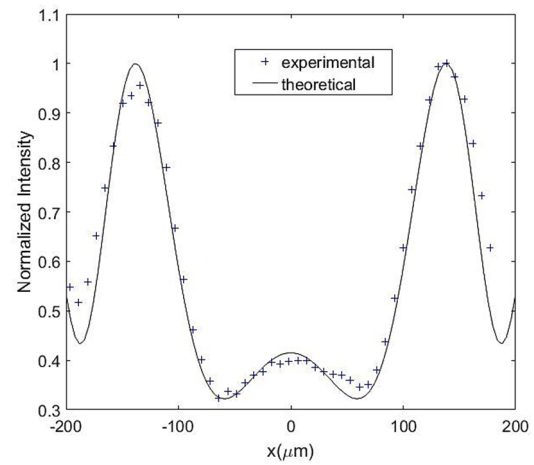
Fig. 6. Experimental data and theoretical fit of the intensity recorded on a CCD camera from the diffraction of a hair with refractive index of 1.55 and radius 21.35 μm.

4. Conclusions

In this work the Fresnel-Kirchoff integral approximation is compared to the rigorous solution of Helmholtz equation for the particular case of a circular cylinder. The results demonstrate that there is good agreement between both methods. The Fresnel-Kirchoff integral method is used to fit the experimental data of the diffraction pattern created by a hair.

Acknowledgements

References

[1]. J. W. Goodman, Introduction to Fourier Optics, *McGraw-Hill*, New York, 1996.
[2]. M. G. Beygi, R. Karimzadeh, M. Dashtdar, Nonlinear refractive index measurement by Fresnel diffraction from phase object, *Optics & Laser Technology*, Vol. 66, 2015, pp. 151-155.
[3]. A. Sabatyan, M. T. Tavassoly, Application of Fresnel diffraction to non-destructive measurement of the refractive index of optical fibers, *Optical Engineering*, 2007, Vol. 46 (12), 128001.
[4]. G. Arfken, H. Weber, F. E. Harris, Mathematical Methods for Physicists, *Academic Press*, 2012.

(046)

New Ultrashort OPCPA Petawatt Class Beamline for Vulcan Laser Facility

N. Baktash [1], M. Galimberti [1], P. Oliveira[1], I. Musgrave [1] and C. Hernandez-Gomez [1]
[1] Central Laser Facility, Science and Technology Facilities Council, Chilton, Didcot, Oxon. OX11 0QX, UK
Tel.: + 44 1235 445734, fax: + 44 1235 445888
E-mail: neda.baktash@stfc.ac.uk

Summary: We report on a new beamline for Vulcan Petawatt laser facility, this will deliver high quality support for the laser plasma community in a unique laser facility configuration. The beamline will deliver 30 J pulse energy in less than 30 fs pulse width to target with a repetition rate of 1 shot every 5 minutes. We will be able to fire this laser in conjunction with the already available PW laser (500 J and 500 fs) on target at the same time. This beamline will be based solely on OPCPA using LBO as the non-linear crystal.

Keywords: Ultrafast laser, CPA, Ultra-broadband OPA, High power laser, LBO nonlinear crystal, Betatron x-ray laser.

1. Introduction

The Vulcan laser facility is being upgraded with a new beam line that is based fully on Optical Parametric Chirped Pulse Amplification (OPCPA). The Vulcan Petawatt laser has been operated for more than 10 years with a sub 1 ps beam and 500 J of energy. This has allowed high quality support for the scientific community and served as an adaptable facility for plasma physics experiments [1].

In order to perform strong field physics experiments such as laboratory astrophysics [2], high energy density physics [3], schemes for particle acceleration [4], high-energy ultra-short pulses are strongly required. Most of these experiments require PW peak power laser pulses.

We present an upgrade of the referred Vulcan Petawatt laser by adding a new beamline of PW class with a reduced pule duration by less than 30 fs (30 J) over a broadband spectral bandwidth (>100 nm). This is similar with what is achievable with Ti:sapphire systems.

The generation of such pulses can be performed through the OPCPA [5, 6] technique. The main advantages of the OPCPA technique, respect to the Chirped Pulse Amplification (CPA), are the high single pass gain, lower thermal effects and the ability to support broader amplified spectrum [7]. Those are crucial parameters to generate intense pulses in the PW regime at high repetition rate, namely shot/minute.

The short PW beamline together with a long focal length parabola will allow 2 GeV electron beams and the correspondent betatron x-ray source. This increases the imaging capabilities and pump probe experiments for high energy plasmas and will be the main purpose of the new beamline.

2. Experimental Setup

An overview of the final beamline layout is shown in Fig. 1.
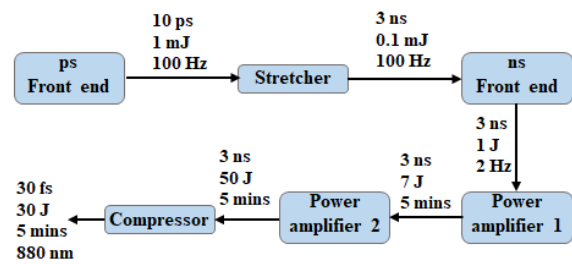
Fig. 1. Beamline layout.

A new broadband mJ-level picosecond OPCPA has been built. It includes a broadband oscillator that is amplified by two ps lasers (1 and 25 mJ respectively) [8].

This is stretched to 3 ns and two OPCPA stages will amplify it using a 10 J Nd:YAG laser system as a pump. A Nd:Glass amplification chain with 30 J is then used to pump a first power amplifier. A last amplification stage is pumped by one of the Nd:Glass disks amplifiers.

All the amplification stages are based in LBO because it is the highest nonlinearity crystal that allows us to have apertures of up to 200×200 mm^2.

The infrastructure of the facility including the highlight of the new broadband mJ-level picosecond OPCPA source, and the focusing chamber is presented in Fig. 2.
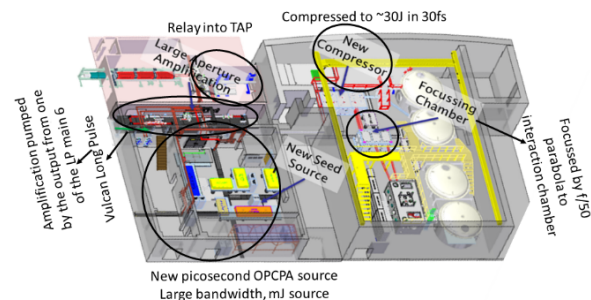
Fig. 2. Facility layout including the OPCPA beamline, compressor and focusing chamber.

3. Project Plan

The overall project is splitted in 3 phases, two of these are illustrated in the Table 1.

In the first phase, the last amplifier will use a 108 mm disk amplifier and an amplification stage will increase the energy up to 30 J, with a limited repetition rate of 1 shot every 20 min. This is limited by the pump repetition rate.

In a second phase a new design of forced air cooled disk amplifier, will allow the pump to increase the repetition rate to 1 shot every 5 min, which at the end will provide the beamline with 1 shot in each 5 mins.

Table 1. Laser specification of two phases of Vulcan beamline project.

	Phase I	**Phase II**
Pulse Length	< 30 fs	
Spectral range	800 nm – 960 nm	
Final Beam Size	200 mm	
Final Beam Shape	Round	Square
Energy on Target	~30 J	~40 J
Rep. Rate	20 min	5 min

In phase 3, in addition to the new beamline, the long pulse capability for the Petawatt target is planned to the improved, increasing the available energy to the kJ scale.

4. Conclusions

This new laser beamline will mainly be used for betatron radiation probing of the plasma. Apart from betatron radiation this beamline can also allow for a new set of experiments for study QED effect using two high intensity PW beamlines.

References

[1]. C. N. Danson, P. A. Brummitt, R. J. Clarke, et al., Vulcan Petawatt – An ultra-high-intensity interaction facility, *Nuclear Fusion*, Vol. 44, Issue 12, 2004, pp. S239-S246.

[2]. B. A. Remington, D. Arnett, R. P. Drake, H. Takabe, Modelling astrophysical phenomena in the laboratory with intense lasers, *Science,* Vol. 284, Issue 5419, 1999, pp. 1488-1493.

[3]. M. Roth, T. E. Cowan, M. H. Key, S. P. Hatchett, et al., Fast ignition by intense laser-accelerated proton beams, *Phys. Rev. Lett.,* Vol. 86, Issue 3, 15 January 2001, pp. 436-439.

[4]. T. Bartal, M. E. Foord, C. Bellei, M. H. Key, et al., Focusing of short-pulse high-intensity laser-accelerated proton beams, *Nature Physics*, Vol. 8, Issue 2, 2011, pp. 139-142.

[5]. A. Dubietis, G. Jonušauskas, A. Piskarskas, Powerful femtosecond pulse generation by chirped and stretched pulse parametric amplification in BBO crystal, *Optics Communications,* Vol. 88, 1992, pp. 437-440.

[6]. I. N. Ross, P. Matousek, M. Towrie, A. J. Langley, J. L. Collier, The prospects for ultrashort pulse duration and ultrahigh intensity using optical parametric chirped pulse amplifiers, *Optics Communications*, Vol. 144, 1997, pp. 125-133.

[7]. A. Dubietis, R. Butkus, A. P. Piskarskas, Trends in chirped pulse optical parametric amplification, *IEEE Journal of Selected Topics in Quantum Electronics,* Vol. 12, Issue 2, 2006, pp. 163-172.

[8]. M. Galletti, High contrast front-end for a petawatt laser system designed for electron acceleration and high intensity laser-matter applications towards advanced compact particle accelerators, PhD Thesis, *Instituto Superior Tecnico*, Lisboa, 2020.

(047)

Optical Phase Readout Instrument for Picometer-level Precision Heterodyne Interferometers

J.J. Esteban Delgado [1], M. Dovale Alvarez [1], T. Schwarze [1], C. Vorndamme [1], I. Bykov [1],
P. Martínez Cano [1], G. Fernández Barranco [1], K. Yamamoto [1], A. Pizzella [1,] Fahri Öztürk [1,]
D. Penkert [1], Jens Reiche [1] and G. Heinzel [1]

[1] Max Planck Institute for Gravitational Physics (Albert Einstein Institute), and Leibniz Universität Hannover,
Institut für Gravitationsphysik, Callinstrasse 38, 30167 Hannover, Germany
Tel.: +49- (0) 511-762-17882
E-mail: juan.jose.esteban@aei.mpg.de

Summary: Optical heterodyne detection is a well-stablished technology for monitoring relative pathlength fluctuations of a laser link through phase measurements of the interfering signals. A laser interferometer typically combines a number of beams that travel different optical paths to determine factors as lengths, surface irregularities or index of refraction in materials. Its ability to measure precisely with high dynamic range and accuracy over multiple interference fringes allows the measurement of features on the atomic scale, in fields like gravitational physics, even when the received beam is sensed at ultra-low light power [1-5].

In this contribution, it is reported the design, construction and operation of an optical phase readout instrument able to extract picometer-stable translation and nanometer-stable tilts measurements over thousands of seconds from a laser link operating at MHz heterodyne frequencies. The optical pathlength sensitivity of the instrument has been measured below 1 pm/√Hz for frequencies above 3 mHz [6, 7]. The pitch and yaw pointing sensitivity is required below 5 nrad/√Hz and performed by applying a differential wavefront sensing technique [5, 8]. The instrument sensitivity seems to be limited above 3 mHz by ADC clock timing jitter and below 1 mHz by phase distortion caused by temperature fluctuations in the front-end electronics circuitry [9]. Noise budgets and coupling mechanisms for both longitudinal and angular displacements are still under investigation with the design goal of an enhanced instrument performance with reasonable margins to the stringent noise requirements.

These ultra-stable optical sensitivities result from relative displacement measurements after interfering an optical link and a stable local oscillator with an offset frequency up to 25 MHz. Beyond such heterodyne frequency, electronic noise at the quadrant photo-receives becomes the dominant noise source contribution in the measurement chain [10]. To enable a stable heterodyne signal at the photoreceivers outputs, the instrument features a tunable offset phase locking scheme able to operate the laser link as an optical transponder. The frequency readout of the heterodyne signal is used by the controller to mutually lock both interfering beams and return the local laser

as a high power phase replica of the incoming light. It also allows to compensate for Doppler effects while ensuring operation under environments with high diffraction losses, e.g., enabling measurements over larger distances in contrast to passive retroreflectors configurations. The built-in optical transponder controllers have been designed for tracking frequency varying beat note signals in the range of up to a few kHz/s and able to operate under weak-light conditions, i.e., about 100 pW of impinging optical power levels at the quadrant photoreceivers.

The laser transponder scheme is developed to enable a stable heterodyne signal within the photoreceiver bandwidth. In order to achieve a displacement sensitivity of 1 pm/√Hz at 3 mHz for beat notes up to 25 MHz, the necessary clock timing jitter stability between Rx/Tx remote terminals would be approximately 40 fs/√Hz [11]. Without a direct mechanism for timing synchronization between instruments, the optical metrology system requires the realization of a clock noise removal scheme in order to subtract the excess phase noise that couples into the laser interferometer. To measure the relative clock noise contribution, the 10 MHz master oscillator of the instrument is multiplied by an integer factor (typically 240) and modulated as high-frequency (~ 2.4 GHz) phase modulation sidebands onto each laser link by using 10 % of its optical link power. After interference between local and incoming lasers, the phase measurement of the resulting sideband-to-sideband beat note contains the amplified clock noise information necessary to remove the clock noise in post-processing [12].

A side-effect of the laser transponder configuration enables that our metrology system features Doppler estimations between terminals by reading out the frequency registers of the interferometric signals. It enables precise measurements of both relative optical displacements and velocity between Tx/Rx terminals. Relative measurements are combined with absolute positioning estimations by applying a second phase modulation scheme onto the laser link. The applied absolute ranging concept is inherited from Global Positioning Systems (GPS) by implementing a Direct-Sequence Spread Spectrum (DSSS) modulation scheme. In contrast to other ranging methods, our

development provides a low-depth modulation index to reduce both the optical power allocated to the Pseudo-Random Noise (PRN) modulation and the residual carrier phase noise due to fast PRN transitions. Thus, our ranging scheme uses only 1 % of the available optical link power and achieves sub-meter ranging accuracy for PRN chipping rates around 1 MHz, while most of the light power is used for precise heterodyne interferometry. This PRN ranging scheme determines the light travel time over the interferometric arm, so-called pseudorange measurements, due to the fact that clock differences between terminals are coupled into the measurement and therefore computed with an accuracy at nano-second levels, i.e., at the level of the absolute ranging accuracy. Moreover, this DSSS modulation scheme enables optical communication between terminals by encoding PRN codes with data information running at lower bit rates. Experimental results have shown ranging measurements with centimeter rms noise at 3 Hz of updating rate and the viability of highly reliable data transfer at several kilobits per second under ultra-low light power (1 pW) conditions [13].

In conclusion, the optical metrology system described herein combines a continuous-wave (c.w) laser interferometry with low-depth modulation techniques to provide in a single optical instrument both picometer-level interferometry and absolute ranging measurements with optical communication capabilities. This optical metrology system allows to overcome one of the limiting factors on c.w laser interferometers, the ambiguity range. Moreover, this scheme enables precise timing of readout data, indirect clock synchronization between remote terminals, Doppler estimations and optical acceleration measurements, being a versatile and attractive technology for several optical applications apart from our main research field, i.e., gravitational physics.

Keywords: Gravitational physics, Optical metrology, Heterodyne interferometry, Laser ranging, Differential wavefront sensing, Laser pointing, Laser offset phase locking, Phase-locked loop, Delay locked loop, Pseudoranges, Optical communication, High resolution translation and tilt measurements.

References

[1]. K. Danzmann, LISA and its pathfinder, *Nature Phys.*, Vol. 11, 2015, pp. 613-615.

[2]. M. Armano, *et al.,* Sub-femto-g free fall for space-based gravitational wave observatories: LISA pathfinder results, *Phys. Rev. Lett.*, Vol. 116, Issue 23, 2016, 231101.

[3]. D. Castelvecchi, Success of gravity-wave satellite paves way for three-craft mission, *Nature News Physics*, Vol. 546, Issue 7660, 2017, pp. 583-584.

[4]. G. Wanner, Space-based gravitational wave detection and how LISA Pathfinder successfully paved the way, *Nature Physics*, Vol. 15, 2019, pp. 200-202.

[5]. K. Abich, *et al.*, In-orbit performance of the GRACE follow-on laser ranging interferometer, *Phys. Rev. Lett.*, Vol. 123, 19 July 2019, 031101.

[6]. O. Geberding, *et al.,* Readout for intersatellite laser interferometry: Measuring low frequency phase fluctuations of high-frequency signals with microradian precision, *Review of Scientific Instruments*, Vol. 86, 2015, 074501.

[7]. T. S. Schwarze, et al., Picometer-stable hexagonal optical bench to verify LISA phase extraction linearity and precision, *Phys. Rev. Lett.*, Vol. 122, 2019, 081104.

[8]. E. Morrison, *et al.,* Automatic alignment of optical interferometers, *Appl. Opt.*, Vol. 33, 1994, 5041.

[9]. O. Geberding, *et al.,* Phasemeter core for intersatellite laser heterodyne interferometry: Modelling, simulations and experiments, *Classical and Quantum Gravity*, Vol. 30, Issue 23, 2013, 235029.

[10]. G. Fernández Barranco, *et al.,* A low-power, low-noise 37-MHz photoreceiver for intersatellite laser interferometers using discrete heterojunction bipolar transistors, *IEEE Sensors Journal*, Vol. 18, Issue 18, pp. 7414-7420.

[11]. G. Heninzel, et al., Auxiliary functions of the LISA laser link: ranging, clock noise transfer and data communication, *Classical and Quantum Gravity*, Vol. 28, Issue 9, 2011, 094008.

[12]. M. Tinto. et al., Time-delay interferometry and clock-noise calibration, *Phys. Rev. D*, Vol. 98, 2018, 042003.

[13]. J. J. Esteban Delgado, et al., Experimental demonstration of weak-light laser ranging and data communication for LISA, *Optics Express*, Vol. 19, Issue 17, 2011, pp. 15937-15946.

(048)

Recent Progress on High Harmonic Generation Source at ELI Beamlines

O. Hort [1], M. Albrecht [1,2], O. Finke [1,2], M. Jurkovič [1,2], R. Lera [1], D. D. Mai [1], E. Klimešová [1], S. Espinoza [1], S. Richter [1], J. Gautier [1], S. Sebban [1], R. Antipenkov [1], F. Batysta [1], J. Novák [1], J. T. Green [1], M. Krikunova [1,3], J. Andreasson [1] and J. Nejdl [1]

[1] ELI Beamlines, Institute of Physics ASCR, Na Slovance 1999/2, 182 21 Prague, Czech Republic
[2] Faculty of Nuclear Sciences and Physical Engineering CTU, Břehová 7, Prague 1, Czech Republic
[3] Institut für Optik und Atomare Physik, Technische Universität Berlin, ER 1-1,
Strasse des 17. Juni 135, 10623, Berlin, Germany
Tel.: +420266051494
E-mail: Ondrej.Hort@eli-beams.eu

Summary: The mission of the ELI Beamlines facility is to provide various ultrafast extreme ultraviolet, X-ray and charged particles sources for user-driven basic and applied research. Here we present the latest progress and experimental results of the XUV beamline. It is based on high harmonic generation (HHG) in gases driven by multi-TW femtosecond pulses in loose focusing geometry. The focal length was recently increased to 5 meters upscaling the generated XUV photon flux and shifting the efficient generation to wavelengths between 20 and 30 nm. We report XUV energy per shot generated in argon cell and briefly describe diagnostics and user chamber capabilities.

Keywords: High harmonic generation, TW femtosecond pulses, Loose focusing, XUV.

1. Introduction

The European project ELI consists of 3 pillars. One of them – the ELI Beamlines – is devoted to fulfil the need of users from various fields for laser-driven secondary sources of extreme ultraviolet (XUV) and X-ray photons, as well as accelerated charged particles. The ELI Beamlines facility was specifically designed to offer unique pump-probe experimental schemes where the secondary sources are coupled together or combined with the driving laser beams [1, 2].

Here we present the XUV beamline based on HHG in gases. It was designed for versatility to fulfil user needs of various spectral bandwidth and high photon flux. It takes advantage of the recent development in the field of Ti:Sapphire OPCPA based laser chains providing high peak-power pulses at a repetition rate of 1 kHz, suitable for applications. As the HHG scaling laws were recently defined [3], one can obtain high XUV photon numbers using high energy driving lasers. Therefore, high XUV intensity can be obtained even with state-of-the-art HHG conversion efficiency.

2. Experimental Setup

2.1. Laser System

The L1 laser system is based on Ti:Sapphire oscillator and optical parametric chirped-pulse amplifiers (OPCPA). This concept provides both short pulse duration, high energy and high repetition rate [4]. At the end of 2020 it is expected to deliver pulses of 40 mJ energy, 15 fs duration at a repetition rate of 1 kHz. Optimal temporal characteristics of the beam are ensured by an acousto-optical modulator (Dazzler).

Installation of adaptive optics will, in near future, allow controlling the wavefront and divergence of the beam for the HHG. To provide high beam stability, active beam-pointing stabilization will be employed in early 2021. Furthermore, a set of permanent laser diagnostics close to the experiments is under implementation. As some of the characterization tools run at the laser repetition rate of 1 kHz, they will provide timestamped driving pulse & beam characteristics for every shot. Acquisition software to integrate such data with saved experimental results is under development.

2.2. High Harmonic Generation

The HHG beamline will be extended to support focusing mirror focal length up to 25 meters (f-number 900) to ensure optimal scaling of XUV generation. In such geometry, and with the fully commissioned laser system, we expect to obtain XUV radiation of up to 250 eV of photon energy (corresponding to a wavelength of 5 nm) in a beam of low divergence of < 0.5 mrad [5].

The beamline is currently equipped with 5 m focusing and is planned to extend to 14.5 m towards the end of 2020. The focusing mirror is placed at 50 cm motorized translation stage to allow changing the longitudinal position of the laser focus with respect to the target.

Currently, a gas cell is used to perform HHG. It is variable and motorized to provide the possibility to rapidly change the HHG medium length in the range 0 – 20 cm. A motorized diaphragm placed in the beam approx. 5 m upstream of the focusing mirror gives a possibility to conveniently change the beam size and interaction intensity.

For applications where a very short and high-density HHG medium is required an Even-Lavie valve will be installed to obtain very high gas pressure in the interaction zone.

The HHG beamline may as well serve experiments where very high laser intensity is needed. For that reason a new focusing chamber is under development. This vacuum vessel will allow 2.5 m focusing length.

After the HHG, the XUV beam co-propagates together with the IR beam. There are two complementary ways to separate the IR radiation from the XUV beam.

Metallic filters are used to block the IR radiation completely. They are installed in 2 independent positions enabling direct experimental measurement of their XUV transmission. As the driving laser average power reaches very high levels, three glass plates at grazing incidence are installed in front of the filters in order to reduce the IR power hitting the metallic filters. The plates are coated with Ta_2O_5 for high XUV reflection and high transmission of IR. These plates are planned to be motorized under vacuum for convenient change of the setup.

2.3. Monochromatization and Characterization of XUV Radiation

For certain applications it is advantageous to employ a narrow bandwidth XUV beam. For this purpose an XUV monochromator was installed on the HHG beamline. It is designed to accommodate up to 4 easily exchangeable gratings and a set of slits with various widths to provide quick change of spectral bandwidth and tunable resolution.

The monochromator is removable under vacuum so the broadband XUV beam can be characterized and used as well. Offline XUV pulse energy is measured via a calibrated XUV diode and an upgrade for online energy measurement is in progress.

For spectral characterization the source is first imaged in the horizontal plane on a motorized slit that is imaged by a concave grating onto a XUV CCD while in vertical plane the source is imaged directly on the camera chip. This way one obtains a high sensitivity XUV spectrometer. Recently, an upgrade was installed that allows the option not to image in the vertical plane and thus get the far field of the XUV beam resulting in a spatially resolved XUV spectra.

The beamline is also equipped with an XUV wavefront sensor. The XUV diagnostics chamber is designed in a way that permits fast switching of the XUV characterization instruments.

3. Experimental Results

The HHG beamline is currently equipped with 5 m focusing geometry to match the current status of the L1 driving laser that currently produces pulses of 20 mJ of energy, 15 fs duration at 1 kHz repetition rate spectrally centered on 825 nm. The collimated beam of w = 15 mm (radius at e^{-2}) was clipped by a 20.5 mm diameter iris and then focused to a 120 mm long cell with a vacuum focus 112 mm behind the front face of the cell. The cell was filled with 30 mbar of argon. The raw XUV spectrum and its spatial integration are depicted on Fig. 1. The exposure time was set to 10 ms. It corresponds to the overall XUV signal of 34.7 nJ, (corresponding to 5.6×10^9 photons) generated per shot (i.e. before metallic filters). This value gives an estimate of the conversion efficiency of 5×10^{-6} that is higher than the value expected from scaling [5]. The harmonic orders are wide due to high interaction intensity and ionization degree. Surprisingly, a lot of signal is contained in the 20 – 30 nm spectral region, which we attribute to generation in ions Ar^+. Also, the spectral structures in some harmonic peaks are due to nonlinear effects altering the driving pulse due to high intensity and long generating medium.
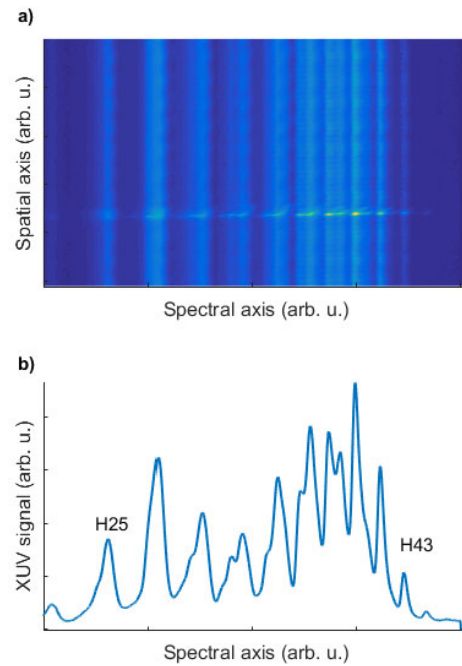
Fig. 1. (a) raw XUV spectrum and corresponding (b) spatial integration generated in argon cell. The spectrum was acquired after two Al filters of 1 and 2 μm thickness.

4. User Stations

Users of the HHG beamline can take advantage of two already installed scientific end stations: ELIps and MAC.

The ELIps station is optimized for experiments in XUV magneto-optical ellipsometry of solid-state targets [6]. It is equipped with rotatable reflecting XUV polarizers for polarization dependent experiments based on reflection or transmission [7]. Sample temperature can be applied on a sample and its temperature can be controlled by a cryostat and a switching magnetic field (+/-1.5 T) is under development.

The MAC is a multi-purpose station designed for investigating dynamics in low-density atomic and

molecular targets employing fs-synchronized beams of a broad spectral range (from soft x-ray to THz) [8]. It includes various detectors such as ToF spectrometers, velocity map imaging (VMI), magnetic bottle and X-ray CCD. Available sample delivery systems are for atomic/molecular beams, clusters and aerosols.

4. Conclusions

We presented recent results from the high-photon flux HHG beamline, its experimental setup, diagnostics and user stations. Although the beamline and the user station are already available for user experiments, a number of improvements are planned for the future. Moreover, with the deployment of further amplification OPCPA stages of the driving laser, we expect the XUV photon number produced via HHG to increase significantly.

References

[1]. G. A. Mourou, G. Korn, W. Sandner, J. L. Collier (Eds.), ELI Whitebook, *Andreas Thoss*, Berlin, 2011.

[2]. B. Rus, F. Batysta, J. Čáp, M. Divoky, *et al.,* Outline of the ELI-beamlines facility, *Proceeding of SPIE*, Vol. 8080, 2011, 808010.

[3] C. Heyl, H. Coudert-Alteirac, M. Miranda, M. Louisy, K. Kovács, V. Tosa, E. Balogh, K. Varjú, A. L'Huillier, A. Couairon, C. L. Arnold, Scale-invariant nonlinear optics in gases, *Optica*, Vol. 3, 2016, pp. 75-81.

[4] F. Batysta, R. Antipenkov, J. Novák, J. T. Green, J. A. Naylon, J. Horáček, M. Horáček, Z. Hubka, R. Boge, T. Mazanec, B. Himmel, P. Bakule, B. Rus, Broadband OPCPA system with 11 mJ output at 1 kHz, compressible to 12 fs, *Optics Express*, Vol. 24, 2016, pp. 17843-17848.

[5]. O. Hort, M. Albrecht, V. E. Nefedova, O. Finke, et al., High-flux source of coherent XUV pulses for user applications, *Optics Express*, Vol. 27, Issue 5, 2019, pp. 8871-8883.

[6]. S. Espinoza, G. Neuber, C. D. Brooks, B. Besner, et al., User oriented end-station on VUV pump-probe magneto-optical ellipsometry at ELI beamlines, *Applied Surface Science*, Vol. 421, 2017, pp. 378-382.

[7]. S. Espinoza, F. Samparisi, F. Frassetto, *et al.,* Characterization of the high harmonics source for the VUV ellipsometer at ELI Beamlines, *J. Vac. Sci. Technol. B*, Vol. 38, 2020, 024005.

[8]. M. Krikunova, N. Timneanu, J. Andreasson, Ultrafast Dynamics Driven by Intense Light Pulses (M. Kitzler, Ed.), *Springer*, 2016.

(058)

Ghost Modalities with Classical Correlated Photons Emitted by Semiconductor Devices: Quantum Metrology 64 Years after Hanbury-Brown & Twiss

Wolfgang Elsäßer

Institute of Applied Physics, Technische Universitaet Darmstadt, 64289 Darmstadt (Germany)
E-mail: Elsaesser@physik.tu-darmstadt.de

Summary: Ghost metrology is a measurement modality exploiting correlations of photons. In the spirit of the Hanbury-Brown & Twiss (HBT) experiment from 1956, well before the advent of the first laser, we discuss and apply photon correlations. First, we realize ghost imaging by using a novel, extremely compact super luminescent diode source based on Amplified Spontaneous Emission and exhibiting photon bunching with a second order correlation coefficient $g^{(2)} = 2$. Then, we demonstrate that amplified spontaneous emission light emitted by a spectrally broad-band semiconductor-based super luminescent diode exhibits spectral photon correlations in the spirit of the HBT experiment [1], however now in the spectral domain. We apply these spectral photon correlations within a proof-of-principal ghost spectroscopy experiments at an ab-sorption band of trichloromethane (chloroform) at 1214 nm reproducing the characteristic absorption features. This ghost spectroscopy work fills the gap of a hitherto missing analogy between the spatial and the spectral domain in classical ghost modalities. Finally, by exploiting polarization correlations of unpolarized light from an erbium-doped fibre amplifier, we succeed in reconstructing a hidden, camouflaged polarization in a ghost polarimetry experiment in close analogy to ghost imaging and ghost spectroscopy. Via these successfully demonstrated results we are contributing towards a broader dissemination of correlated photon ghost modalities, hence paving the way towards more applications which exploit their favorable advantages.

Keywords: Ghost metrology, Correlated photons, Imaging, Spectroscopy, Polarimetry, Superluminescent diodes.

1. Introduction

Ghost imaging (GI) is by far not a "spooky action" but rather a photon correlation imaging modality based on the fundamentals of quantum optics, either realized with entangled photons in the quantum GI version or with bunched photons from classical thermal sources. In contrast to conventional imaging systems, GI exploits intensity correlations of light to retrieve an image of an object. Ghost Imaging (GI) or photon-correlation imaging is one of the recent topics of quantum optics. After the first demonstration in 1995 with entangled photon [2] also classical GI [3, 4] has been demonstrated with light emitted by rather complex, bulky thermal light sources. The name GI results from the fact that the image is formed by light which has never interacted with the object. Hereby, the total intensity of the transmitted or reflected light of an illuminated object and the spatially resolved intensity of a highly (position)-correlated reference beam which itself has never interacted with the object, are detected. The information of both intensities alone is not enough to form an image of the object. However, correlating the two intensities in terms of the intensity autocorrelation or second order correlation yields an image, the ghost image.

2. Ghost Modalities – Experimental Results

Very recently, we introduced to field of ghost modalities a novel, extremely compact ultra-miniaturized superluminescent diode source [5]

based on Amplified Spontaneous Emission (ASE) in a classical GI experiment based on the full in-coherence of light as requested for classical GI, namely in 1st order coherence being spectrally broad-band, in 2nd order coherence exhibiting Hanbury-Brown & Twiss photon bunching with a correlation coefficient of two and being spatially incoherent due to the dynamic mode filamentation.

Here, the presentation will start with a description of the fundamentals of this GI modality with superluminescent diodes with a set-up schematically shown in Fig. 1 and ghost imaging results of a macroscopic double slit transmission object as depicted in Fig. 2. We then extend the field of ghost modalities in analogy to this classical spatial GI principle with classical light to ghost spectroscopy. We propose and realize a first ghost spectroscopy (GS) experiment with classical light by exploiting spectral correlations of light emitted by a semiconductor.-based superluminescent diode (SLD) and demonstrate the applicability of this ghost modality in a real-world proof-of-principle experiment by measuring a ghost absorption spectrum $\alpha(\lambda)$ of the characteristic absorption features of chloroform at 1214 nm, i.e. a ghost spectrum [6]. Fig. 3 shows the schematic realization of this set-up and Fig. 4 shows the proof-of-principle demonstration experiment with the ghost absorption spectrum of chloroform [7].

We then discuss further perspectives and possibilities of photon bunching in amplified spontaneous emission light suggesting the realization of ghost polarimetry (GP) [8]. By exploiting polarization correlations of unpolarized light from a

broadband fiber-based amplified spontaneous emission source we succeed in reconstructing a scrambled and thus camouflaged linear polarization state in the object arm in a ghost polarimetry experiment via a ghost polarigram [8] (see Figs. 3 and 4) in close analogy to ghost imaging and ghost spectroscopy.
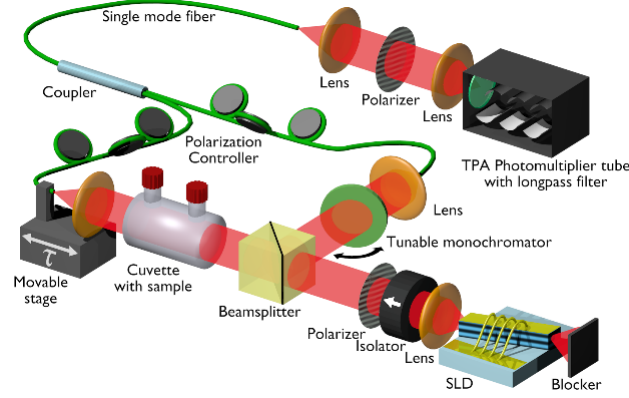
Fig. 1. Experimental set-up for the realization of a ghost spectroscopy at the absorption line of chloroform.
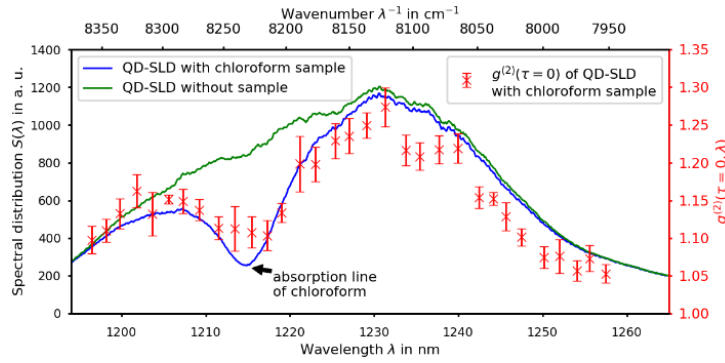
Fig. 2. Ghost Spectrum of an absorption feature of chloroform at 1215 nm measured with the set-up of Fig. 1: SLD spectrum (green), conventionally measured absorption spectrum of chloroform (blue, both left scale) and ghost spectrum (red) obtained via the spectral intensity correlation (right scale).
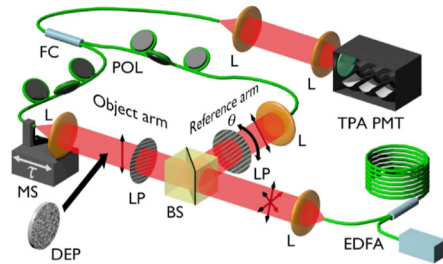

Fig. 3. Schematic depiction of the ghost polarimetry experiment in a standard classical ghost imaging setup.

3. Conclusions

In the spirit of the Hanbury-Brown & Twiss (HBT) experiment [1] we have demonstrated various ghost modalities, as ghost imaging, ghost spectroscopy and ghost polarimetry by exploiting classical photon correlations in light emitted by semiconductor-based superluminescent diodes and erbium-doped fibre amplifiers. We are convinced that this amplified emission source concept and the pursued and exploited analogy between ghost imaging and ghost spectroscopy will further fertilize the field, thus allowing to develop a deeper understanding of the experimental scheme and even leading to other ghost metrology protocols. It is expected that our findings will open perspectives for disseminating the ghost modality idea by exploiting classical correlated photons to enter further real-world applications in chemistry, physics and engineering.
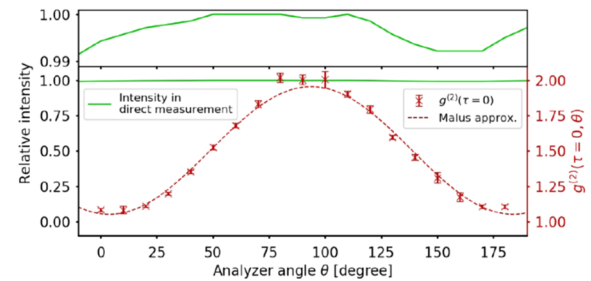
Fig. 4. Measured polarization-polarization second-order intensity correlations of light emitted by the ASE light source (red crosses; right scale), thus the measured ghost polarigram and a direct polarization measurement with a polarizer and an analyzer as a function of polarization angle θ (red dots; left scale). Both curves are fitted in terms of a Malus' law $\cos^2(\theta)$- dependence.

Acknowledgements

References

[1]. R. Hanbury Brown, R. Q. Twiss, Correlation between photons in two coherent beams of light, *Nature*, Vol. 177, 1956, pp. 27-29.

[2]. T. B. Pittmann, Y. H. Shih, D. V. Strekalov, A. V. Sergienko, Optical imaging by means of two-photon quantum entanglement, *Phys. Rev. A*, Vol. 52, 1995, R3429(R).

[3]. R. S. Bennink, S. J. Bentley, R. W. Boyd, "Two-photon" coincidence imaging with a classical source, *Phys. Rev. Lett.*, Vol. 89, 2002, 113601.

[4]. F. Ferri, D. Magatti, A. Gatti, M. Bache, E. Brambilla, L. A. Lugiato, High-resolution ghost image and ghost diffraction experiments with thermal light, *Phys. Rev. Lett.*, Vol. 94, 2005, 183602.

[5]. S. Hartmann, W. Elsäßer, A novel semiconductor-based, fully incoherent amplified spontaneous emission light source for ghost imaging, *Sci. Rep.*, Vol. 7, 2017, 41866.

[6]. P. Janassek, S. Blumenstein, W. Elsäßer, Ghost spectroscopy with classical thermal light emitted by a superluminescent diode, Phys. Rev. Appl., Vol. 9, 2018, 021001.

[7]. P. Janassek, S. Blumenstein, W. Elsäßer, Ghost spectroscopy with classical correlated amplified spontaneous emission photons emitted by an erbium-doped fiber amplifier, *Appl. Sci.*, Vol. 8, 1896, 2018.

[8]. P. Janassek, S. Blumenstein, W. Elsäßer, Recovering a hidden polarization by ghost polarimetry, *Opt. Lett.*, Vol. 43, 2018, pp. 883-886.

Spectroscopic Analysis of SWCNT Dimer: An Ab Initio Approach

D. Sharma [1]

[1] Department of Higher Education, Government of Haryana (India)
Deenbandhu Choturam University of Science, Technology and Management, Murthal (Haryana), India
Shaheed Udham Singh Government College, Matak-Majri (Haryana), India
Tel.: + 91-8813965077
E-mail: bhargava.dp@gmail.com

Summary: An ab initio approach based on density functional theory has been adopted for spectroscopic analysis of a Singlewalled Carbon Nanotube dimer comprising of two CNTs of different chiralities aligned together to form an inhomogeneous dimer. Raman Spectra of a (5, 0) CNT; a (6,0) CNT and a (5,0)- (6,0) CNT dimer comprising of parallel standing (5,0) and (6,0) CNTs held by weak Van der Waals were simulated using Quantum Espresso Code based on density functional theory. Ignoring the redundant modes which might arise due to the approximations, overall a red shift is observed that clearly affirms the stability and existence of the structure formed by conjugation of CNTs. In the RBM region, additional peaks can be seen arising out of the coupled vibrations. D-band peaks of the dimer cover the D-band peaks of both the CNTs as disorder in the constituents reflects in its constitution. In the G-band region arising out of tangential vibrations, a low wavelength component with Lorentzian shape and a weak high wavelength component with a Breit Wigner Fano (BWF) kind of lineshape suggest metallic nature of the inhomogeneous CNT dimer. Vibrational modes corresponding to significant peaks have been chalked out.

Keywords: Inhomogeneous CNT dimer, Simulation, Density functional theory, Molecular modeling, Vibrational modes, Raman spectra.

1. Introduction

The power of Raman spectroscopy as a probe and a characterization tool for carbon nano-materials is unquestionable. It provides useful information about significant properties of carbon nanotubes (CNTs) like chiral indices (n, m), diameter, strain analysis, purity index/ doping levels, functionalization status and the orientation. Especially for studying the inherent vibrational modes of carbon nanotubes, Raman spectroscopic techniques serve as a well trusted tool. Various techniques and technicalities; various dimensions of analytical approaches; various elaborate studies on experimental as well as theoretical aspects of vibrational analysis of CNTs have been well recorded establishing Raman spectroscopy as a means to chalk out the vibrational behavior of CNTs. Study of the interactions between elementary excitations like electrons, phonons, and plasmons is very crucial for predicting or manipulating their optical and electronic properties. SWCNTs being low-dimensional materials, the role of these interactions becomes even more effective and enhancement of interaction between these excitations greatly influences their physical properties. Spectroscopic studies henceforth provide significant input as far as optimization of the design of nanotube electronic/optoelectronic CNT device design is concerned and offers a key to understand better explore their phonon decay channels better. Combining the intriguing features of CNTs in conjugation with other nanomaterials makes their conjugated hybrid nanomaterials useful multidimensional structures having various potential applications like supercapacitors, Lithium rechargeable batteries, solar cells, sensors, photodiodes, PV(photovoltaic) cells, HR printable conductors, optical tunable devices, EM absorbers and highly efficient transistors... the list is endless. To utilize the peculiar characteristics of these novel nanomaterials developed through conjugation, one need to thoroughly study their molecular structure and that is where the vibrational spectroscopic methods come into the picture. As the vibration based applications of these 1-D tubules transit into the quantum regime, understanding of quantum coupling between electrons and phonons becomes necessary for which Raman spectroscopy is the ultimate tool. A number of spectroscopic studies, experimental as well as theoretical, have already been reported in the literature but the effect of conjugation of CNT with itself i.e. with another CNT with same or different chirality is still to be explored well. Conjugation of two free standing SWCNTs held together by weak Vander Waal's interaction constitute a SWCNT-dimer. In 2014, Levisohn *et. al.* marked a free-standing dimer of SWCNTs using HRTEM and determined its structure using electron diffraction patters. This dimer constituted of two interacting semiconducting SWNTs with chiralities (15, 11) and (16, 12). They used spectral moment method to determine the Raman Spectra. In this paper, we have calculated the Raman spectra of two zigzag SWCNTs of chiralities (5, 0) and (6, 0) and a (5, 0) - (6, 0) CNT dimer using density functional theory based calculations to study the effect of conjugation of two free standing SWCNTs forming an inhomogeneous SWCNT dimer.

2. Computational Details

The Raman spectra calculations were performed with the Quantum-Espresso (QE) package Theoretical evaluation of the Raman spectra requires first-, second-, and third-order energy derivatives, among which the most demanding are the second-order derivatives of the energy with respect to the atomic positions (force constants) and the third-order polarizability derivatives, twice with respect to the electric field (yielding polarizability) and once with respect to the atomic positions (Raman intensity tensors). The important advantage of the Quantum Espresso code is that the polarizability derivatives have been recently implemented via a second-order response formalism thus making their calculation relatively inexpensive compared to that of the force constants. To avoid the effect of the finite edges, we adopted a periodic supercell approach. In all of our calculations, we used the Local Density approximation (LDA) exchange correlation functional and treated the valence-core interaction for the electrons with norm-conserving pseudo potentials in reciprocal space. The electronic wave functions were expanded in plane wave basis set with finite basis set correction. The lattice vectors were optimized in the plane and the atomic positions in the supercell by variable cell dynamics. The residual stress in the optimized structures did not exceed 300 MPa. A plane wave expansion cutoff of 500 eV for the wave functions and of 2000 eV for the charge density was used. The Brillouin zone integration was performed using the Monkhorst-Pack scheme.

3. Results and Discussions

The spectra reveal that along with the usual Radial Breathing Mode peaks, D-Mode peaks and G-Mode peaks, a number of peaks are visible in the frequency range 300-1000 cm^{-1}. These peaks are known as Intermediate frequency mode peaks. If the redundant modes are ignored in view of a lot of approximations involved, an overall red shift is observed in the spectra of the individual SWCNTs as a result of conjugation which indicates the stability of the conjugated structure.

Peak-splitting was observed in G-mode and DMode peaks as a consequence of the tube-tube interaction. The Radial Breathing Mode originates from the out-of-plane transverse acoustic mode of graphene. This mode does not generate an electron-phonon interaction in graphene, but does do so in SWCNTs, such that the RBM can be observed in SWCNTs.

The origin of Intermediate Frequency Mode peaks is the out-of-plane acoustic phonon branch of graphene

that transforms to an "acoustic-like" optical branch in the tubular structure of SWCNTs.
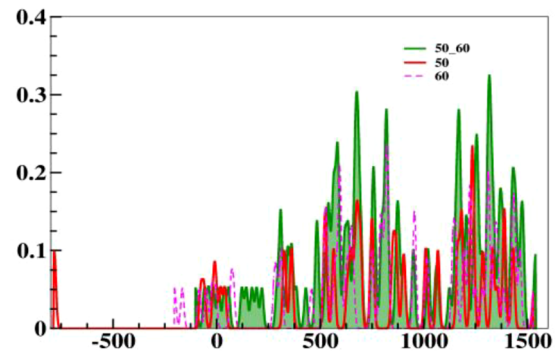

Fig. 1. Raman Spectra of a (5, 0) CNT; a (6, 0) CNT and a (5, 0) - (6,0) CNT dimer.

4. Conclusions

Significant alterations are observed in SWCNT spectra when they conjugate to form SWCNT dimer held together by weak Van der Waal's forces. These changes may be studied to throw light on tube-tube interactions, electron-phonon interactions and the vibrational aspects of conjugation and enrich the basic physics related to carbon nanotubes.

Acknowledgements

References

[1]. P. Giannozzi, *et. al.*, QUANTUM ESPRESSO: A modular and open-source software project for quantum simulations of Materials, *Journal of Physics: Condensed Matter*, Vol. 21, Issue 39, 2009, 395502.

[2]. S. Baroni, *et. al.*, Phonons and related crystal properties from density functional perturbation theory, *Reviews of Modern Physics*, Vol.73, Issue 2, 2001, 515.

[3]. D. Catalin, *et. al.*, Excitonic effects and optical spectra of single-walled carbon nanotubes, *Physical Review Letters*, Vol.92, Issue 7, 2004, 077402.

[4]. G. S. Duesberg, *et. al.*, Polarized Raman spectroscopy on isolated single-wall carbon nanotubes, *Physical Review Letters*, Vol. 85, Issue 25, 2000, pp. 5436-5439.

(072)

General Framework to Derive Casimir Force of Electromagnetic Field in Non-inertial Reference Frames

B. Markowicz [1], **K. Dębski** [1], **M. Kolanowski** [1], **W. Kamiński** [1] and **A. Dragan** [1]

[1] Institute of Theoretical Physics, University of Warsaw, Pasteura 5, 02-093 Warsaw, Poland
Tel.: + 48 666 36 216 5
E-mail: b.markowicz3@student.uw.edu.pl

Summary: Study of the Casimir effect allows to observe non-trivial behavior of quantum vacuum - the simplest state of the electromagnetic field. Casimir force (CF) has been studied in many different cases. Attempts were also made to analyze the CF for a cavity located in non-inertial reference frames. However, these attempts led to questionable results.

Here we present a general framework that allows us determine the CF in a system of mirrors moving on any trajectory in 1+1 and 3+1 dimensional Minkowski space time (ST) and in any conformally invariant ST with the Minkowski ST. We analyzed the framework on the example of a system of uniformly accelerating mirrors described by Rindler coordinates and in De Sitter expanding universe. The case of uniformly accelerating cavity, by virtue of the principle of equivalence, is analogous to the case of a cavity placed in a gravitational field. Obtained here expressions for CF can be used to determine parameters of space near the cavity for example Hubble constant or intensity of local gravitational field. We also discuss the problem of defining force in non-inertial systems as a measure of the interaction between matter and the electromagnetic field.

Keywords: Casimir effect, Electromagnetic field, Non-inertial frame, Rindler coordinates, De Sitter Space time.

1. Introduction

CF can be defined in two ways. First as the work needed to be introduced into the system to move one of the plates by a unit distance and the second way as the pressure that the field exerts on the plates limiting the cavity. Both approaches gives same results in Minkowski ST for resting plates. However, when plates are moving along non-inertial trajectory aforesaid definitions of CF are no longer equivalent.

First approach, the most popular one [1, 2] turns out to be incorrect due to false implicit assumption that time run with the same speed in different space points. In the next chapter we show application of field pressure approach in the simplest possible case.

2. Field Pressure Approach

Let us Consider a 1+1 dimensional cavity limited by uniformly accelerating plates. The plates accelerate in a way that at any time in the cavity's rest frame the length of the cavity is equal to L. To operate in the mentioned frame, we introduce Rindler coordinates (τ, χ) associated with Minkowski coordinates (t, x) via the transformation

$$\chi = \sqrt{x^2 - t^2} \qquad \tau = \frac{1}{a} \tanh^{-1} \frac{t}{x}, \qquad (1)$$

where a is a transformation parameter. Body moving on trajectory with $\chi = const.$ has constant acceleration [3]. In the rest frame of cavity, the plates are placed at $\chi = A$ and $\chi = B$, as shown in the Fig. 1.

Accelerating cavity seen in
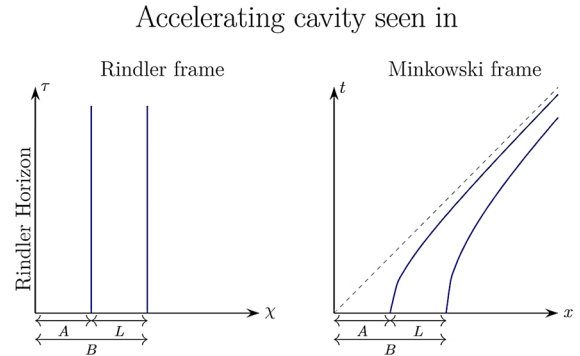
Fig. 1. The graphs show the ST trajectories of uniformly accelerating plates in the Rindler frame (τ, χ) and in the Minkowski frame (t, x) in which at $t = 0$ plates are in rest.

Let's consider the force acting on the accelerating plate from the point of view of an inertial observer and identify the CF that the inertial observer sees when the cavity rests in its frame with the actual force acting on the plate. By actual force we understand the force measured by point-like dynamometers attached to the plates. We will conduct considerations in inertial frame in which plates are at rest at the $t = 0$.

From our inertial observer's point of view, field pressure acting on the right plate can be written as the energy momentum tensor (EMT) evaluated at the vacuum state contracted with the spatial Killing vector in Minkowski ST and a unit vector normal to the surface of the plate [4]. By Subtracting pressure acting from the left and right site of the plate we obtain CF

$$F_c = -\frac{\pi \cosh a\tau}{12 B^2 \log^2 \frac{B}{A}} \qquad (2)$$

Let us note that the obtained force depends on time! However, from the very beginning of the derivation, we knew that the force will be equivalent to the actual CF only at the moment $\tau = 0$. Then CF gets simplified to

$$F_c = -\frac{\pi}{12B^2 \log^2 \frac{B}{A}} \qquad (3)$$

Presented method gives the correct results whenever we are able to introduce a comoving frame, i.e. when the mirrors move along any trajectory in a flat ST or in a conformally flat ST.

3. Stress Tensor from Conformal Anomaly

The field pressure method is intuitive but can lead to complex calculations due to finding eigenmodes of the field inside and outside the cavity, which are necessary to find EMT. The method presented in this chapter allows us to simplify the process of finding EMT.

In the classical case, the EMT trace should disappear. However, in quantum case this principle ceases to apply. This effect is known as conformal anomaly. Interestingly enough, that trace has a universal, geometric structure – it depends only upon a curvature of a background and not on a state on which it is evaluated. In 1+1 ST it is given by [5]:

$$\langle \hat{T}^\mu_{\ \mu} \rangle_{d=2} = -\frac{R}{24\pi}, \qquad (4)$$

where R is the Ricci Tensor. Surprisingly, it is enough to know merely conformal anomaly to recover transformation law for EMT evaluated on state picked by us state upon conformal transformations defined as

$$\eta_{\mu\nu}(x) \mapsto e^{2\sigma(x)}\eta_{\mu\nu}(x) = g_{\mu\nu}(x)$$
$$\phi(x) \mapsto e^{-n\sigma(x)}\phi(x) \qquad (5)$$

We have [6]:

$$\langle \hat{T}_{\mu\nu} \rangle_{d=2} = \langle \hat{T}_{\mu\nu} \rangle_0 +$$
$$\frac{1}{12\pi} \left[\sigma_{;\nu\mu} - \sigma_{;\mu}\sigma_{;\nu} + \eta_{\mu\nu} \left(\frac{1}{2}\sigma_{;\xi}\sigma^{;\xi} - \sigma^{;\xi}_{\ ;\xi} \right) \right], \qquad (6)$$

where first term on the right is expectation value of EMT of a state pull-backed by conformal transformation to the Minkowski ST.

Equipped with that knowledge, we can lay down our strategy. We look for a coordinate system (t,x^j) and a conformal factor e^σ such that

$$g = e^{2\sigma} \left(dt^2 - \delta_{ij}dx^i dx^j \right), \qquad (7)$$

and mirrors trajectories are given by $x = const.$ Then, we can calculate in this coordinate system EMT for stationary vacuum with appropriate boundary conditions and transform it back to our background via (6). After determining EMT, deriving CF is just straightforward continuation of procedure described in Section 3.

4. Conclusions

The derived framework allows us to effectively determine CF for plates moving along any trajectory in a 1+1 or 3+1 dimensional conformally flat TS resulting from the interaction of plates with the electromagnetic field. Application of the framework to uniformly accelerating plates leads to the result (3). Framework can be also applied to 3+1 dim De Sitter ST with metric

$$ds^2 = \frac{1}{H^2\eta^2} \left(d\eta^2 - \delta_{ij}dx^i dx^j \right), \qquad (8)$$

which describes a uniformly expanding universe with Hubble constant - H. CF in that universe take form

$$F_c = \frac{\pi^2 H^2 \eta^2}{240 L^4} - \frac{31 H^4}{480 \pi^2} \qquad (9)$$

References

[1]. H. B. G. Casimir, On the attraction between two perfectly conducting plates, *Proceedings of the Koninklijke Nederlandse Akademie van Wetenschappen*, Vol. 5, 1948, pp. 261-263.

[2]. A. A. Saharian, R. S. Davtyan, A. H. Yeranyan, Casimir energy in the Fulling-Rindler vacuum, *Physical Review D*, Vol. 69, Issue 8, 2004, 085002.

[3]. W. Rindler, Essential Relativity – Special, General, and Cosmological, *Springer-Verlag*, New York, 1969.

[4]. R. M. Wald, General Relativity, *Chicago University Press*, 1894.

[5]. S. M. Christensen, M. J. Duff, Axial and conformal anomalies for arbitrary spin in gravity and supergravity, *Physics Letters B*, Vol. 78, Issue 5, 1978, pp. 571-574.

[6]. L. S. Brown, J. P. Cassidy, Stress tensors and their trace anomalies in conformally flat space-times, *Physical Review D*, Vol. 16, Issue 6, 1977, pp. 1712-1716.

(075)

Optical Development Steps of a Fully Integrated Miniature Spectrometer Designed for Injection Molding Fabrication

M. Haupt [1] and U. H. P. Fischer-Hirchert [2]

[1] Jade University of Applied Sciences, Friedrich-Paffrath-Str. 101, 26389 Wilhelmshaven, Germany
[2] Harz University of Applied Sciences, Friedrichstr. 57-59, 38855 Wernigerode, Germany
Tel.: + 49 4421 985 2625, fax: +49 4421 985 2304
E-mail: matthias.haupt@jade-hs.de

Summary: Optical simulation software based on the ray tracing method offers easy and fast results in imaging optics. This method can also be applied in other fields of light propagation, e.g. non-imaging optics. In this paper a miniature spectrometer designed and developed by means of ray tracing will be discussed. Compared to the classical optical design, requirements for optimal design of this element differ particularly with regard to the spatial separation of the different wavelengths and the complete transmission of light to achieve the best signal-to-noise ratio. The basis of the presented element is a Rowland spectrometer. But for the complete guidance of light that emerges the entrance split the design of this element has to be changed fundamentally, especially when a high numerical aperture of the light beam is taken into account. A monolithic approach is presented with a blazed grating based on an aspheric mirror to suppress most of the aberrations. The grating is analyzed for different diffraction orders and the best possible efficiency. On the exit of this element the light must be guided into different photo diodes with different effective areas. In general, the element should be designed in a way that it can be produced with a mass production technology like injection molding in order to offer a reasonable price. The paper will describe the development of this miniature spectrometer step by step by means of ray tracing simulations.

Keywords: WDM, Polymer optical fibers, Multiplexing, Raytracing, Rowland spectrometer.

1. Introduction

1.1. Advantages of Polymer Optical Fibers

Polymer Optical Fibers (POFs) offer many advantages compared to alternate data communication solutions such as glass fibers, copper cables and wireless communication systems. In comparison with glass fibers, POFs offer easy and cost-efficient processing and are more flexible for plug interconnections. POFs can be passed with smaller radius of curvature and without any mechanical disruption because of the larger diameter compared to glass fibers.

The advantage of using glass fibers is their low attenuation, which is below 0.3 dB/km in the infrared range. In comparison, POF can only provide acceptable attenuation in the visible spectrum from 400 nm up to 700 nm, see Fig. 1. The attenuation has its minimum with about 85 dB/km at approximately 570 nm. For this reason, POF can only be efficiently used for short distance communication up to 100 m and the disadvantage of the larger core diameter is higher mode dispersion.

The use of copper as communication medium is technically outdated, but still the standard for short distance communication. In comparison, POF offers lower weight and space. Another reason is the nonexistent susceptibility to any kind of electromagnetic interference [1-3].

Wireless communication is afflicted with two main disadvantages. The electromagnetic fields can disturb each other and probably other electronic devices.

Additionally, wireless communication technologies provide almost no safeguards against unwarranted eavesdropping by third parties, which makes this technology unsuitable for the secure transmission of volatile and sensitive business information.
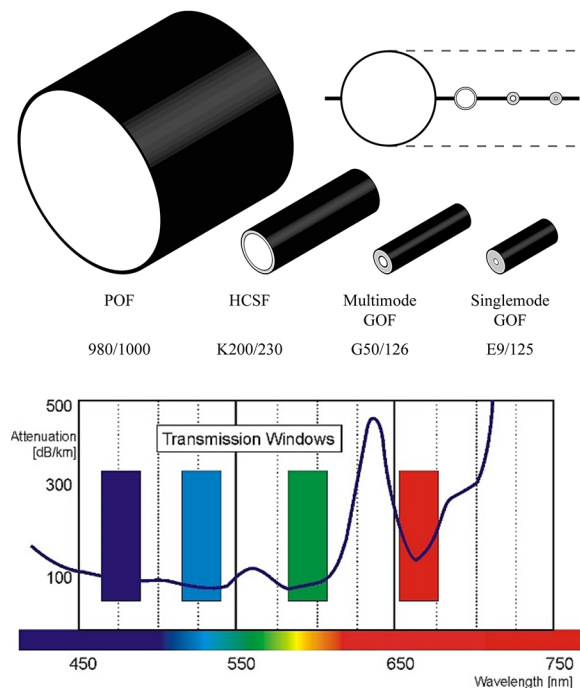
Fig. 1. Principle and attenuation of POF in the visible range [1].

1.2. The Motivation for WDM over POF

POF offers advantages compared to the established technologies. This leads to a broad usability in different sectors, such as the automotive, the in-house or the industrial sectors. This kind of fiber can also be applied for aviation or the medical sector. All these applications have one thing in common – they all need high-speed communication systems [4-7].

The standard communication over POF uses only one single channel [1, 2]. To increase bandwidth for this technology the only possibility is to increase the data rate, which lowers the signal-to-noise ratio and therefore only can be improved in small limitations.

This paper presents a possibility to open up this bottleneck. In glass fiber technology, the use of the WDM (wavelength division multiplexing) in the infrared range at about 1550 nm has long been established [8-10]. This multiplexing technology uses multiple wavelengths to carry information over a single fiber [11]. This basic concept can – in theory – also be assigned to POF. However POF shows different attenuation behavior, see Fig. 1. For this reason, only the visible spectrum can be applied when using POF for communication.

For WDM, two key-elements are indispensable: a multiplexer and a demultiplexer. The multiplexer is placed before the single fiber to integrate every wavelength to a single waveguide. The second element, the demultiplexer, is placed behind the fiber to regain every discrete wavelength. Therefore, the polychromatic light must be split in its monochromatic parts to regain the information. These two components are well known for infrared telecom systems, but must be re-developed for POF, because of the different transmission windows.

One technical solution for this problem is available [12], but it cannot be efficiently utilized in the POF application scenario described here, mostly because this solution is afflicted with high costs and therefore not applicable for any mass production.

2. Basic Concept of the Demultiplexer

As mentioned before, a demultiplexer is essential for WDM. Several preconditions must be fulfilled to create a functional demultiplexer for POF. First of all, the divergent light beam, which escapes the POF, must be focused. This is done by an on-axis mirror. In the first attempt, a spherical mirror is used. To get perfect results without any spherical aberrations, an ellipsoid mirror should be used.

The second function is the separation of the different transmitted wavelengths. In Fig. 2, this principle is illustrated for three wavelengths (red, green, blue). This is not a limitation for possible future developments, but rather an experimental basis from where to run the various simulations described below. The diffraction is done by a diffraction grating. The diffraction is split into different orders of diffraction.

The first order is the important one to regain all information. There a detector line can be installed to detect the signals.

Because the grating is attached to a bended basement only one element can cover both functions, the focusing and the diffracting. The higher the grating constant g of the diffraction grating is the sharper are the maxima of the different diffraction orders. The diffracted light interfere positively on the detection layer for:

$$z\lambda = g(\sin\alpha + \sin\beta) \qquad (1)$$

The resolution of the diffraction grating follows the Rayleigh Criterion and depends on the complete number of grating steps N and not on the grating constant:

$$\frac{\lambda}{\Delta\lambda} \leq zN \qquad (2)$$

The light is also not afflicted with any aberrations or attenuations of a focusing lens or other refractive elements, which are necessary for any other setup [13, 14].

Another characteristic of key elements for POF communication is the three dimensional approach. Key elements of glass fiber communication are usually designed planar. This simplification cannot be adopted for POF communication, because of the large Numerical Aperture of the POF.
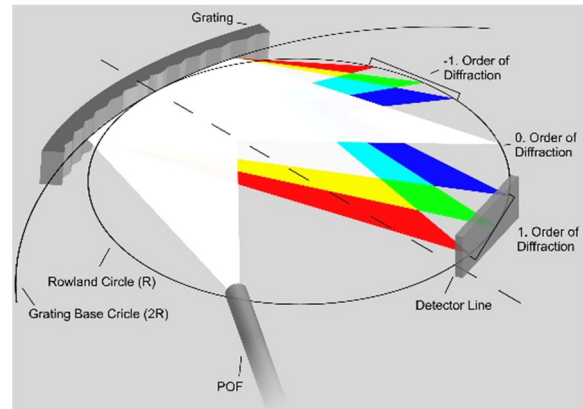

Fig. 2. Principle sketch of a Rowland spectrometer.

3. Results of the Simulation

In the following steps, an optical simulation software is used to design a demultiplexer based on the general concept outlined above. For the current task, the software OpTaLiX provides all required functionalities [15]. This approach offers different advantages: It is easy to design a setup and to analyze and to evaluate the simulated results. Furthermore, effective improvements of the configuration can be simulated quickly.

In Fig. 3, the 2D plot of the demultiplexer with an ellipsoid mirror and a grating is shown. The multicolored light, consisting of three wavelength (450, 520 and 650 nm) is emitted by a polymeric fiber. It hits the aspheric mirror, where it is focused and diffracted in its monochromatic parts. The light is focused onto a POF- or detector-array.
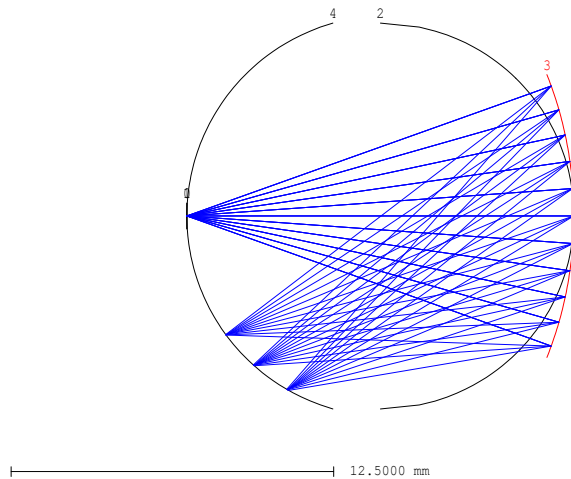
Fig. 3. 2D plot of the demultiplexer.

Without a grating, a perfect point to point mapping (without any aberrations) is possible with an ellipsoid mirror because of the two foci, but there is no separation of the different channels. With a grating stamped on the mirror, the separation of the multicolored light in its monochromatic parts is possible. But this grating distorts the optical path of light dramatically.

The first change is that the gap of the different colors in the image layer (here the POF- or detector array) increases with the line density of the grating. This can be noticed for an ellipsoid mirror and for a spherical mirror as well. The advantage of the spherical mirror is that the shape can be produced for injection molding easier. This optimization process was shown in different papers before [13, 16].

The result so far is that the demultiplexer can separate three colors with enough space between them to regain the information with a POF- or detector-array. The shapes of the foci feature low coupling losses and the shape of the mirror is producible in injection molding.

The mentioned results are satisfying for the optical requirements, but there are manufacturing requirements of this device as well. However, the line density of 1200 l/mm for the first diffraction order is too high for mass production. The goal is to produce a key component for high-speed POF communication for a reasonable price. The structure size of the grating is very small. To solve this problem, higher diffraction orders can be used, meaning that the second and the third order will be researched further on.

3.1. Grating Efficiency for Different Diffraction Orders

Focusing of the light is one part of the setup. The other task is separating the different wavelengths. Both of them is done by a dispersion grating based on an aspheric mirror. This grating can only be optimized for one diffraction order. A simple linear grating guides most of the light into the first diffraction order. But to reduce the line density of the grating for better manufacturing possibilities a higher order (second or third) should be used instead. Therefore a blazed grating must be applied. This Littrow configuration optimizes the light guidance in a higher diffraction order. But this kind of grating can only be improved to nearly 100 % for a single wavelength. It is common to use a green peak wavelength for the whole visible spectrum to get the best efficiency. The result of this optimization of the grating is shown in Fig. 4 for the first, the second and the third diffraction order.

The first order of diffraction exhibits the best efficiency. The value is above 60 % for the complete visible spectrum, but is not applicable in our case due to problems with the fabrication. The second order of diffraction offers more than 40 % of efficiency in the range from 450 nm to 650 nm. The third order has two maxima: at 470 nm and 630 nm to cover a larger wavelength range, but the efficiency is not higher than 50 %. That means 3 dB of the power will be lost just for the grating. This is too much for the insertion loss of this component. Consequently the second order seems to be the only suitable order of diffraction. This is not the only reason for the use of the second order. Third and higher orders will be overlapped in the visible region by lower orders and this will cause crosstalk.

3.2. Examination of Image Layer for the Blazed Grating

The shape of the foci in the detection layer will not be changed dramatically by optimizing the grating. The higher the line density the larger is the gap between the colors. But this will also lead to greater aberrations. Therefore, it is easy to find the right line density for the grating. The line density of the grating must be high enough to separate every color in the image layer. So the distance must be at least 0.5 mm between the blue and the green focus point and also between the green and the red focus point. Higher line densities would lead to greater aberrations and to more problems in the fabrication process. The image layer for the second order of diffraction and a line density of 500 l/mm is shown in Figs. 5 and 6. As can be seen, this parameters fit well to the requirement. An additional fourth color with a wavelength of 405 nm is added. Also the radii in the x- and y-axis are optimized to suppress the astigmatism caused by the Rowland spectrometer setup. This works well in one direction but in the other direction the astigmatism will remain even for the optimized setup.
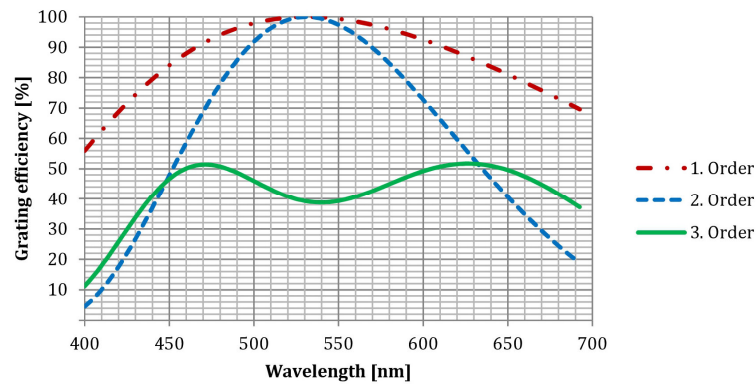
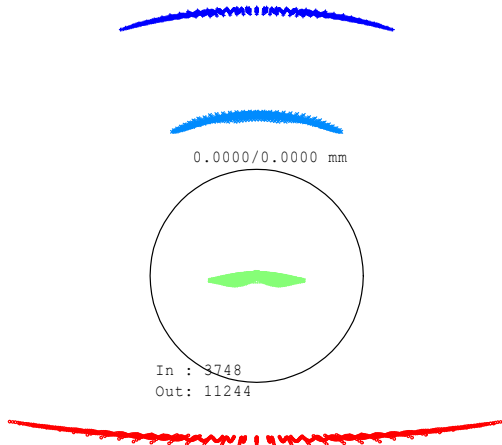**Fig. 4.** Grating efficiency for different diffraction orders.

Fig. 5. Spot diagram (not optimized, circle diameter 1 mm).

Fig. 7. Image layer of the setup for an area light source.
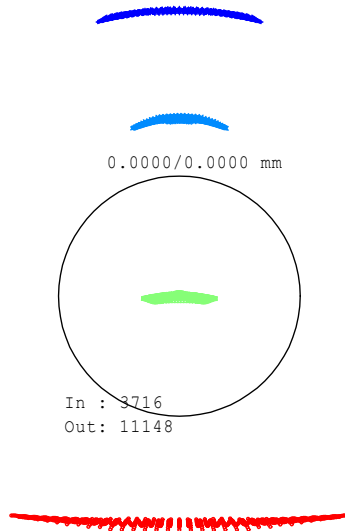

Fig. 6. Spot diagram (optimized, circle diameter 1 mm).

The spot diagram can only give a hint of the real size of the focus points, because the rays were sent through the optical systems by an ideal source. But in the setup the source will be a POF, with a core diameter of 0.98 mm. This will lead to larger focus points. To get a realistic estimation, the simulation is enhanced to an area light source with a diameter of 0.98 mm. The result can be seen in Fig. 7.
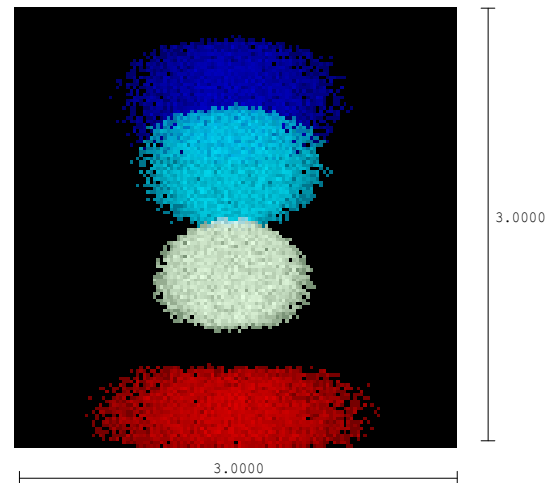
4. Conclusion

The Polymer Optical Fiber exhibits many advantages in comparison to glass fiber and copper for short-howl communication.

State of the art for POF communication is the use of only one single channel. This means a limitation of bandwidth. The solution for this bottleneck is WDM over POF, where not only one channel is used to transmit the information over a single fiber. To use this technique, two key elements: a multiplexer and a demultiplexer have to be designed completely new, because already established key elements for WDM communication over glass fiber in the infrared range cannot be applied.

The simulation results show that it is possible to build up a demultiplexer by means of a Rowland spectrometer. A special shape of the mirror is needed to suppress most of the aberrations, which results from the grating. The improved demultiplexer can separate three colors without any overlap. But for four colors this setup will gain high crosstalk (Fig. 7). Therefore, the basic idea of focusing the light with different wavelength by means of adjusting the two radii should be reconsidered. Besides increasing the line density an alternative could be the use of a holographic grating. But this will lead to higher production costs. The

grating efficiency for the second order of diffraction is suitable for source in the range of 450 nm to 650 nm and the setup can also be used as a spectrometer in the visible wavelength range.

References

[1]. W. Daum, J. Krauser, P. E. Zamzow, O. Ziemann, POF – Polymer Optical Fibers for Data Communication, *Springer-Verlag*, Heidelberg, 2002.

[2]. H. S. Nalwa, Polymer Optical Fibers, *American Scientific Publishers*, California, 2004.

[3]. J. Marcou, Plastic Optical Fibres – Practical Applications, *John Wiley & Sons*, Masson, 1997.

[4]. J. Brandrup, E. H. Immergut, E. A. Grulke, Polymer Handbook, *Wiley-Interscience*, 1999.

[5]. Infineon Technologies AG, Infineon Technologies, http://www.infineon.com/de/

[6]. H. Kragl, A Product Family for Simplex POF Home Networks, http://www.pofac.de/itg/fg_5_4_1/de/ fachgruppentreffen/treffen21.php

[7]. R. T. Chen, G. F. Lipscomb (Eds.), WDM and photonic switching devices for network applications, *Proceedings of SPIE*, Vol. 3949, 2000.

[8]. J. Colachino, Mux/DeMux Optical Specifications and Measurements, White Paper, *Lightchip, Inc*., Lightreading, 2001.

[9]. A. H. Gnauck, A. R. Chraplyvy, R. W. Tkach, *et al*., One terabit/s transmission experiment, in *Proceedings of the Conference on Optical Fiber Communication (OFC'96)*, 1996.

[10]. C. R. Batchellor, B. T. Debney, A. M. Thorley, T. J. B. Swanenburg, G. Heydt, F. Auracher, *et. al.,* A coherent multichannel demonstrator, *Electr. & Comm. Engineer. J.*, Vol. 4, Issue 4, 1992, pp. 235-242.

[11]. E. Voges, K. Petermann, Optische Kommunikationstechnik, *Springer-Verlag*, Heidelberg, 2002.

[12]. Fraunhofer Institute for Integrated Circuits, Optical Multiplexer for Short Range Communication, http://www.iis.fraunhofer.de/ec/oc/download/demux. pdf.

[13]. U. H. P. Fischer, M. Haupt, WDM over POF: The inexpensive way to breakthrough the limitation of bandwidth of standard POF communication, *Proceedings of SPIE*, Vol. 6478, 2007, 64780I.

[14]. A. Last, J. Mohr, Fehllicht in LIGA-Mikrospektrometern, *Forschungszentrum Karlsruhe Wiss. Berichte*, 2003.

[15]. H. Blechinger, OpTaliX: Optical Design Software, http://www.optenso.com

[16]. U. H. P. Fischer, M., Haupt, Advanced integrated WDM system for POF communication, *Proceedings of SPIE*, Vol. 7234, 2009, 72340C.

(078)

In Vitro Study of Ti Implants with Laser-functionalized Surface

<u>Yu. Karlagina</u> [1], G. Odintsova [1], E. Egorova [1], N. Shchedrina [1], C. Zernitskaia [2], K. Doll [3], B. Chichkov [4] and V. Veiko [1]

[1] ITMO University, International laboratory 'Laser micro-and nanotechnologies', 197101, 49 Kronverkskiy pr., St. Petersburg, Russia
[2] Pavlov First Saint Petersburg State Medical University, Dental clinic 'Hollywood smile', 197136, 7 Vsevoloda Vyshnevskogo st., St. Petersburg, Russia
[3] Clinic for Dental Prosthetics and Biomedical Materials Science, Hannover Medical School, 30625, 1 Carl-Neuberg-Straße, Hannover, Germany
[4] Laser Zentrum Hannover e.V., Hollerithallee 8, D-30419, Hannover, Germany
E-mail: jujukarlagina@ifmo.ru

Summary: Current study investigates how the surface relief of an implant affects cell behavior, bacterial adhesion and biofilm formation. We have conducted an *in vitro* study for human bone marrow mesenchymal stem cells and *Streptococcus oralis.* Study has demonstrated grooved relief with the distance between the peaks with subcellular to cellular scales are beneficial for life-sustaining activity of cells. The results of bacteriological study has demonstrated visible passive antibacterial effect of blue oxide (anatase) coating.

Keywords: Titanium implants, Laser modification, Biointegration, Biocompatibility, Microstructuring, Nanostructuring.

1. Introduction

In modern dental implantology two problems can be distinguished: osseointegration and microbial resistance. The solutions of them in most cases is mutually exclusive. To ensure the osseointegration of the implant in the body, it is necessary to provide its biocompatibility. For the further success of the implants and prevention of postoperative complications, a high microbial resistance is necessary as well.

It was shown that that relief, roughness, wettability and chemical composition of titanium implant surface are crucial points for its biocompatibility [1, 2]. Different methods applied to change surface relief and chemical composition [3]. The most commonly used parameters for surface characterization are a height-descriptive parameters, usually Sa and Sdr [4]. We suppose that the interaction between cells and implants also depends on such relief peculiarities as continuous or discontinuous topography, subcellular distance between peaks and presence of nano-roughness or nano-structures.

In addition there is a need to develop a biocidal surface for bacteria formed on the neck of the implant and the abutment. Numerous advances were proposed to improve antibacterial properties of the implants [5, 6]. It should be noticed that existing methods allow the formation of antibacterial coatings, which are harmful not only for bacteria but also for cells.

This work aims to:

1. Verify the hypothesis which states that bone cells need not only a rough surface just for fixing, but also a special relief to provide comfortable life-sustaining activity of cells throughout their lives;
2. Find laser-induced surface coating to provide antibacterial properties.

2. Results and Discussion

2.1. Sample Preparation

The surface of Ti–6A1–4V disks (1 mm thickness, 5 mm diameter) was processed by the ytterbium pulsed fiber laser (1064 nm, 20 W, 100 and 200 ns, 10-100 kHz, 50 µm). Line-by-line scanning of the surface was performed with overlapping laser pulses along the X and Y axis with the fixed-step. Different laser modes was developed to provide subcellular-sized reliefs and color oxide coatings (TiO_2 anatase) (see Fig. 1(1)).

2.2. *In vitro* Study

The hMSCs proliferation study showed that, compared with the untreated titanium surface, the cells proliferated perfectly in all reliefs. The results obtained showed the cells cover both tops and bottoms of the reliefs, as well as grow inward in open pores. It was noted that the shape and size of the cell nuclei for the different reliefs diverge. The osteocalcin expression study showed that osteogenesis occurred on all reliefs (see Fig. 1(2)). The data are confirmed by the results of the ALP activity test. The maximum number of cells and greatest amount of osteocalcin was found for the «Grooves» relief. This relief affects the spatial orientation of cells: hMSCs extend along the grooves.

2.3. Bacterial Adhesion and Biofilm Formation

Analysis of bacterial adhesion and biofilm formation of *Streptococcus oralis* strain ATCC 9811 was performed. Analysis of 3D-reconstructions (see Fig. 1 (3, 4)) clearly shows that there is no anti-adhesive or anti-biofilm effect for reliefs. In contrast, for the blue surface, a slight reduction in bacterial adhesion and biofilm formation might be observed visually.
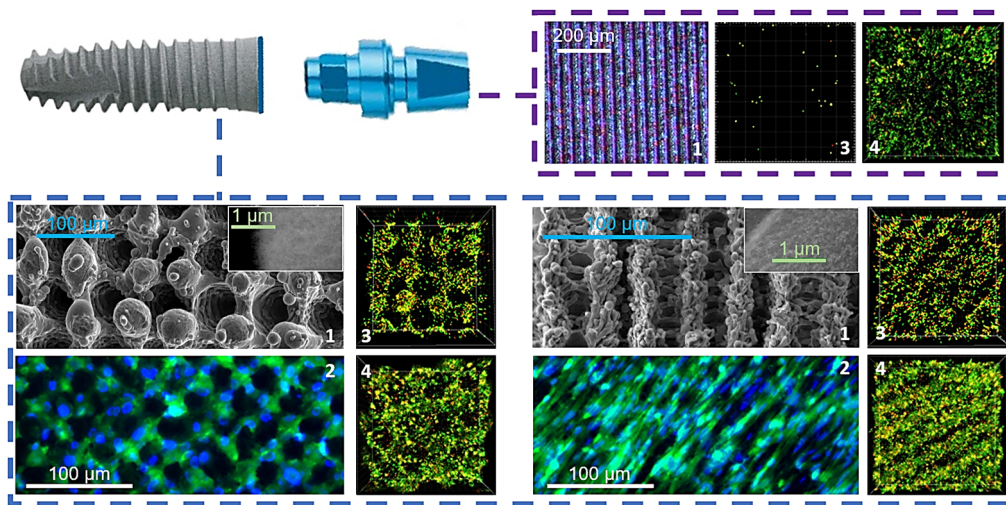
Fig. 1. Dental implant with laser-functionalized surface. Blue box – structures for implant body (1), in vitro: expression of osteocalcin (2), bacterial adhesion (3) and biofilm formation (4). Purple box – color laser oxidation (1).

4. Conclusions

This study demonstrates that a type of the surface relief affected cell behavior and bone tissue response. We have found that it is beneficial for cells to have not individual slots, but structures like a grooves, with the distance between the peaks with subcellular to cellular scales. The results of this comprehensive study show that the cells-surface interaction are affected not only by surface micro-roughness, as most implant manufacturers claims, but also by the relief, which includes continuous topography with the features less than 50 μm and the presence of nano-structures.

We have found that bacterial adhesion and biofilm formation are active on the reliefs due to the fact that the surface structures are several magnitudes bigger than bacterial cells. Thus, bacteria just behave like on an increased surface area. Our blue oxide (anatase) coating has positive effect on antibacterial properties.

Thus, we propose the following solution for the implant design: to structure the implant body with a biocompatible laser-induced grooved relief and cover the surface of abutment with the antibacterial oxide film.

Acknowledgments

References

[1]. K. Almas, et al., What is the best micro and macro dental implant topography?, *Dental Clinics of North America,* Vol. 63, Issue 3, 2019, pp. 447-460.

[2]. F. Rupp, *et al.*, Surface characteristics of dental implants: A review, *Dental Materials,* Vol. 34, 2018, pp. 40-57.

[3]. D. Duraccio, *et al.*, Biomaterials for dental implants: Current and future trends, *Journal of Materials Science*, Vol. 50, Issue 14, 2015, pp. 4779-4812.

[4]. A. Wennerberg, T. Albrektsson, Effects of titanium surface topography on bone integration: A systematic review, *Clinical Oral Implants Research,* Vol. 20, 2009, pp. 172-184.

[5]. K. Doll, et al., Development of laser-structured liquid-infused titanium with strong biofilm-repellent properties, *ACS Applied Materials & Interfaces* Vol. 9, Issue 11, 2017, pp. 9359-9368.

[6]. F. Hizal, et al., Impact of 3d hierarchical nanostructures on the antibacterial efficacy of a bacteria-triggered self-defensive antibiotic coating, *ACS Applied Materials & Interfaces*, Vol. 7, 2015, pp. 20304-20313.

(081)

Particle Size and Density of Dispersion Phase Measurement by Light Scattering Methods

Sh. M. Ismailov, Yu. D. Arapov, V. G. Kamenev and A. A. Tavleev

N. L. Dukhov All-Russian Scientific Research Institute of Automatics
Address: 22, Sushchevskaya St., Moscow, 127055, Russian Federation
Tel.: +7 (988) 655 44-45
E-mail: ismailov@vniia.net

Summary: The report presents a description of laser-optical methods and equipment for recording the parameters of laser radiation transmitted and scattered by a dispersed medium. The results of the application of the methods and the created equipment make it possible to obtain information on the concentration of scatterers and their sizes at various intensities of dusting processes in gas dynamic experiments.

Keywords: Gas dynamic experiment, Coherent backscattering, Mie, Laser-optical methods, Dispersed phase, Aerosol.

1. Introduction

The study of the properties of structural materials and special products is a very urgent problem in the field of gas-dynamic research by shock-wave methods. At the same time, various methods are mainly used to register the motion of surfaces [1, 2]. However, when the shock wave interacts with the sample surface and the pressure thresholds are exceeded, the processes of spalling and microcumulation of dust particles are observed, leading to the formation of metal particles. At the beginning of the surface movement, the formed particles have velocities that exceed the speed of the surface itself, as a result of which the surface is screened by a cloud of these particles [3]. The parameters of the dispersed phase significantly affect the results of studying the motion of the free surface by optical and interferometric methods, since, firstly, the dispersed phase creates a parasitic signal of radiation reflected from the dust, and, secondly, it screens the free surface from probing radiation. At present, the mechanisms of the formation of a dispersed phase during shock-wave loading of structural materials have not been sufficiently studied, which makes the results of this study in demand. Determination of the parameters of a cloud of a dispersed phase is possible using such optical methods as statistical scattering, photon correlation spectroscopy, diffraction methods, and electron microscopy [4]. In this paper, we describe the results of studying the possibility of using the method of small-angle light scattering by small particles in accordance with the Mie theory.

The combination of holography, coherent backscattering (CBS) and Mie scattering methods will expand the range of recording the parameters of dust formations. Simultaneous registration by several methods will allow tracking the dynamics of the development of a dust cloud, Fig. 1.
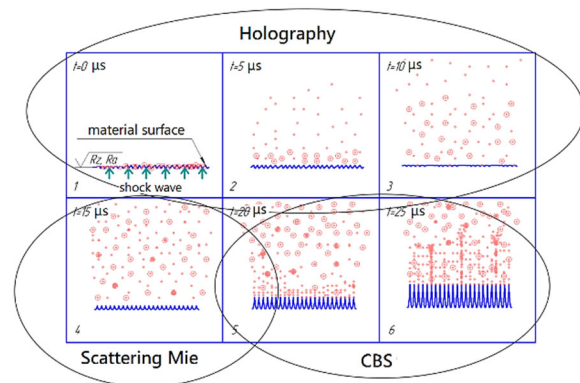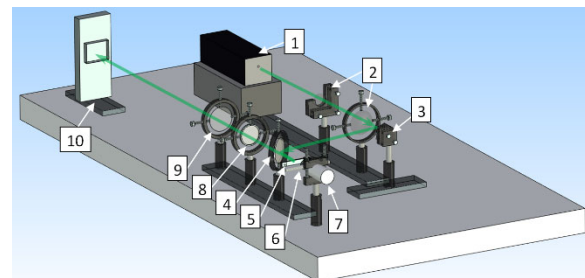

Fig. 1. Study of combined methods.

2. CBS Registration System

Fig. 2 shows a general view of the experimental setup for recording coherent backscattering in dispersed media, which is commonly used in static experiments. The installation works as follows.

1 – laser, 2 – telescope, 3 – mirror, 4 – semitransparent mirror, 5 – wedge-shaped sample, 6 -displacement, 7 – motor, 8 – polarizer, 9 – lens, 10 – recorder

Fig. 2. CBS registration system.

This installation has some limitations, for example: it is not possible to register loose dust, since the study of loose dust gives special information about the studied environment. The aim of this work was to increase the reliability of information on the parameters of a dispersed medium at a high intensity of dusting processes in gas dynamic experiments by analyzing the radiation transmitted and scattered by the dispersed medium.

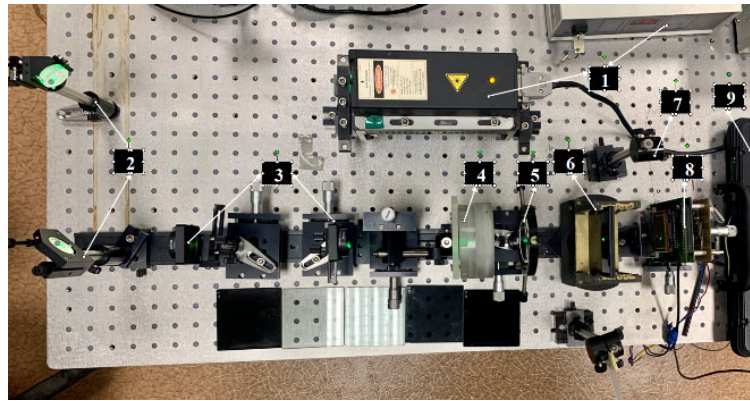## 3. Mie Scatter Registration System

It follows from the Mie theory that the angular distribution of light scattered by particles of a dispersed medium is uniquely related to the particle radius R. The intensity of light scattered by one particle at different angles to the direction of the incident beam (light scattering indicatrix) is determined by the following relationship:

$$I = I_0 \frac{8\pi^4}{z^2\lambda^2} R^6 \left(\frac{m^2-1}{m^2+1}\right)(1+\cos^2\gamma), \qquad (1)$$

where m is the refractive index of the particle substance, z is the distance from the particle to the recording device, λ is the wavelength, I_0 and I are the intensities of the incident and scattered emitters, γ is the angle at which the intensity of the scattered radiation is measured relative to the incident one.

Fig. 3 shows a general view of the stand for recording Mie scattering.


1 – laser, 2 – mirror, 3 – beam expander, 4 – object, 5 – lens, 6 – filter, 7 – screen, 8 – CMOS matrix, 9 – computer

Fig. 3. Stand for registration of Mie scattering.

Experiments were conducted using the USAF-1951 world as a sample. The beam was aimed at the central part of the target, where the positions with the minimum size are located. Fig. 4 shows the results of superposition of the Fourier image from the angular profile of the transmitted radiation and the positions of the USAF-1951 target.
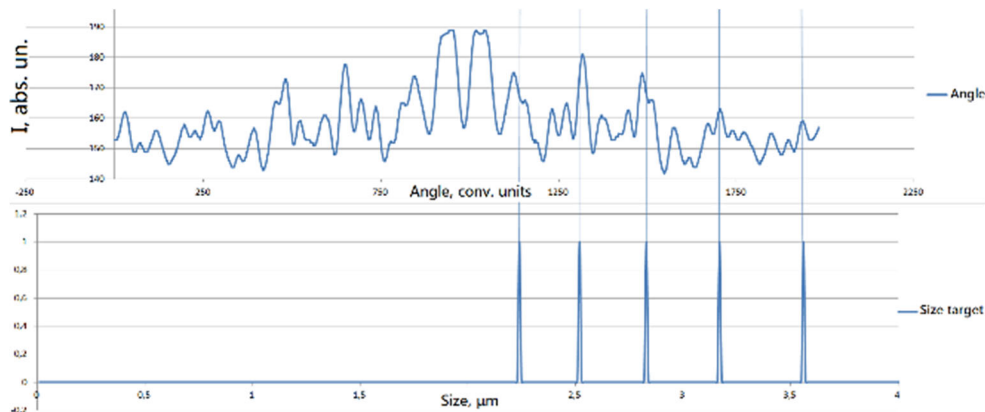
Fig. 4. The results of the superposition of the Fourier image from the angular profile of the transmitted radiation and the positions of the USAF-1951 target.

The first peak of the distribution, symmetrical about the center, is associated with the processing features and suppression of low spatial frequencies. The rest of the distribution peaks correlate with the sizes of the main positions of the target.

Simulation of light scattering by particles of a dispersed phase was performed using the Fresnel software package [5], in which the calculation of the intensity distribution over the beam cross section during propagation is determined based on the calculation of the Fresnel integral:

$$Q(x, y, d) =$$
$$= -\frac{1}{i\lambda}\frac{e^{i\frac{2\pi}{\lambda}d}}{d}\iint_{-\infty}^{+\infty} I(x`, y`, 0) \cdot e^{\frac{i\pi}{\lambda d}\left[(x-x`)^2 + (y-y`)^2\right]} dx`dy`, \quad (2)$$

where x`, y`, are the coordinates of the starting distribution of the beam intensity I (x`, y`, 0), x, y are the coordinates of the calculated distribution of the beam intensity Q (x, y, d) at a distance d from the starting one.

4. Conclusions

- Designed, assembled, and experimentally tested a stand for registering CBS and Mie scattering.
- Simulation of light scattering by particles of the dispersed phase in the Fresnel software package has been carried out.
- The CBS method allows the estimation of the concentration of particles at high dust densities.
- Based on the results obtained from experimental data and performed calculations, the Mie method at a given concentration allows one to quantitatively

determine the size of the particles on which scattering occurs, and the CBS method to obtain information about the concentration.

References

[1]. M. M. Schauer, W. T. Buttler, D. K. Frayer, Ejected particle size distributions from shocked metal surfaces, *J. Dynam. Behavior Mater.*, Vol. 3, Issue 2, 2017, pp. 217-224.

[2]. Y. L. Kim, Y. Liu, R. K. Wali, H. K. Roy, V. Backman, Low-coherent backscattering spectroscopy for tissue characterization, *Applied Optics*, Vol. 44, 2007, pp. 366-377.

[3]. R. Sapienza, S. Mujumdar, C. Cheung, A. G. Yodh, D. Wiersma, Anisotropic weak localization of light, *Physical Review Letters*, Vol. 92, Issue 3, 2004, 033903.

[4]. W. S. Vogan, W. W. Anderson, M. Grover, et al., Piezoelectric characterization of ejecta from shocked tin surfaces, *Journal of Applied Physics*, Vol. 98, 2005, 113508.

[5]. Fresnel Software Package, Fresnel.com

(082)

Determination of Sound Speed in Optical Fibers Based on the Stimulated Mandelstam-Brillion Scattering Effect

A. A. Tavleev [1], Yu. D. Arapov [1], P. V. Kubasov [1] and Sh. M. Ismailov [1]

[1] N. L. Dukhov All-Russian Scientific Research Institute of Automatics,
Moscow city, Russia
Tel.: +7 495-321-49-66
E-mail: alaltav@mail.ru

Summary: This work is focused on creating multipurpose device for diagnostics of interferometric measuring systems. Operating principle of such device is based on appearing of a nonlinear effect – stimulated Mandelstam-Brillion scattering (SMBS) which appears because of influence of laser radiation in optical fiber. As a result there were conducted investigations of parameters of nonlinear effect in optical paths under different conditions. There were formulated recommendations for designing device and methods for diagnostics of measuring systems such as Photon Doppler velocimetry (PDV), velocity interferometer system for any reflector (VISAR), and Fabry-Perot. The purpose of this work is to determine the technical capabilities of the implementation of the diagnostic method for velocity measuring systems such as PDV, VISAR and Fabry-Perot. For this purpose, in this work, the thresholds for the appearance of the SBS effect were determined, experimental measurements of the spectral shift were carried out, and the ultrasound velocity in various media was calculated from the data obtained.

Keywords: Stimulated Mandelstam-Brillion scattering, Nonlinear effects, Sonic wave, Sound speed, Stokes wave.

1. Introduction

In experiments on studying shock-wave loading using diagnostics of the speed of motion of accelerated objects based on laser interferometric systems, to increase the level of the useful signal, it is necessary to use high-power laser radiation sources. At the same time, to increase the number of recording channels, time division multiplexing with extended signal delay lines is often used, which can lead to the manifestation of nonlinear optical effects [1]. In this work, it is proposed to use one of such effects – stimulated Mandelstam-Brillouin scattering (SMBS) – in order to create equipment for verifying velocity measurement systems such as Photon Doppler velocimetry (PDV), velocity interferometer system for any reflector (VISAR), and Fabry-Perot.

The creation of a universal stand for diagnostics of laser-interferometric instrumental systems is an urgent task, which will provide the possibility of calibration by measuring the spectral shift of the signal reflected back due to the SBS effect in an optical fiber.

SMBS is a nonlinear process that can occur in optical fibers at a radiation power much lower than that required for other nonlinear effects [2]. It manifests itself in the form of generation of a Stokes wave propagating in the opposite direction and containing the largest part of the initial energy. The magnitude of the spectral shift depends on the speed of the ultrasonic wave generated in the optical fiber. Since the speed of sound in a medium is measurable and known with a high accuracy, this can be used for calibration and verification of laser-optical speed meters.

2. Review of Studies on Nonlinear Effects in Optical Fibers

Studies of the maximum achievable parameters of fiber-optic systems for the transmission of laser radiation began a long time ago and this was due to the improvement in the quality and transmission of the created samples of fiber products, which, as a result, made it possible to increase the length of fiber-optic lines and create a new class of laser emitters and amplifiers – the so-called fiber-optic lasers and amplifiers with diode pumping.

Analyzing the material of the studies performed on the problem of limiting the capabilities of fiber-optic systems for transmitting laser radiation, it is clear that there are the following main limiting factors:

- Radiation resistance of optical fibers;
- The phenomenon of stimulated Mandelstam-Brillouin scattering (SMBS);
- Stimulated Raman scattering (SRS);
- Four-wave displacement (FWD).

With an increase in the power of laser radiation obtained in such devices, developers and researchers faced physical limitations, which were caused by such effects as SMBS [3-5], SRS [4, 6], FWD [6, 7], the result of which was a decrease in quality radiation, damage to elements of the optical schemes, the appearance of parasitic spectral components. The study of the indicated parasitic phenomena was carried out both within the framework of theoretical concepts about the processes accompanying the propagation of radiation in optical waveguides, and experimentally. As a result, the basic relationships were determined, which make it possible to perform accurate

calculations and approximate estimates of the limits of the occurrence of nonlinear phenomena, the power of scattered waves, emerging harmonics and other components resulting from the interaction of light with the environment. Researchers from various scientific groups carried out a large amount of experimental research, as a result of which the nature and numerical characteristics of the arising nonlinear phenomena at various parameters of radiation (wavelengths, spectral width) and optical fibers (core diameters, lengths, dispersion) were determined, the limits of their occurrence and efficiency.

It should be noted that the research carried out has a peculiarity associated with the fact that most of the work is aimed at solving problems associated with the provision of traditional telecommunication problems: the exchange of information over a long distance with the maximum possible speed. Existing works devoted to the study of the onset thresholds and characteristics of SMBS, SRS, and other nonlinear effects practically do not consider the propagation of narrow-band radiation (with a line width in the range of tens, hundreds, and units of kHz) in optical fibers up to 3 km long. As a result, the coverage of experimental results, for example, for SMBS, looks as shown in Fig. 1.
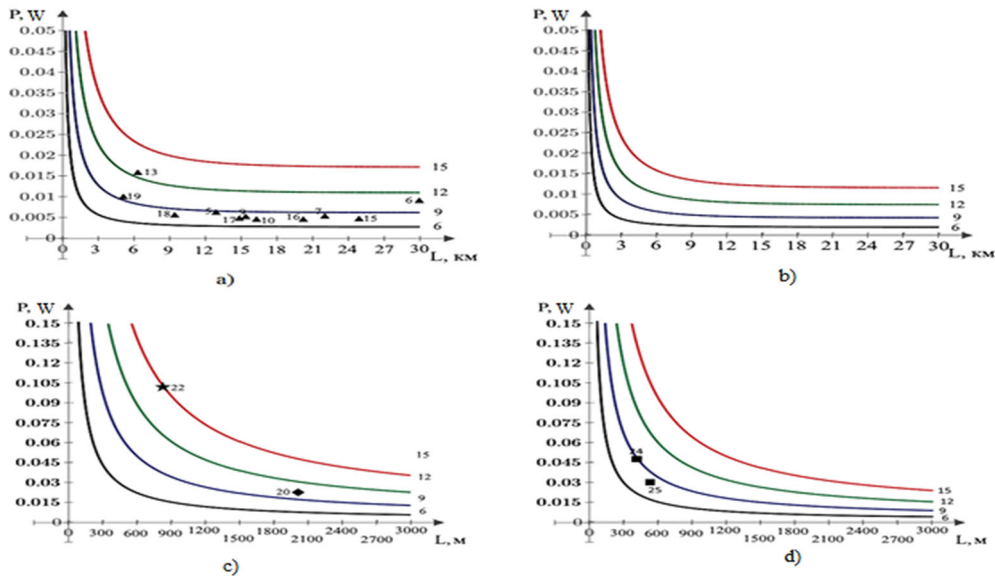
Fig. 1. Comparison of the results of experimental studies based on the data of [5-7, 9, 10] with the calculated dependence of the threshold SMBS power on the fiber length for a given core diameter for the spectrum width (labels with numbers correspond to the results works with serial numbers according to Table 1:
a), c) 10 MHz, b), d) 10 kHz.

Table 1. Ultrasound speed and SMBS threshold.

No.	Fiber type	Ultrasound speed, m/s	SMBS threshold, mW
1.	SMF-28 (25 km)	5447	4
2.	GeO_2 – fiber (47 m)	4972	134

Since the effect of lowering the threshold for the occurrence of SMBS for such radiation is obvious, and the existing data for the formation of a full-fledged picture are not enough, the problem of experimental determination of the characteristics of nonlinear effects for narrow-band radiation used in interference optical fiber techniques with short optical fibers is urgent.

3. Estimation of the Threshold for the Onset of Stimulated Scattering of Mandelstam-Brillouin

In the event of SMBS occurrence, acoustic phonons are involved in the process of interaction of radiation with matter, while the interaction at a wavelength of 1.55 μm occurs in a narrow frequency band $\Delta f_b = 20 \cdot 10^6$ Hz [1]. Therefore, in SMBS, wavelengths with an interval of more than 20 MHz between them do not interact. Within this width, SMBS can cause significant distortions of the original signal, which is expressed in the appearance and amplification of a reverse directional frequency-shifted signal (Stokes wave). In applications involving the use of fiber-optic components in measuring complexes, SMBS leads to a decrease in the level of the useful signal and a decrease in the signal-to-noise ratio, which entails a loss of information content of the received data. Some of the forward propagating light is scattered backward by the refractive index waves with a frequency shift. This leads not only to a weakening of the signal transmitted along the fiber in the forward direction, but also to the appearance of additional variations in the frequency and amplitude of the radiation source when reflected radiation hits it.

Shown in Fig. 2 families of curves characterize the dependence of the threshold power on the length and diameter of a single-mode fiber at spectral widths of 10 kHz and 100 MHz.

The SMBS process can be described classically as a parametric interaction between pump, Stokes and acoustic waves. Due to electrostriction [11], the pump generates an acoustic wave, which leads to periodic modulation of the refractive index. The induced refractive index grating scatters the pump radiation as a result of Bragg diffraction. Since the grating moves with a sonic velocity vA, the frequency of the scattered radiation undergoes a Doppler shift towards the region of longer wavelengths. The speed of sound in a medium is expressed by the formula [2].
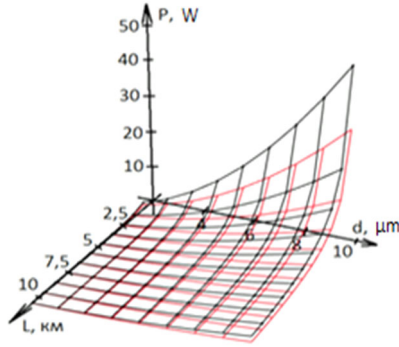
Fig. 2. Dependence of the threshold power of SBS occurrence on the length and diameter of the waveguide core at a signal wavelength of 10 kHz (red (lower) grid) and 100 MHz (black (upper) grid), L is the length, d is the diameter of the fiber core.

$$\nu_A = \frac{\upsilon_B \lambda_p}{2n_p},\qquad(1)$$

where υ_B is the frequency shift at SMBS, λ_p is the pump wavelength, n_p is the effective refractive index at the pump wavelength λ_p.

Since the speed of sound in a medium is measurable and known with a high accuracy, it can be used for diagnostics of laser-optical speed meters.

## 4. Experiment Setup and Results

In this work, the thresholds for the onset of the SMBS effect were determined, experimental measurements of the spectral shift were carried out, and from the data obtained, the ultrasound velocity in various media was calculated. The diagram of measurements and equipment location is shown in Fig. 3.

To calculate the threshold signal power at which the power output signal is compared with the wave scattered in the opposite direction, taking into account the width of the radiation spectrum, use the expression [2]:

$$P_{SMBS} \approx \frac{21bS_e}{g_B L_e}\left(1 + \frac{\Delta f_s}{\Delta f_B}\right),\qquad(2)$$

where b takes values from 1 to 2, depending on the state of polarization of the initial wave and the Stokes

wave (in the worst case, when the radiation of both waves is linearly polarized b = 1), S_e is the cross-sectional area of the fiber core along which the signal propagates, $L_e = \frac{1-e^{-\alpha L}}{\alpha}$ is the effective fiber length, $g_B = 4.5 \cdot 10^{-11}$ is the typical SMBS gain for silica fiber, Δf_s – is the line width signal radiation, Δf_B is the SMBS gain frequency band (20 MHz).
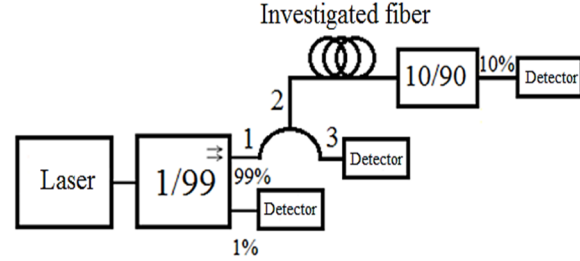
Fig. 3. Measurement scheme for determining the ultrasound velocity.
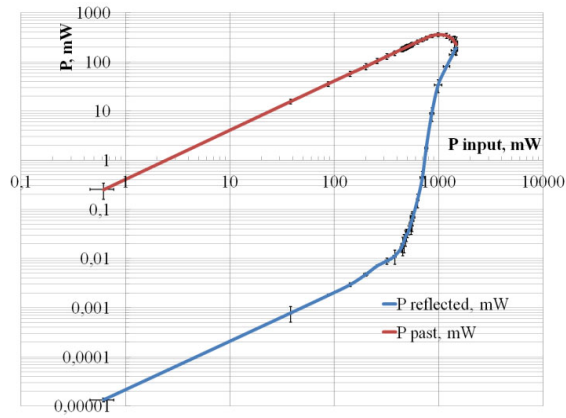
Graphs of the dependence of the transmitted and reflected power of laser radiation on the input power were plotted for the optical fiber SMF-28 and GeO$_2$-fiber. The obtained experimental curves were used to determine the thresholds for the occurrence of SMBS in the studied fibers, which manifests itself in the form of a significant increase in the intensity of the reflected signal.

The experimental curves for optical single-mode fiber SMF-28 and GeO$_2$-fiber are shown in Fig. 4 and Fig. 5, respectively.
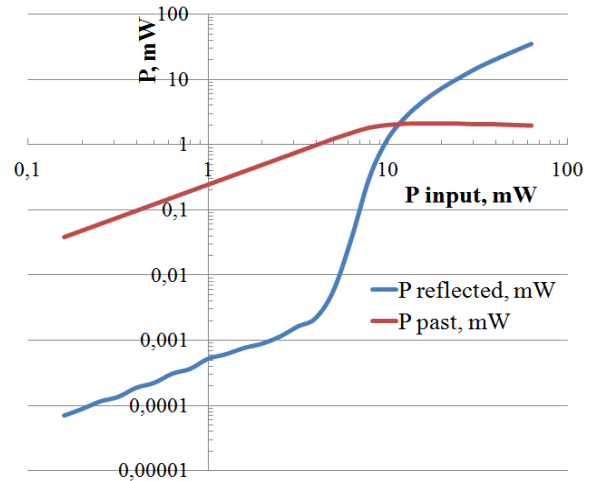

Fig. 4. Dependences of the transmitted and reflected power of laser radiation on the input power for an SMF-28 optical single-mode fiber with a length of 25 km and a core diameter of 9 μm.

Fig. 6 shows a schematic diagram for determining the spectral shift for SMBS in optical fibers. Experimental determination of the spectral shift is possible in two ways: using a spectrometer or using a photodetector and oscilloscope instead of device 7, as shown in Fig. 6.

Fig. 5. Dependence of the transmitted and reflected power of laser radiation on the input power for an optical single-mode fiber doped with GeO_2 with a length of 47 m and a core diameter of 2.2 μm.
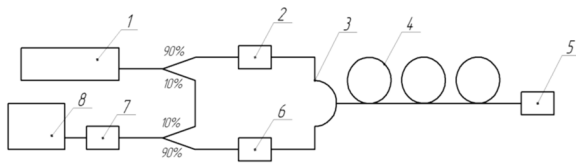

Fig. 6. Scheme for determining the speed of sound in an optical fiber based on the SBS effect (1 – laser, 2 – pass-through power meter, 3 – circulator, 4 – SMF-28 fiber optic 25 km, 5.6 – power meters, 7 – photodetector, 8 – oscilloscope)

Using a spectrometer, we obtain spectrograms of signals (transmitted and reflected) spaced from each other at a certain distance characteristic of a given sample. Fig. 7 and Fig. 8 show spectrograms for SMF-28 and GeO_2 optical fibers, respectively.
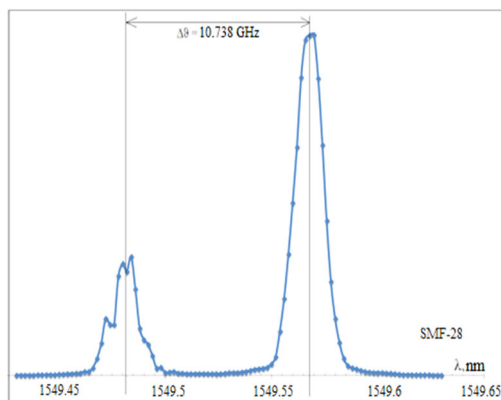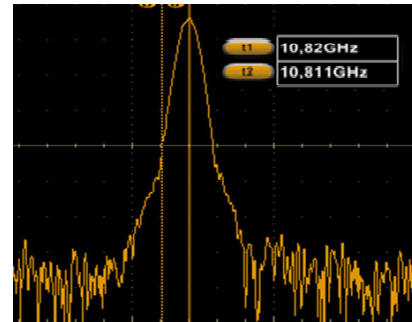

Fig. 7. Spectrograms of the output laser radiation for an SMF-28 single-mode optical fiber 25 km long and 9 μm in diameter.

The second method is based on the use of PDV technology. Fig. 9 and Fig. 10 show the processed oscillograms of the frequency beats for the SMF-28 optical fiber and for the GeO_2-doped fiber, respectively. With the help of Fourier transforms, it is possible to determine how much the frequency of the reflected signal has shifted from the transmitted one.
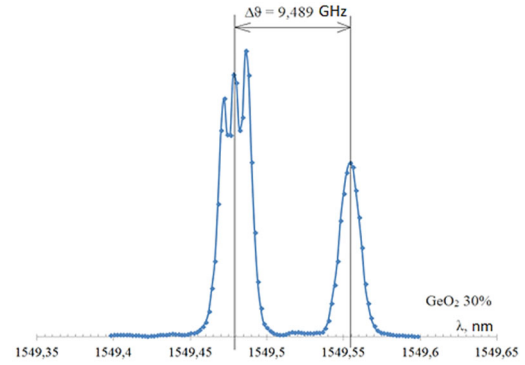
Fig. 8. Spectrograms of the output laser radiation for an optical single-mode GeO_2 fiber with a length of 47 m and a core diameter of 2.2 μm.

Fig. 9. Oscillogram of the output laser radiation for an SMF-28 single-mode optical fiber with a length of 25 km and a core diameter of 9 μm.
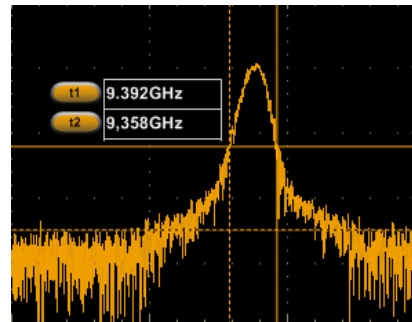
Fig. 10. Oscillogram of the output laser radiation for an optical single-mode GeO2 fiber with a length of 47 m and a core diameter of 2.2 μm.

Thus, the spectral shift was determined for two fibers: SMF-28 with a length of 25 km and GeO_2 fiber with a length of 47 m. For the case with SMF-28 at a power of 4 mW, the spectral shift corresponds to a speed of 5447 m/s, and for the case with a germanium doped fiber at a power of 130 mW the spectral shift corresponds to a speed of 4972 m/s.

5. Conclusions

In this work, we present the results of experimental development of an optical scheme for observing the SMBS effect under various conditions when measuring the spectral shift based on the heterodyne principle. Estimates are made for the speed of sound

for optical fibers with a core of various types of materials. The data obtained are compared with the calculated values of the speed of sound in optical fibers.

In this work, we determined the threshold powers at which stimulated Brillouin scattering is excited, measured the ultrasound velocity in an SMF-28 single-mode optical fiber 25 km long with a core diameter of 9 μm and in a GeO$_2$ fiber 47 meters long with a core diameter of 2.2 μm with the use of narrow-band laser radiation with a line width of 1 kHz.

The results obtained demonstrate the fundamental possibility of implementing a device that allows diagnostics of measuring complexes based on laser heterodyne interferometers using the SBS effect.

Having large experimental data (wavefront reversal, SMBS onset threshold) in various types of fibers and in various media of laser radiation propagation, we are able to diagnose a PDV-based device in different spectral regions.

Table 2. Summary table on the existing experimental data on the thresholds of SMBS.

№	Fiber length, m	Losses, dB / km	Core diameter, μm	Fiber type	Wavelength, μm	Line width, MHz	Threshold power, W (dBm)
1.	5.8	20	3.8	SMF	0.535	100	2.3 (33.6)
2.	4000	4	3.5	SMF	0.71	30	0.03 (13)
3.	13000	0.41	9	SMF	1.32	22	0.0056 (7.5)
4.	30000	0.46	10	SMF	1.3	22	0.01 (10)
5.	22000	0.2	8	SMF	1.55	20	0.004 (6)
6.	396	0.4	9	SMF	1.064	0.01	102 (20)
7.	500	1	4.5	HNLF	1.55	0.01	0.0298 (14.7)
8.	900	0.8	4	HNLF DS	1.55	0.01	0.0232 (13.65)
9.	200	17	10	MSF	1.55	0.01	1.29 (31.1)
10.	100	30	10	MSF with acetone	1.55	0.01	0.521 (21.17)
11.	10	0.3 [8]	1.5	MSF with CS$_2$	1.55	0.01	0.005 (7)

References

[1]. A. B. Ivanov, Fiber Optics: Components, Transmission Systems, Measurements, *Cyrus Systems*, 1999.

[2]. G. P. Agrawal, Nonlinear Fiber Optics, 4th Ed., *The Institute of Optics University of Rochester*, New York, 2007.

[3]. E. P. Ippen, R. H. Stolen, Stimulated Brillouin scattering in optical fibers, *Appl. Phys. Lett.*, Vol. 21, Issue 11, 1 December 1972, 539.

[4]. R. G. Smith, Optical power handling capacity of low loss optical fibers as determined by stimulated Raman and Brillouin scattering, *Appl. Opt.,* Vol. 11, 1972, pp. 2489-2494.

[5]. G. B. Benedek, K. Fritsch, Brillouin scattering in cubic crystals, *Phys. Rev.*, Vol. 149, 1966, 647.

[6]. P. Labudde, P. Anliker, H. P. Weber, Transmission of narrow band high power laser radiation through optical fibers, *Optics Communications*, Vol. 32, Issue 3, March 1980, pp. 385-390.

[7]. K. O. Hill, D. C. Johnson, B. S. Kawasaki, R. I. MacDonald, CW three-wave mixing in single-mode optical fibers, *J. Appl. Phys.*, Vol. 49, 1978, 5098.

[8]. Y. E. Monfared, S. A. Ponomarenko, Slow light generation via stimulated Brillouin scattering in liquid-filled photonic crystal fibers, *Optik*, Vol. 127, Issue 15, 2016, pp. 5800-5805.

[9]. R. J. Smith, Optical power handling capacity of low loss fibers as determined by stimulated Raman and Brillouin scattering, *Applied Optics*, Vol. 11, Issue 1, 1972, pp. 269-270.

[10]. R. Ramaswami, K. N. Sivarjan, Optical Networks: A Practical Perspective, *Morgan Kaufmann Publishers Inc.*, San Francisco, California, 1998.

[11]. R. W. Boyd, Chapter 9, in Nonlinear Optics, 2nd Ed., *Academic Press*, San Diego, 2003.

Sponsored by:

9 788409 244218